8-2016

Sounding Rocket Measurements of Vertically-Sheared F Region Neutral Winds at Sunset and Modeling of their Effect on Spread F Development

Andrew Kiene
Clemson University

Recommended Citation

Kiene, Andrew, "Sounding Rocket Measurements of Vertically-Sheared F Region Neutral Winds at Sunset and Modeling of their Effect on Spread F Development" (2016). *All Dissertations*. 1721.
https://tigerprints.clemson.edu/all_dissertations/1721

SOUNDING ROCKET MEASUREMENTS OF VERTICALLY-SHEARED F REGION NEUTRAL WINDS AT SUNSET AND MODELING OF THEIR EFFECT ON SPREAD F DEVELOPMENT

A Dissertation
Presented to
the Graduate School of
Clemson University

In Partial Fulfillment
of the Requirements for the Degree
Doctor of Philosophy
Physics

---

by
Andrew Kiene
August 2016

Accepted by:
Dr. Miguel Larsen, Committee Chair
Dr. Gerald Lehmacher
Dr. Jens Oberheide
Dr. Chad Sosolik

Abstract

During the hours near sunset, Earth's equatorial ionosphere undergoes significant changes as it transitions from day to night. This period is a dynamic time that preconditions the ionosphere for a number of plasma instabilities that may develop over the course of the night, including equatorial spread *F*. The neutral dynamics of the sunset ionosphere are of critical importance to the generation of the currents and electric fields which drive spread *F* and other instabilities; however, the behavior of the neutrals is experimentally understood through single-altitude measurements or measurements that provide weighted altitude means of the winds as a function of time. Vertically resolved neutral wind measurements in the *F* region near and after sunset are extremely rare. In this work, are presented several sounding rocket chemical tracer measurements, which are vertically resolved and show large westward winds and wind shears in the *F* region near sunset. Winds and shears of this magnitude near sunset are unexpected based on current wind models, which show eastward neutral flow with very small gradients above 200 km altitude. The observed chemical tracer neutral wind profiles are applied to an existing spread *F* model in order to investigate the effects of such large westward winds and shears during the transitional period near sunset on the subsequent development of spread *F* plumes. The unusual wind profiles observed in the experiments are shown to have a suppressing effect on instability development.

Dedication

For everyone who kept believing in me, even when I had trouble believing in myself.

Acknowledgments

My sincerest thanks go out to my advisor, Miguel Larsen, for his patience and continued support throughout my work at Clemson, as well as the rest of the atmospheric physics group, who have given valuable insight at our group meetings.

I appreciate the contributions of our collaborators on this project: Dr. Dave Hysell of Cornell University, whose numerical model made this study possible, as well as Dr. Rob Pfaff of Goddard Space Flight Center and Dr. Erhan Kudeki of the University of Illinois at Urbana-Champaign, who contributed data from the other instruments on the EVEX campaign.

And finally, thank you to everyone who participated in the rocket campaigns throughout my tenure at Clemson. Thanks to Patti Larsen for both operating camera sites and organizing our equipment and making sure an absent-minded graduate student like me didn't forget anything. Thanks to all of the other camera operators over the years: Lamar Durham, Jon Simpson, Barrett Barker, Lucas Hurd, and Brenden Roberts. Finally, thanks to all the hundreds of other people at NASA and elsewhere who had a role in making sure the experiments were a success.

Table of Contents

List of Figures

Chapter 1

Introduction

The Earth's ionosphere, the region of the upper atmosphere where the gas becomes partially ionized due to solar radiation, is a dynamic and complex system. There are many cycles and phenomena that contribute to the variability of the ionosphere, ranging from the simple day-night cycle to intense solar activity that generates geomagnetic disturbances which, in turn, cause spectacular cascades of energy that propagate through the atmosphere. Equatorial spread F is a broad collection of plasma density irregularities that are often observed during the premidnight hours in the ionosphere near the Earth's geomagnetic equator. The observed density irregularities are driven by the inherently unstable vertical plasma density gradients that form near sunset. This creates instability in the bottomside F region near 250 km altitude, but the resulting nonlinear cascades of energy, which drive convective mixing that can produce large plumes, sometimes called bubbles, of density depletion to well over 1000 km altitude. This interpretation was first presented by Woodman and LaHoz (1976), nearly four decades after the first observations of spread F were reported by Booker and Wells (1938).

Four more decades have passed since Woodman and LaHoz (1976) gave their revolutionary interpretation. With the process more or less identified, one might expect that this would be enough time to fully come to comprehend it. This has not been the case, however. Complete understanding of the ionospheric processes that begin before sunset and progress into the evening, which may or may not eventually result in spread *F*, is still lacking. Our measurement and modeling techniques have improved greatly over the years, but we still lack some of the funamental data required to accurately model and predict spread *F* on a daily basis.

Today, spread *F* can be observed using a variety of ground-based techniques, as well as spaceborne instruments on sounding rockets or satellites (see Chapter 3). The plasma density irregularities produced by the instabilities cause the scintillation of radio signals, which interferes with communication, navigation, and imaging systems.

The dynamics of spread *F* have been the subject of many theoretical and experimental studies over the past decades, with the ultimate goal of accurate prediction of spread *F* development. For a recent review of spread *F* theories and experiments, see review papers by Woodman (2009) and Kelley et al. (2011). Our understanding of many of these processes has improved significantly, but there is still a sparsity of observational data of some of the critical parameters, including the characteristics of the neutral winds in the important bottomside *F* region. The exact seeding mechanisms that lead to the pronounced instabilities are still under investigation; however, the neutral wind is a key driver of nearly all of these mechanisms.

The experimental understanding of neutral wind behavior in the sunset *F* region to this point has been mostly limited to single-altitude satellite measurements and vertically-integrated ground-based optical measurement techniques [REFS]. Neither of these techniques provide information about any vertical structure within the wind field.

This dissertation presents new vertically-resolved neutral wind profiles derived from several sounding rocket experiments conducted near the geomagnetic equator. These experiments have revealed significant vertical shears in the wind field that were unexpected based on previous single-altitude measurements. In addition, the winds respond rapidly to the motion of the solar terminator, reversing direction over a period of about 20 minutes as the terminator rises.

In order to understand the effects of such neutral wind shears on the development of spread *F*, we have developed a model wind field that evolves based on the motion of the solar terminator. We applied this wind field to an updated version of the 3-D numerical spread *F* model created by Aveiro and Hysell (2010) in order to compare the effects of the experimentally-measured sheared wind profile on spread *F* development to that produced by a smoother wind profile based on the Horizontal Wind Model (HWM14) (Drob et al., 2015).

It is our hope that this work sheds some light on the missing pieces of the spread *F* puzzle. Little consideration has been given to potential vertical variability in *F* region winds in recent years. This is because we have had no practical way to measure them and because there has been little motivation to do so. The climatology of winds at single altitude points is well understood, and the norm has been to generalize those wind trends to all altitudes. The results of this study show that it is important to take a renewed interest in fully understanding the behavior of *F* neutral winds near sunset in order to completely understand spread *F* development.

The objective of this dissertation is to explore the effect of vertically sheared zonal winds on the development of postsunset ionospheric plasma instabilities. Chapter 2 gives some background information about the composition and dynamics of the equatorial ionosphere, as well as a discussion of the theory that motivates the study of *F* region neutral winds as a driver for spread *F*. We will show that neutral winds are a key driving factor in each of the theories surrounding spread *F* development.

Other potential spread F drivers will also be discussed, along with the current state of research in the field.

With the importance of neutral winds defined, Chapter 3 will discuss the various techniques for analyzing the equatorial thermosphere, weighing the advantages and disadvantages of each. Particular attention will be given to sounding rocket chemical tracer techniques, which are the focus of later chapters. Chapter 4 details the sounding rocket campaigns that took place as a part of this study, presenting the chemical tracer measurements taken from each. In Chapter 5, the features of the vertically-resolved neutral wind profiles from the three rocket campaigns are used to generate a wind field as input for a numerical spread F model. We will examine the differences in the model output when using the model winds versus the measured winds. Chapter 6 will recap the key points of each chapter as well as discuss conclusions based on the modeling work and experiments.

Chapter 2

Neutral winds as a driver of ionospheric instabilities

The Earth's upper atmosphere is a complex, interconnected system that is close enough to affect us on a daily basis, yet far enough away that it is difficult to measure. For more than a century now, we have made use of the electrical properties of Earth's ionosphere for the purposes of communication, yet we still do not fully understand the processes that can drive dramatic changes in the ionosphere. In particular, there is a dearth of neutral wind measurements above 200 km altitude. These winds, this chapter will show, have a significant effect on the daily development of ionospheric instabilities that can disrupt communications.

2.1 Atmospheric Layers

While the primary focus of this work is the dynamics of the F region, which is the region between 150 and 500 km altitude, the neutral atmosphere and the ionosphere are vertically coupled both through the Earth's dipole magnetic field geometry and through direct vertical energy propagation. Thus, it is important to understand the characteristics of all regions of the atmosphere.

Owing to the hydrostatic balance of the atmosphere, the Earth's atmosphere is stratified with respect to altitude, with regions in the lower atmosphere delineated corresponding to the direction of the vertical temperature gradient. The lowest two regions, the troposphere and the stratosphere, are entirely neutral. As the ambient density decreases with altitude, absorption of high-energy solar photons begins to ionize a fraction of the atmosphere at a rate that outpaces recombination. Above the stratosphere is the mesosphere, which contains the D region, a lightly ionized region of the ionosphere that vanishes at sunset, when the input of solar radiation ceases and recombination happens rapidly. At about 90 km altitude, the temperature reaches a minimum, termed the mesopause (Kelley, 2009). Above this point, the temperature begins to increase rapidly due to absorption of ultraviolet and extreme ultraviolet (EUV) solar radiation. The EUV radiation is sufficiently energetic to ionize the neutral gas and produce plasma in the sunlit hemisphere. Because there is one electron produced for each ionized atom, the plasma is generally assumed to be quasi-neutral, i.e., $n_e = n_i$, where n_e is the electron density and n_i is the ion density.

Above the D region lies the E region, ranging from 90 to 150 km altitude, so named during the early days of radio when it was discovered that it was electrified and thus reflected radio waves. The electron density in the E region is several orders of magnitude greater than the D region. It continues to increase with altitude into the F region (150-500 km altitude), which is often divided into the F_1 and F_2 layers corresponding to the two maxima in the daytime electron density profile produced by the effects of molecular ions. This is difficult to see in Figure 2.1 due to the logarithmic scale, but there is a small peak in daytime electron density near 200 km that corresponds to the F_1 layer, with the F_2 layer being the prominent peak near

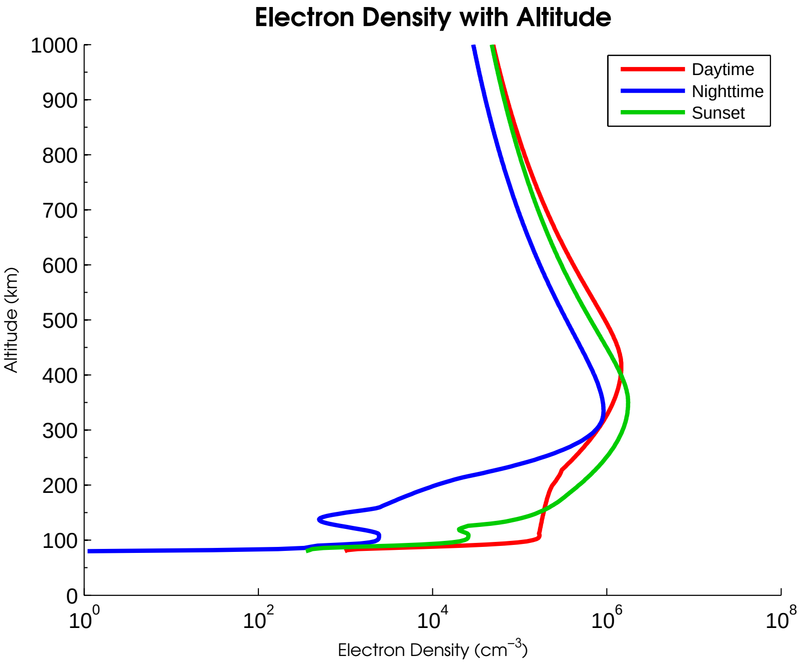

Figure 2.1: Electron density profiles from the International Reference Ionosphere (IRI-2000) model for daytime, nighttime, and sunset.

400 km.

Because the electron density in the ionosphere is directly driven by solar EUV radiation, the removal of this radiation after sunset causes a rapid decrease in plasma density throughout the ionosphere. Typical electron density profiles for the equatorial region are shown in Fig. 2.1 for daytime and nighttime, as well as for the period near sunset, which is of interest to the experiments discussed in this work. The transition from day to night creates a very sharp gradient in the bottomside F region between 200 and 300 km altitude. The neutral flow is also driven by thermal gradients resulting from solar heating, which causes a reversal of the neutral flow near sunset. These changes near sunset are termed the “F region dynamo” and are discussed further in section 2.4.

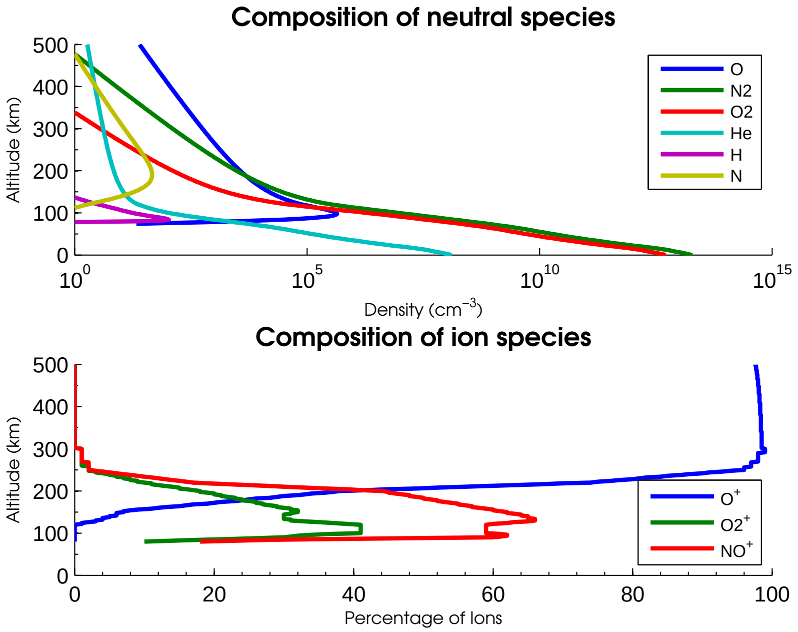

Figure 2.2: Neutral (top) and Ion (bottom) composition as a function of altitude from the surface to the topside F region. Neutral data from MSIS-E00 and ion data from IRI-00.

The molecular composition of the ionosphere also plays an important role in governing the electron density and chemical interactions. Above the turbopause, near 100 km altitude, the atmosphere ceases to be turbulently mixed, and thus individual atomic species begin to vary in density independently of one another (see Figure 2.2). Atomic oxygen becomes a significant part of the population, and it eventually exceeds the fraction of N_2 near 250 km altitude. Below 150 km, NO^+ and O_2^+ are the primary ions within the plasma, giving way to atomic O^+ in the F region. Above 500-600 km, atomic hydrogen and helium begin to dominate.

In the bottomside *F* region near 250 km altitude, where the seeding processes for spread *F* instabilities occur, the primary constituents of the neutral atmosphere are O and N_2, with the former being the subject of many ground-based optical studies thanks to its well-known emission spectrum (see Chapter 3).

2.2 Coordinate Systems, Terminology, and Units

Before continuing, it is important to the discussions that follow that the coordinate systems be clearly defined. In addition, there are certain traditional notations and units that should be clarified. The standard rectangular coordinate system used in meteorological discussions has the x-axis oriented eastward, the y-axis northward, and the z-axis upward. For ionospheric purposes, where the magnetic field is of importance, it is more useful to consider a coordinate system where the y-axis points along the magnetic field at the geomagnetic equator. The z-axis remains vertical, and the remaining x coordinate points orthogonal to the other two, which is mostly geographically eastward near the equator. Because the geomagnetic equator is quite close to the geographic equator, the deviation from the typical meteorological coordinate system is fairly small. Unless otherwise noted, this is the convention that will be used throughout this dissertation. Other terms that are often used with respect to these coordinates are that eastward and westward motions are referred to as “zonal” motions, and northward and southward motions are referred to as “meridional” motions.

There are some idiosyncrasies within the notation for the neutral and ion vectors. The neutral wind is typically denoted as $\mathbf{U}$, with components (u, v, w) corresponding to the zonal, meridional, and vertical wind, respectively. The ion drifts are represented using the vector $\mathbf{V}$, with components (V_x, V_y, V_z). Table 2.1 gives these and other common definitions for the various quantities of interest in following discussions.

Symbol	Parameter
ρ	Neutral density
p	Pressure
g	Gravity
n_e	Electron density
n_i	Ion density
$\mathbf{U} = (u, v, w)$	Neutral wind
$\mathbf{V} = (V_x, V_y, V_z)$	Ion drift
η	Viscosity
$\mathbf{\Omega}$	Coriolis parameter
σ_P	Pedersen conductivity
σ_H	Hall conductivity
σ_0	Direct conductivity
ν_{xn}	Collision frequency of species x with neutrals
κ_x	Mobility of species x

Table 2.1: Definition of symbols used in this text.

2.2.1 The Earth's Magnetic Field

The Earth's magnetic field resembles that of a dipole with an axis tilted 11° relative to that of the Earth. This means that the magnetic north pole currently resides in northern Canada rather than at the geographic north pole. This creates a somewhat complex geometry relating magnetic coordinates to geographic coordinates, resulting in an offset between the geographic and geomagnetic equators that varies significantly with longitude.

The SI unit for magnetic field magnitude is the tesla. However, the Earth's magnetic field magnitude is quite small, $0.6\text{x}10^{-4}$ tesla at the poles, so we typically refer to the magnetic field in terms of gauss, where 1 gauss = 10^{-4} tesla. Fluctuations in the magnetic field can have even smaller magnitudes. These are typically measured in gamma, with 1 gamma = 10^{-5} gauss = 10^{-9} tesla.

At the geomagnetic pole, the magnetic field vector, $\mathbf{B}$, points either directly

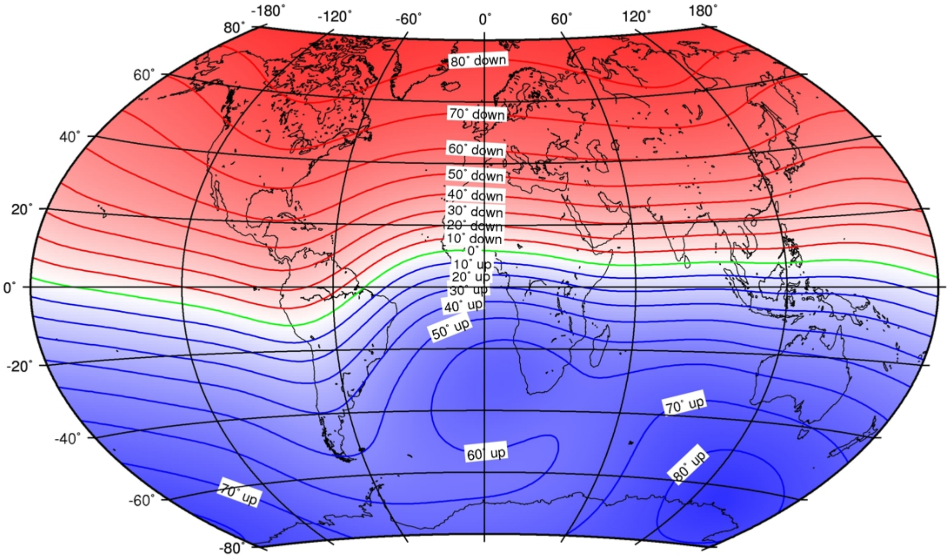

Figure 2.3: Map of geomagnetic latitude overlaid on a map of the Earth. Map taken from http://www.geomag.bgs.ac.uk/education/earthmag.html

upward (northern hemisphere) or directly downward (southern hemisphere). At the geomagnetic equator, **B** points horizontally northward with no vertical component. Magnetic latitude corresponds to the inclination of the magnetic field vector relative to these two end points. A plot of magnetic latitude overlaid on a map of the Earth is shown in Figure 2.3. In the Pacific sector, the site of one of the rocket campaigns discussed in this work, the magnetic equator is offest northward from the geographic equator by approximately 4°. In the South American sector, the primary source of spread F observations, the magnetic equator varies significantly with latitude. At the site of the Jicamarca Radio Observatory near Lima, Peru, the magnetic equator is loctated almost 12° south of the geographic equator, while the rocket launch site near Alcantara, Brazil is at only 1.2° geomagnetic latitude.

The geometry of the magnetic field near the geomagnetic equator is fairly simple, yet of critical importance to the processes that lead to the F region dynamo and subsequent nighttime irregularities. **B** points directly northward at the equator. Just

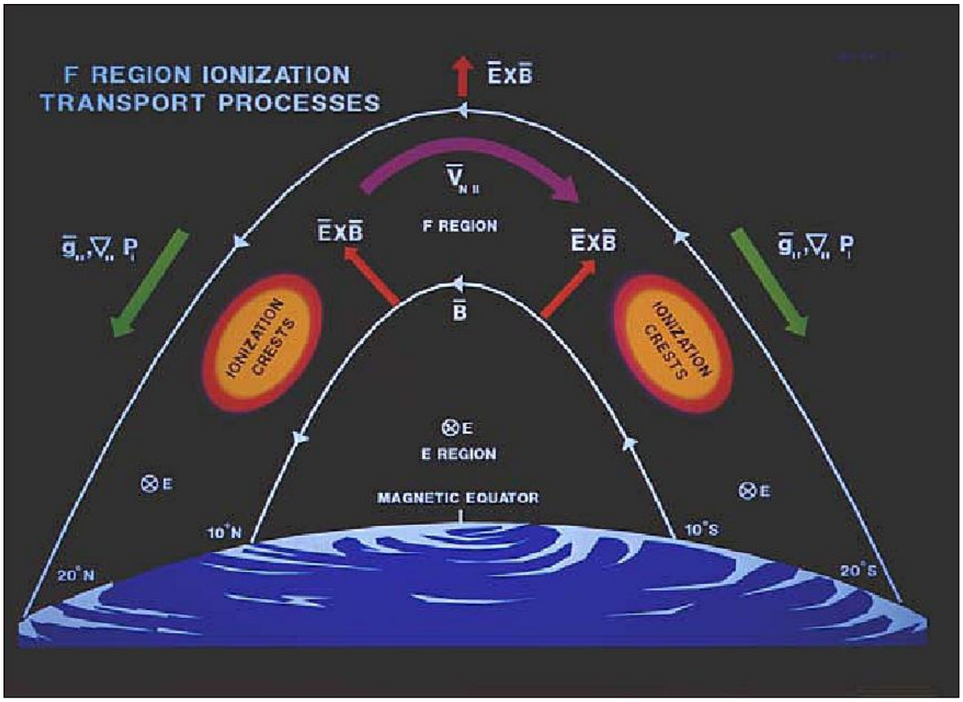

Figure 2.4: Illustration of the magnetic field geometry at the equator that results in coupling of the equatorial F region with off-equator E regions. Figure taken from de La Beaujardiere (2004).

off the equator, the vector points northward and slightly up (southern hemisphere) or down (northern hemisphere). The vertical inclination increases as we move further from the equator. The same magnetic field line that was in the *F* region at the equator will be located in the *E* region some distance north and south of the equator. This creates a coupling effect between the *E* and *F* regions that allows for current transport between the two along the field lines. This magnetic field geometry is also responsible for the maximum ionization points being located approximately 15° north and south of the equator, rather than the crest being centered on the equator. This effect, along with the magnetic field line geometry illustrating the connection between the equatorial *F* region and the off-equator *E* regions is shown in Figure 2.4.

The Earth's magnetic field at polar latitudes is significantly affected by changes in the interplanetary magnetic field (IMF), routinely producing ionospheric disturbances such as the aurora. The equatorial ionosphere is much less sensitive to geomagnetic activity; however, large magnetic perturbations have been known to cause ionospheric effects (Fejer and Scherliess (1997); Basu et al. (2001)). Geomagnetic activity was only significant during one of the experiments presented in this dissertation, and more detail will be given to potential ramifications in that section.

2.3 The Equations of Motion and Conductivity

In the ionosphere, neutral and charged particles coexist and interact. This means that we must understand the behavior of both in order to fully comprehend the evolution of the ionosphere. Kelley (2009) gives the equations of motion governing both the neutrals and the charged species. The neutral set is:

$$\frac{\partial \rho}{\partial t} = -\nabla \cdot (\rho \mathbf{U}) \tag{2.1}$$

$$\rho \frac{d\mathbf{U}}{dt} = -\nabla p + \rho g + \eta \nabla^2 \mathbf{U} - \nabla \cdot \pi_w - 2\rho \mathbf{\Omega} \times \mathbf{U} + \mathbf{J} \times \mathbf{B} \tag{2.2}$$

$$p = \frac{\rho k_B T_n}{m_n} = n_n k_B T_n \tag{2.3}$$

The ion equations are (subscript j denotes species):

$$\frac{\partial \rho_j}{\partial t} + \nabla \cdot (\rho_j \mathbf{V}_j) = (P_j - L_j) M_j \tag{2.4}$$

$$\rho_j \frac{d\mathbf{V}_j}{dt} = -\nabla p_j + \rho_j \mathbf{g} + n_j q_j (\mathbf{E} + \mathbf{V}_j \times \mathbf{B}) - \sum_{k(j \neq k)} \rho_j \nu_{jk} (\mathbf{V}_j - \mathbf{V}_k) \tag{2.5}$$

$$p_j = \frac{\rho_j k_B T_j}{M_j} = n_j k_B T_j \tag{2.6}$$

In the above equations, π_w is the momentum flux density tensor due to waves, P and L are the production and loss rates, respectively, $\mathbf{g}$ is gravity (oriented downward), T is temperature, M is mass, and k_B is the Boltzmann constant. The other quantities are defined in Table 2.1. These equation sets are coupled; the ions affect the neutral momentum through the $\mathbf{J} \times \mathbf{B}$ term, and the neutrals affect the ions through collisions via the summation term in equation 2.5. At this point, it is useful to define several quantities that are typically used to define conductivities in the ionosphere. Following the notation of Kelley (2009) for species j, the ratio of the gyrofrequency to the collision frequency is $\kappa_j = (q_j B / M_j \nu_{jn})$ and the mobility is $b_j = (q_j / M_j \nu_{jn})$. With these, we can define the conductivity tensor:

$$\sigma = \begin{pmatrix} \sigma_P & -\sigma_H & 0 \\ \sigma_H & \sigma_P & 0 \\ 0 & 0 & \sigma_0 \end{pmatrix} \tag{2.7}$$

where the individual conductivites σ_0, σ_P, and σ_H are the direct, Pedersen, and Hall conductivities, respectively. These are defined in terms of the quantities b_j and κ_j:

$$\sigma_0 = ne(b_i - b_e) \tag{2.8}$$

$$\sigma_P = ne[b_i/(1+\kappa_i^2) - b_e/(1+\kappa_e^2)] \tag{2.9}$$

$$\sigma_H = (ne/B)[\kappa_e^2/(1+\kappa_e^2) - \kappa_i^2/(1+\kappa_i^2)] \tag{2.10}$$

These Pedersen and Hall conductivities are often integrated along field lines; when this is the case, they are denoted by Σ_P and Σ_H, respectively. The direct conductivity operates parallel to $\mathbf{B}$, the Pedersen conductivity acts perpendicular to $\mathbf{B}$ and parallel to $\mathbf{E}$, and the Hall conductivity acts perpendicular to both $\mathbf{B}$ and $\mathbf{E}$. A plot of the various conductivities as a function of altitude is shown in Figure 2.5 for both daytime and nighttime. Conductivities are expressed in units of mho/m, where

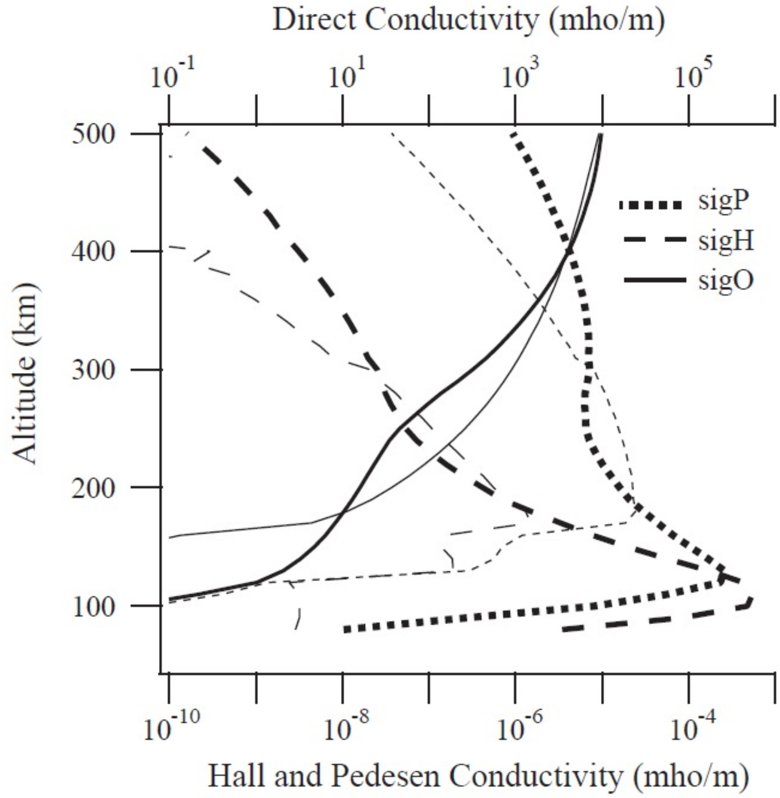

Figure 2.5: Direct, Pedersen, and Hall conductivities as a function of altitude for both day (bold) and night (thin). Note the different scale for the much larger Direct conductivity. After Heelis (2004)

1 mho = 1 Ω^{-1}.

In the F region, $\sigma_P \gg \sigma_H$ (see Figure 2.5), and so the conductivity tensor can be expressed as

$$\sigma = \begin{pmatrix} \sigma_P & 0 & 0 \\ 0 & \sigma_P & 0 \\ 0 & 0 & \sigma_0 \end{pmatrix} \tag{2.11}$$

Because the curents that flow in the ionosphere are directly modulated by the conductivity tensor ($\mathbf{J} = \sigma \cdot \mathbf{E}$), in the neutral frame, it is important to understand the behavior of the conductivities in the E and F regions near both before and after sunset. In the E region, the Hall conductivity dominates during the day, but the rapid recombination of the plasma at sunset (due to cessation of ion production by sunlight) drastically reduces the conductivity, which scales linearly with electron density. In the F region, where collisions are less frequent, recombination is a much slower process, and thus currents are able to flow in the F region even after sunset, while very little current is capable of flowing in the E region. This result is very important to the following discussions of the F region dynamo and the prereversal enhancement.

2.4 The Equatorial F Region Dynamo

It is well known that the neutral wind in the F region at the equator obeys a diurnal cycle. Winds are strongly eastward at night and westward during the day, reversing near sunrise and sunset. Solar heating is the primary driving mechanism of this reversal. Because the Coriolis parameter is approximately zero near the equator, the steady-state winds blow against the pressure gradient, from west to east across the solar terminator. In other words, the neutral winds blow from warm, sunlit air (high pressure) toward cooler, dark air (low pressure).

Near the equator, the neutral winds play a large role in determining the electric fields by driving currents in the ionosphere. The common form of the current equation is $\mathbf{J}' = \sigma \cdot \mathbf{E}'$, where the prime denotes quantities measured in the reference frame of the neutral particles. However, most measurements are taken in the Earth-fixed reference frame, where $\mathbf{E}' = \mathbf{E} + \mathbf{U} \times \mathbf{B}$. Thus, the current equation in the Earth-fixed frame is given by

$$\mathbf{J} = \sigma \cdot (\mathbf{E} + \mathbf{U} \times \mathbf{B}) \tag{2.12}$$

where each of these quantities is measured in the Earth-fixed frame. Taking the conventional notation of z upward, the magnetic field at the equator is represented as $\mathbf{B} = |\mathbf{B}|\hat{\mathbf{y}}$, which is horizontal and northward in geomagnetic coordinates, owing to the dipole geometry.

Taking the vertical component of the neutral wind to be very small, which is broadly true in the equatorial upper atmosphere, the current equation becomes

$$\mathbf{J} \cong \sigma \cdot (u\hat{\mathbf{x}} \times B\hat{\mathbf{y}}) \tag{2.13}$$

This wind-driven current is vertically upward, provided the wind u is eastward, with magnitude $J_z = \sigma_p uB$. The magnitude of J_z varies with altitude due to the dependence of σ_P on the product $n\nu_{in}$, as well as any vertical variation in the zonal wind, u. Typically the assumption is that viscosity keeps vertical variations in the zonal wind small, though results presented in Sections 4.3 and 4.4 show this is not always true near sunset. The vertical gradient of J_z means that an electric field must build up in the z direction in order to keep the current divergence-free. Assuming that current cannot flow along the magnetic field lines, i.e., that the magnetic field lines terminate in an insulating layer, imposes the condition that $J_y = 0$. Therefore, in order to maintain the divergence-free condition, i.e., $\nabla \cdot \mathbf{J} = 0$, we must have $\mathbf{J} = J_z = 0$, since $dJ_z/dz \neq 0$. Kelley (2009) employed a model of the evening ionosphere that treats the narrow peak region of σ_P as a thin slab with $\sigma_P = 0$ elsewhere. This is a reasonable approximation because, in the evening hours, recombination rapidly decreases the plasma density on the lower side of the F peak, and ν_{in} (and thus σ_P) falls off exponentially above the peak. Assuming a constant zonal wind, u within the layer, charges pile up at the two boundaries due to the vertical current driven by the neutral wind (eq. 2.13). In order to maintain $\mathbf{J} = 0$, the electric field that builds up must satisfy

$$J_z = \sigma_P E_z + \sigma_P u B = 0 \tag{2.14}$$

and, therefore,

$$E_z = -uB \tag{2.15}$$

This implies that the plasma within the slab will drift with an $\mathbf{E} \times \mathbf{B}$ velocity equal to in magnitude and direction to that of the neutral wind. The slab model leads to the prediction of plasma shears across the conductivity boundary, which have been observed with both radar (Kudeki et al., 1981) and barium releases (Valenzuela et al., 1980) (see Figure 2.12). Kudeki and Bhattacharyya (1999) later showed that the sheared drift profiles observed previously may be part of a much larger vortical flow structure that results from negative charging of the postsunset ionosphere as a result of the prereversal enhancement phenomenon (see Sec. 2.5.2). A more complete treatment that considers times when the field-line coupled E regions north and south of the equator are not perfect insulators is given by Kelley (2009). The end result is

$$E_z(z) = -[u(z)B\Sigma_P^F(z)]/[\Sigma_P^F(z) + 2\Sigma_P^E(z)] \tag{2.16}$$

At night, when the E region conductivity is very nearly zero, $\Sigma_P^F \gg \Sigma_P^E$ and this reduces to eq. 2.15. The dynamo electric fields that develop as a result of the neutral wind are critically important in the development of the prereversal enhancement that leads to the generation of equatorial spread F instabilities in the evening hours.

2.5 Spread F and possible seeding mechanisms

"Spread *F*" is the generic term for plasma instabilities occurring in the equatorial F-region ionosphere, though the term has come to be typically used to describe large plasma depletion plumes that occur just after sunset. The term was first coined by Booker and Wells (1938) during a series of ionosonde studies where the reflected echo was spread in range or frequency.

Dungey (1956) was the first to propose the Generalized Rayleigh-Taylor (GRT) instability as the process that gave rise to spread *F* plumes. As discussed in section 2.2, there is a sharp gradient in the electron density in the F region near sunset. Gravity is directed downward, antiparallel to the density gradient. This is an unstable configuration, and, given some initial perturbation of the boundary, large vertical perturbations will develop, analagous to the neutral fluid instabilities studied by Rayleigh (1883) and Taylor (1950). The plasma analog gives a net current in the x direction that produces perturbation electric fields that drive vertical $\mathbf{E} \times \mathbf{B}$ drifts, advecting the lower density plasma upward, once more feeding the process and creating instability (Kelley, 2009). In extreme cases the end result can be that massive plumes of lower-density plasma are thrust rapidly upward to heights well above the *F* region, producing spectacular backscatter at over 1000 km altitude. A textbook example of spread *F* is shown in Figure 2.6 (Kelley et al., 1981).

It is possible to linearize and solve the equations of motion in the *F* region in order to obtain plane wave solutions, e.g., $n = n_0(z) + \delta n e^{i(\omega t - kx)}$. Incorporating the effects of the neutral wind and any potential zonal gradients in the electron density, which would produce zonal electric fields, and assuming that the layer may be tilted at an angle Δ with respect to the vertical, the linear growth rate of the RT instability is given by Kelley (2009):

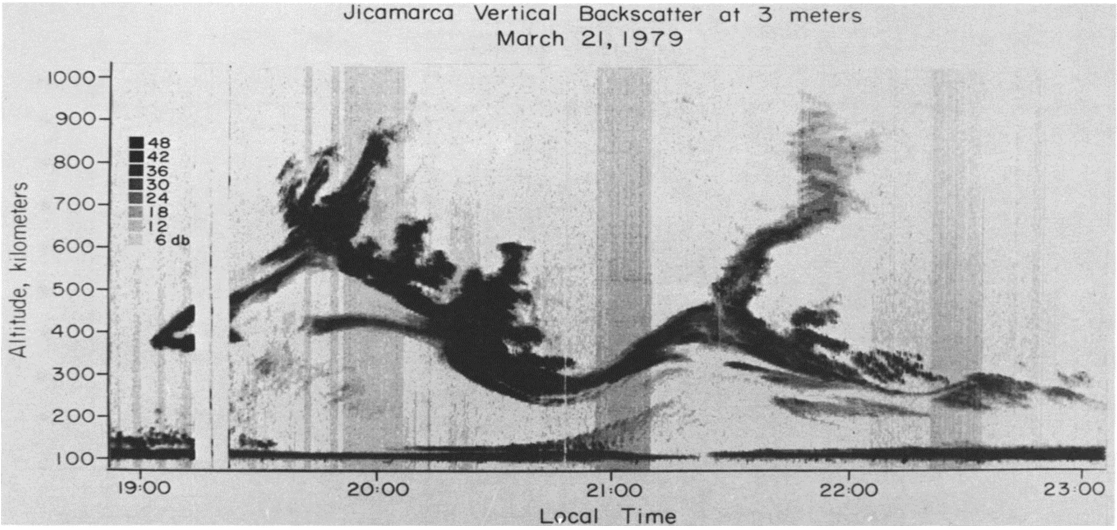

Figure 2.6: An example of spread F, as measured by the Jicamarca incoherent scatter radar. After Kelley et al. (1981). Note the plume development on the down-sloping parts of the F layer.

$$\gamma_{RT} = \frac{E_x - wB}{LB} cos\Delta + \frac{g}{\nu_{in} L} cos\Delta + \frac{E_z + uB}{LB} sin\Delta \tag{2.17}$$

where L is the gradient scale length, $L = [(1/n_0)\partial n_0/\partial z]^{-1}$. While the first terms will have the same contribution whether the tilt is positive or negative in Δ, the third term depends on the sign of the tilt angle, as well as the direction of the neutral wind. Presuming an eastward wind, an eastward-tilted layer (positive Δ) will produce a higher growth rate, while a westward-tilted layer will inhibit plume growth. Kelley et al. (1981) used this equation (sans w term, which they assumed to be zero) to interpret their observation that large spread F plumes were more likely to develop on the negative slope of the F layer height on the night depicted in Figure 2.6. They cited the eastward neutral wind as a contributor to the instability growth rate when it blows antiparallel to the plasma gradient, which occurs in the downward slopes of the F layer. It should be noted that, while the vertical winds in the F region are generally so small as to be negligible, possible contributions to the growth rate by means of the vertical wind, w can occur when gravity waves propagate vertically through the bottomside F region. Raghavarao et al. (1987) reported observations of vertical winds that varied with altitude, up to 42 m/s upward.

One particular consequence of the L^{-1} dependence of 2.17 for the linearized growth rate is that the growth rate scales directly with the vertical gradient of the background electron density, $\partial n_0/\partial z$, as well as inversely with the background density itself $(1/n_0)$. This means that the growth rate will rapidly increase if the postsunset F peak, which has a very sharp density gradient (see Figure 2.1), is lifted to a region of lower background electron density. In fact, as first discussed by Woodman and LaHoz (1976) and later by Sultan (1996) and Kudeki et al. (2007), without some sort of modulation of the base state, the GRT growth rate will be insufficient to reach the nonlinear stages of the instability, and thus will fail to produce the large plumes within the time frames after sunset in which they are normally observed. Thus, the generation of large spread F plumes is a two-step process beginning with some sort of seed perturbation that provides the necessary lifting of the F layer at sunset and initial instability growth, after which the nonlinear GRT process takes over.

The development of computer models that are capable of solving the non-linearized governing equations fully in 3-D is still ongoing. A discussion of current modeling efforts is given in Chapter 5. While these models are capable of producing realistic spread F development, given some set of background conditions, the processes that result in the background conditions necessary for instability development are still under investigation. These so-called "seeding mechanisms" of spread F are discussed in the following sections.

2.5.1 Direct gravity wave seeding of spread F and other external factors

The Rayleigh-Taylor model of spread *F* instability generation requires that the unstable boundary layer undergo some sort of perturbation in order to begin the instability processes, else the ionosphere would remain teetering on the edge of the unstable equilibrium. The prereversal enhancement (PRE) which can drive large vertical plasma $\mathbf{E} \times \mathbf{B}$ drifts that disturb the boundary layer, is one possible seeding mechanism (see Sec. 2.5.2). Because of its daily occurrence during peak spread *F* seasons and strong correlation to spread *F* activity, the PRE is generally regarded as the most consistent seeding mechanism of spread *F* irregularities (Kil et al., 2009). While the primary goal of this dissertation is to examine the *F* region neutral winds near sunset and their relation to the PRE and spread *F* development, it is worth noting the work that has been done studying the potential contribution of direct gravity wave propagation through the boundary region to perturbations that lead to full-blown spread *F*.

Huang and Kelley (1996a) conducted simulations of spread *F* development with varying background influences, including a neutral wind field that mimicked a vertically-propagating gravity wave. They found that the gravity wave was capable of seeding plume development on its own, though a plasma density perturbation, such as that generated by vertical plasma motions as a result of the prereversal enhancement, amplifies growth even further. Fritts et al. (2009) analyzed the influences of gravity wave propagation through the bottomside F layer and determined that gravity waves could have substantial influences on instability growth rates by directly perturbing the neutral wind and plasma drifts upon which the growth rates depend.

There have been a number of case studies conducted on individual spread *F* events in order to investigate the effects of gravity waves on the development of the instabilities. Kelley et al. (1981) examined the event shown in Figure 2.6 and concluded that it was possible for gravity waves to seed the spread *F* instabilities. Hysell et al. (1990) studied a very large spread *F* event that exhibited periodic layered structures that the authors correlated with gravity wave interactions. However, Kudeki et al. (2007) found that the neutral wind and PRE were much more dominant drivers of spread *F* and concluded that direct gravity wave seeding, while possible, is not a critical mechanism for daily spread *F* development, reaching the same conclusion as Fritts et al. (2009) that gravity waves primarily affect spread *F* by modulating the background winds and drifts.

In addition to gravity waves, several other external phenomena can have destabilizing effects on the equatorial ionosphere. The appearance of large-scale wave structure (LSWS) in the plasma density of the bottomside *F* layer has been suggested by Tsunoda (2005) to be a contributor to the day-to-day variability of spread *F* occurence. The wave-like nature of LSWS also causes the quasi-periodic spacing sometimes seen between plumes. Tsunoda (2006) later showed that LSWS may be initiated by the generation of a sporadic *E* layer at the base of the field line that maps to the base of the F_2 region, where plasma drifts are westward early in the evening.

The implication that sporadic *E* layers might contribute positively to the growth of spread *F* was contrary to the simulations of Carrasco et al. (2005), who showed that sporadic *E* layers near the equator were capable of reducing the prereversal enhancement amplitude by a factor of 3 (see Section 2.5.2), and thus suppressing its contribution to spread *F* growth. Testing this theory, Batista et al. (2008) conducted an experimental campaign in Brazil that found that sporadic *E* layers did not, in fact, correlate with reduced spread *F* occurrence. The study of Carrasco et al. (2005) considered sporadic *E* layers within 4° to 6° of the geomagnetic equator, while the sporadic E layers considered by Tsunoda (2006) would be located further off the equator in order to map to F_2 layer atltitudes. The conjugate observation stations where sporadic E was observed in the study of Batista et al. (2008) were located at +11.42° and -12.0° geomagnetic latitude, further from the equator than the layers considered by Carrasco et al. (2005). Whether the sporadic E layers help or hinder spread F growth may simply be due to their distance from the geomagnetic equator or whether there is some important physics missing is yet to be seen. Further study on sporadic E and its relationship to LSWS is required to fully understand their effects on spread F development.

Another potential external factor that modulates spread F occurrence is that of medium-scale traveling ionospheric disturbances (MSTIDs). Miller et al. (2009) showed experimental evidence that MSTIDs caused post-midnight spread F plasma depletions by mapping of polarization electric fields from MSTIDs, which are primarily a mid-latitude process.

The external modulations discussed in this section are of great interest to understanding the daily variations in spread F, since their occurrence individually is not necessarily described by the daily dynamo cycle that controls the rest of the mechanisms discussed below. While the new work presented in this dissertation is focused on the daily reversal of equatorial neutral winds at sunset, it is nonetheless important to understand that there are many external mechanisms that could potentially affect spread F development independently of the more regular, daily dynamo effects.

2.5.2 The Prereversal Enhancement

One source of the initial perturbation necessary to disturb the unstable equilibrium is the prereversal enhancement (PRE) of the eastward electric field. An eastward electric field drives a Pedersen current to the east. Any disturbance at the boundary will intercept this charge as it is transported and cause the perturbation to grow (Kelley, 2009). Thus, an eastward electric field is destabilizing, while a westward wind is stabilizing on the bottomside. A more succinct way of putting this is that the $\mathbf{E} \times \mathbf{B}$ direction be parallel to the plasma density gradient. The large PRE field observed near sunset contributes doubly to the destabilization of the F layer. First, it directly destabilizes the layer due to the eastward electric field; second, it drives the F layer upward, enhancing the destabilizing effect of the gravitational term.

The transition period is of particular interest to the generation of plasma instabilities in the ionosphere. Heelis et al. (1974) developed a model that considered horizontal conductivity gradients near sunset in the F-region dynamo system in addition to the vertical gradients described above. These east-west gradients give rise to an enhanced zonal field in order to maintain $\nabla \cdot \mathbf{J} = 0$. This enhanced zonal electric field drives vertical $\mathbf{E} \times \mathbf{B}$ drifts that are observed consistently by incoherent scatter radars in nearly every season and all parts of the solar cycle.

There are several different theories as to the generation of the PRE. The most widely known mechanism is likely that of Farley et al. (1986). A simplified schematic of the mechanism is shown in Figure 2.7 (Farley et al., 1986). Near sunset, as E region conductivities decrease, the eastward neutral wind in the F region drives the polarization electric field toward a value $-\mathbf{U} \times \mathbf{B}$. This field maps along field lines to an E region off the equator. In that E region, the field points meridionally equatorward. This tries to drive a westward Hall current, but the E region electron density drops sharply at sunset, meaning only very small currents are able to flow. Thus, there is much more current on the day side of the terminator, resulting in a divergence of currents. This leaves a buildup of negative polarization charges at the terminator, which drives an enhanced eastward field on the sunlit side, and an enhanced westward

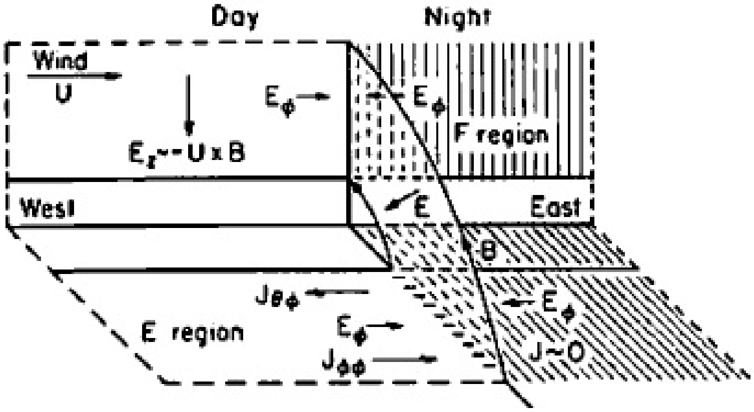

Figure 2.7: Schematic of the PRE development, originally produced by Farley et al. [1986]. The foreground represents the off-equator E region that is coupled to the equatorial F region.

field on the dark side.

Haerendel et al. (1992) proposed an alternative mechanism for PRE generation involving the equatorial electrojet. A strong eastward neutral wind at sunset drives a vertical Pedersen dynamo current. This creates a current divergence from below that causes a vertical polarization field (Rishbeth, 1971). This polarization field induces an opposing Pedersen current in an attempt to balance the dynamo current. The rapid changes in the electron densities and neutral winds that occur in the ionosphere near sunset prevent these two currents from properly balancing. Thus, there is a net vertical current demand that must be met from field-line-coupled *E* region north or south of the equator. However, the sharp drop in *E* region conductivity after sunset requires an increased eastward electric field in order to drag charges from the adjacent sunlit *E* region. This increased electric field then maps back up into the equatorial *F* region. This current-demand mechanism also contains a positive feedback mechanism, noted by Eccles (1998a): The vertical current and enhanced eastward electric fields continue to drag plasma vertically from the electrojet altitudes, which further reduces conductivity and demands even larger fields to supply current demand, which creates even larger prereversal electric fields.

The final mechanism, first proposed by Rishbeth (1971), is that of a curl-free response to the changing vertical electric fields. In this picture, the dynamo zonal winds are responsible for driving the large polarization fields at night, maintaining the fields even when the *E* region conductivities drop.

Eccles (1998a) examined each of these mechanisms in detail. The Farley et al. (1986) model is based on the Hall conductivity gradient in the *E* region off the equator that is connected by field line to the equatorial *F* region. The Haerendel et al. (1992) model relies on the Hall conductivity of the electrojet near sunset. Eccles (1998a) used both of these models with varying Hall conductivities to show that, despite drastic variations, Hall conductivity did not have a large effect on the PRE fields. Even when the conductivity was reduced nearly to zero outside the electrojet region, the PRE did not vanish. In other words, these mechanisms are not fundamental causes of the PRE; rather, they modulate it, and only very slightly. Eccles (1998b) developed an analytical model based on the descriptive comments of Rishbeth (1971) and found that it reproduced the PRE drifts. Ultimately, however, little discussion has been given to this result in the literature, with many papers still focusing on the Fareley and/or Haerendel mechanisms.

While there is still some uncertainty as to the exact physical mechanism that produces the PRE, there is no lack of observational data. Jicamarca has, for decades, produced vertical plasma drift measurements almost nightly [e.g., Fejer et al. (1991)]. Figure 2.8 shows the collected Jicamarca vertical drift observations from 1968-1992 under magnetically quiet conditions, separated by season and solar flux (Scherliess and Fejer, 1999). From this, the seasonal and solar flux variability in the PRE can clearly be seen. This variability has been strongly correlated to variability in the rate of occurrence of spread *F*. Ionosonde observations have also been routinely conducted

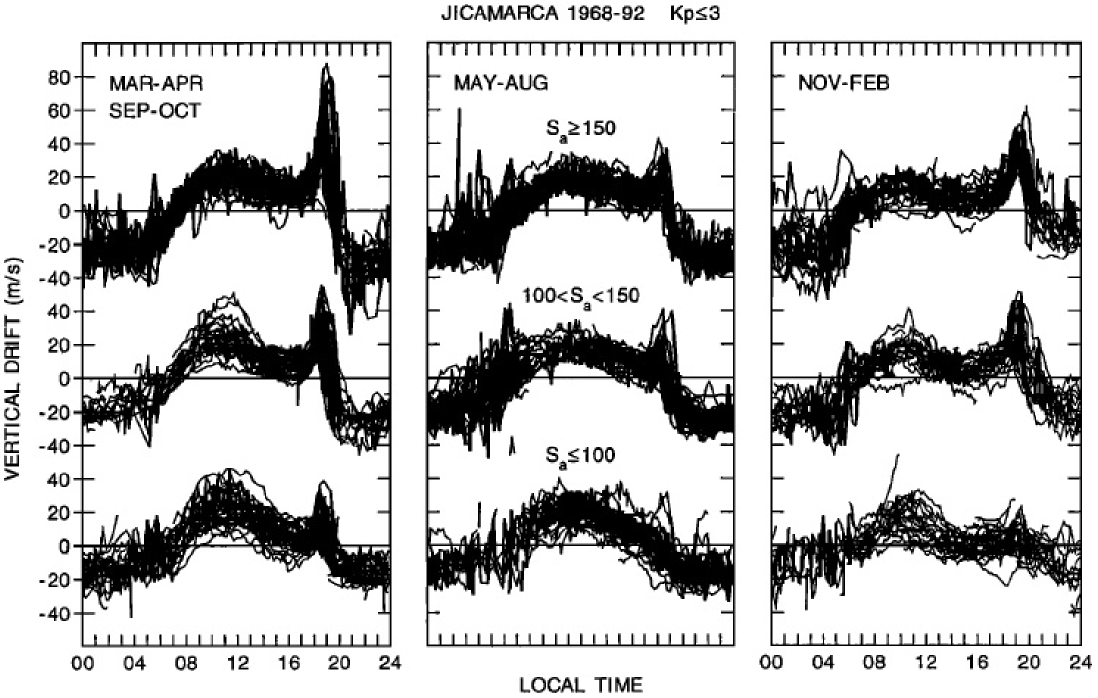

Figure 2.8: Scatter plot of Jicamarca quiet time vertical plasma drifts separated by season and solar flux conditions. After Scherliess and Fejer (1999).

and used to infer vertical *F* region plasma drifts [Sastri (1996); Batista et al. (1996)]. Satellite measurements of vertical ion drifts have also been derived by Fejer et al. (1995). Collecting these measurements, Scherliess and Fejer (1999) developed an empirical model for vertical drift magnitudes in all seasons and times of the solar cycle. This model is of particular importance to the work conducted here, as the model-derived vertical plasma drifts are used to compute background electric fields for the numerical model discussed in Chapter 5.

The correlation between PRE vertical plasma drifts and subsequent spread *F* development was investigated in detail by Kil et al. (2009). They used data from the ROCSAT satellite mission to produce a comparison between spread *F* plume occurence (referred to by the authors as Equatorial Plasma Bubbles (EBPs) and vertical plasma drifts during early evening hours. They found very strong correlation

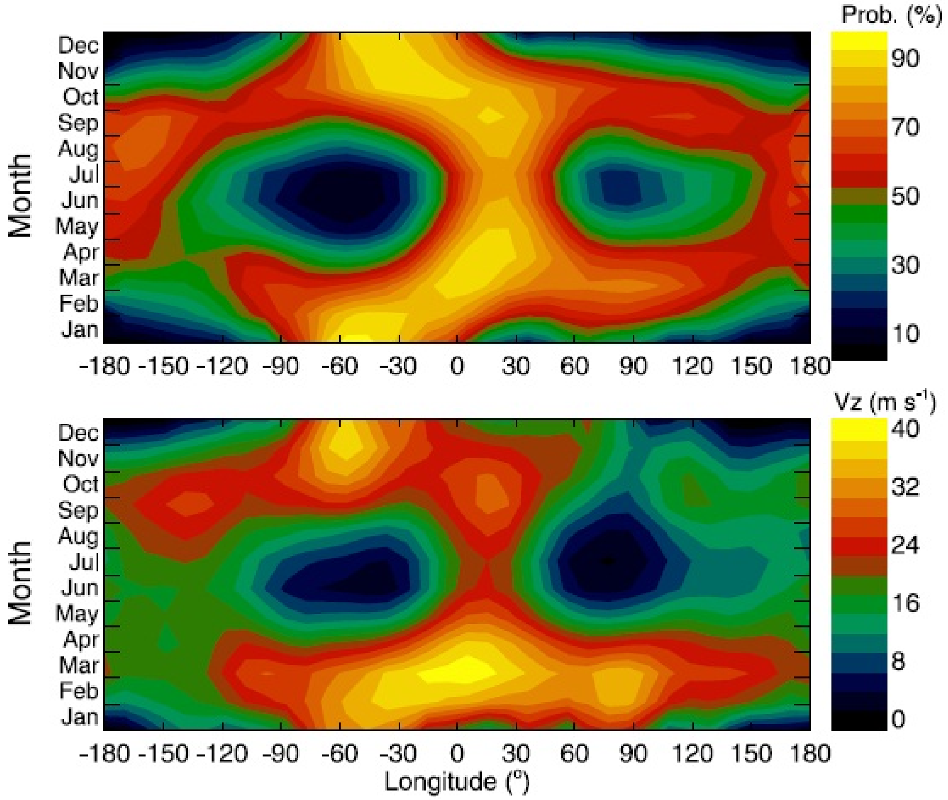

Figure 2.9: ROCSAT-1 data showing (top) Equatorial Plasma Bubble (EPB) occurrence as a function of month and longitude for the period between 1999 and 2002, for quiet geomagnetic conditions ($k_p < 3$) and (bottom) PRE magnitude as a function of month and longitude during the same time period. Figure from Kil et al. (2009)

between the magnitude of the PRE vertical drifts and the subsequent development of EPBs (see Figure 2.9).

The PRE itself is not itself the reason behind the large plasma bubbles commonly seen in spread *F* events, but it creates favorable conditions for instability events to flourish. A particularly famous observation of the PRE and the resulting vortex comes from Kudeki and Bhattacharyya (1999). The color plate is reproduced in Figure 2.10 and shows both plasma drifts and signal strength in the hours after sunset. A clear vortex is visible in the plasma drift vector, beginning with an upward PRE drift in the early evening. The vortical flow is also present in the bottomside region

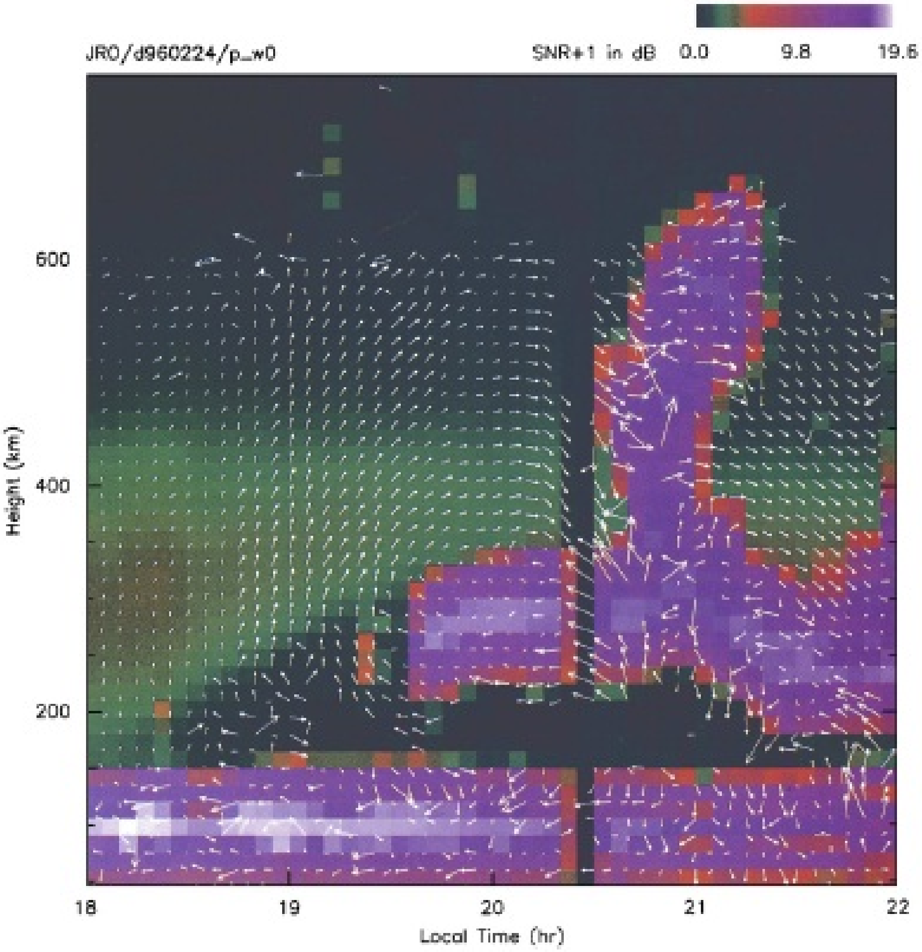

Figure 2.10: A particularly striking example illustrating the PRE drifts followed by the post-sunset vortex and the resulting bottom type spread *F* layer followed by a large plume. After Kudeki and Bhattacharyya (1999).

just before the spread *F* instability develops.

2.5.3 Wind-Driven E x B instability

While the neutral wind has long been thought to be a critical parameter in the generation of spread *F* due to the role it plays in the daily occurence of the PRE, more recent analyses have revealed that neutral winds also play a significant role in driving spread *F* by directly modulating bottomside instabilities. Kudeki et al. (2007)

examined the contribution of wind-driven $\mathbf{E} \times \mathbf{B}$ instability to the growth of spread F. They conducted a linearized stability analysis, finding that the growth rate can be given by

$$\gamma = \frac{km}{k^2 + m^2} U \frac{n_0'}{n_0} \tag{2.18}$$

where k is the zonal wavenumber, m is the vertical wavenumber, U is the zonal wind, n_0 is the ambient plasma density profile, and n_0' represents the vertical derivative of the plasma density. The factor n_0/n_0' is taken to be a plasma scale length, L. The growth rate in equation 2.18 is zero for purely horizontal wave motion (i.e., $m = 0$) or purely vertical wave motion ($k = 0$). It maximizes when $k = m$, which corresponds to an angle of 45° in the east-west plane. The maximum growth rate therefore reduces to

$$\gamma = \frac{U}{2L}. \tag{2.19}$$

While the Rayleigh-Taylor growth rates due to gravitational forcing and PRE vertical $\mathbf{E} \times \mathbf{B}$ drifts typically only produce 3-4 e-folds of growth within the first hour of sunset, equation 2.19 implies that an eastward neutral wind of 200 m/s in a region of typical plasma scale length of $L = 20$ km will produce up to 18 e-folds of growth during the same period for structures with an angle of 45° in the east-west plane (Kudeki et al., 2007). Given a strong enough u, the instabilities will combine to produce enough growth to feed the nonlinear stage of the GRT instability that leads to the rapid development of large spread F plumes. If u is not sufficiently strong, the instability processes will fail to produce enough growth for the nonlinear stages to take over, leaving behind only weak bottom-type spread F. A schematic diagram for this instability process is shown in Figure 2.11.

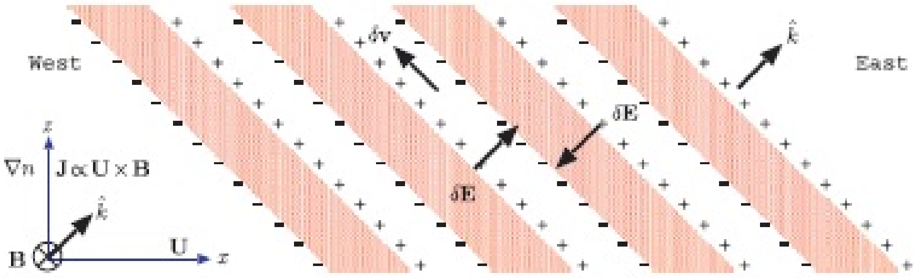

Figure 2.11: A schematic representation for the maximum growth mode of wind driven $\mathbf{E} \times \mathbf{B}$ instability. The induced vertical Pedersen currents (J), combine with the tilted wavevector $\hat{k}$ to produce the charge polarization structure shown. This produces polarization fields $\delta\mathbf{E}$ that carries the density depletions via $\delta\mathbf{E} \times \mathbf{B}$ drift in the direction of $\delta\mathbf{v}$, which is in the direction of increasing ambient plasma density, which causes further perturbation growth. Figure from Kudeki et al. (2007).

Preliminary modeling work conducted in the Kudeki et al. (2007) study showed that field-line coupling effects did reduce this linear growth rate from ∼18 e-folds per hour to 9-10 e-folds per hour. Nonetheless, this is still a substantial contribution to instability growth when compared with the slower growth rates of GRT instabilities in the bottomside region.

2.5.4 Collisional shear instability

Vertically sheared ion drifts, such as those shown in Figure 2.12, are a daily occurrence in the equatorial ionosphere. In fact, the sheared flow has been seen to develop several hours before sunset, intensifying near twilight (Hysell and Kudeki, 2004). While the existence of sheared plasma flow during postsunset hours has been known for decades (Kudeki et al., 1981), it was long thought to contribute to ionospheric stability rather than instability. However, such sheared flows are unstable to the plasma analog of the Kelvin-Helmholtz instability, which occurs in neutral fluids when the top of a wave is moving faster than the bottom, creating overturning and turbulence, akin to ocean waves breaking on shore.

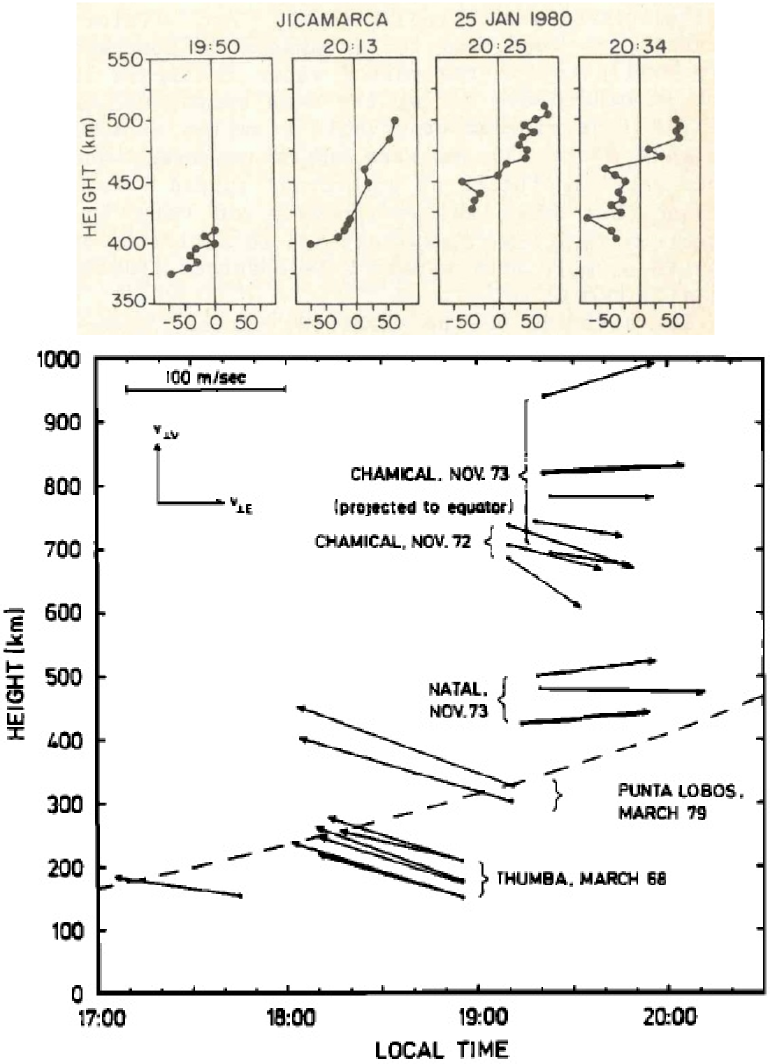

Figure 2.12: Examples of sheared plasma flow in the equatorial ionosphere. (Top) Zonal plasma drifts derived from the Jicamarca interferometry technique, after Kudeki et al. (1981). (Bottom) A collection of zonal plasma drifts measured by Barium releases in various locations, projected to the equatorial plane, after Valenzuela et al. (1980). The altitude of the solar terminator is plotted as a dashed line. Note that velocities reverse near the terminator, which rises with increasing local time.

First discussed by Satyanarayana et al. (1984) and Keskinen et al. (1988), electrostatic Kelvin-Helmholtz instabilities were dismissed as being unimportant because collisions and inhomogeneity of the atmosphere each reduced the growth rate of the instability. Hysell and Kudeki (2004), however, developed a model that was able to show that there were regimes in which the instability could exist and contribute to the growth of spread F irregularities, regimes which included the conditions present in the equatorial F region. The instability showed growth times of about 50 minutes, which were quite slow when compared with the growth times of the GRT instability. However, the sheared flow develops several hours before sunset, meaning that, despite its slow growth rate, collisional shear instability has time to undergo several e-folds of growth before the GRT instabilities take over, and thus it is possible that collisional shear instabilities contribute significantly to the seed perturbation that allows for full-blown GRT development. Hysell et al. (2005) investigated the possibility further, finding the growth rate of the collisional shear instability to be proportional to the flux tube integral of $(u - v_o)$, i.e., the difference between the neutral and plasma zonal drifts. Due to the development of sheared plasma flows, there exists a region of strong retrograde plasma motion, where the plasma drift is opposite that of the presumed eastward wind in the bottomside F region near sunset. They cited this region as an explanation for bottom-type spread F scattering layers, which are present in the retrograde areas.

Collisional shear instability was incorporated into the three-dimensional numerical model first desribed by Aveiro and Hysell (2010). In this work, the authors compared several model runs under different background conditions. The first case, which set neutral winds to zero, effectively suppressed shear instabilities. The resulting instabilities showed characteristics of GRT only, producing smooth, laminar plumes with no tilt or turbulent structure. The second case restored the neutral winds but set both the zonal electric field and gravity to zero. This suppressed GRT instabilities, leaving only collisional shear instabilities at work. The results of the model show plumes that are much more turbulent and structured, but the instabilities are confined to the bottomside region near the shear node. Neither GRT nor collisional shear instabilities alone are sufficient to produce realistic plumes on a wide scale. The final case that the authors studied restored all background parameters, allowing the instabilities to act together. This produced plumes with turbulent structure similar to that of the shear instability case, but with the vertical extent of the GRT case. The depletions are also significantly stronger in magnitude. Data from this paper is used for comparison in Chapter 5 and can be found in Figure 5.4.

The Aveiro-Hysell model is discussed further in Chapter 5, along with other contemporary models. We have used an updated version of the model to investigate the effects of measured neutral wind profiles on plume development.

2.6 Chapter Summary

Spread *F* is a collection of plasma instabilities in the equatorial ionosphere that arises from a plasma analog to the Rayleigh-Taylor neutral fluid instability. It produces large, turbulent plumes of plasma depletion that can penetrate to very high altitudes. These structures disrupt communications by changing the propagation path of E-M waves that pass through them. Understanding the mechanisms that generate spread *F* instabilities is key to predicting and mitigating their effects. There are three primary mechanisms by which spread *F* is thought to be seeded: through direct seeding due to external effects (Sec. 2.5.1), through prereversal enhancement (PRE) of the zonal electric field near sunset (Sec. 2.5.2), and through direct instability growth driven by the neutral wind (Sec. 2.5.3 and 2.5.4).

In each of the mechanisms discussed in sections 2.5.2 through 2.5.4, which operate on a daily basis near sunset, the F region neutral winds are of key importance. Instability growth as a result of these mechanisms is determined each night by the background atmospheric conditions near sunset, and the neutral winds are one of the primary factors. External mechanisms such as those discussed in Section 2.5.1 can also affect spread F growth, but we need to properly understand the daily mechanisms in order to correctly quantify the contributions of external factors. F region neutral winds are the least understood of the background parameters, and yet they are some of the most important modulators of daily instability growth.

As discussed in more detail in Chapter 3, the behavior of the winds are primarily understood through single-altitude satellite measurements or by vertically-integrated ground-based optical measurements, neither of which provide any information about vertical variations in the wind. New sounding rocket results, presented in Chapter 4, have produced vertically-resolved neutral wind profiles that are significantly more sheared and rapidly-evolving than expected based on single-altitude measurements. The implications of such sheared wind profiles on spread F development are examined in Chapter 5.

Chapter 3

Measurement techniques in the equatorial F region

There are a number of measurement techniques employed to probe the upper atmosphere. The parameters required to fully describe the physics at work are myriad, and no single technique provides an all-encompassing sample of the atmosphere. Each technique has its advantages and disadvantages, and these are outlined below. The experimental data presented in this work are a result of joint rocket-radar campaigns, with a focus on the chemical tracer results. More detail in the context of the experiments will be given to these techniques in Chapter 4.

In Chapter 2, we identified the neutral wind as a key driver of spread F instabilities, but measurements of thermospheric winds are few and far between due to the remote nature of the upper atmosphere. The objective of this chapter is to give a brief overview of the different experimental techniques relevant to the neutral and plasma dynamics of the F region. In particular, the unique perspective given by sounding rocket measurements allows us to fill the gaps in the other experimental methods discussed here.

3.1 Radar and other ground-based electrical techniques

The original observations of spread *F* came from ionosonde measurements. An ionosonde is a simple, yet reliable measurement device. It transmits over a range of frequencies and receives backscatter from areas of the ionosphere where the local plasma frequency (a function of the plasma density) is higher than the transmitted frequency. In a quiet, undisturbed ionosphere, the plasma density gradient is smooth with altitude, and thus the ionosonde will receive very clear backscatter at an altitude where the plasma frequency exceeds the ionosonde frequency. However, in the event of plasma instabilities, the plasma density gradient is disturbed, and lower density plasma is turbulently pushed to higher altitudes. This means that the return signal from the ionosonde at a particular frequency will not be from a well-defined layer. Rather, the signal is spread over a wider area, hence the term "spread *F*". The first published ionogram illustrating the spread in ionosonde return signal associated with spread *F* is shown in Figure 3.1.

The extension of low-frequency ionosonde measurements to frequencies higher than any plasma frequency expected in the atmosphere led to the development of large incoherent scatter radars (ISRs). With transmitters capable of delivering megawatts of power, ISRs receive incoherent backscatter from individual electrons in the ionosphere. This backscatter contains information about the electron and ion densities, temperatures, velocities, and the ion composition (Farley, 1969).

Coherent scatter involves Bragg scattering off structures with a scale size half the radar wavelength generated by instabilities within the background plasma. These instabilities create fluctuations within the plasma that are significantly larger than background thermal noise and thus create significant backscatter that can be detected

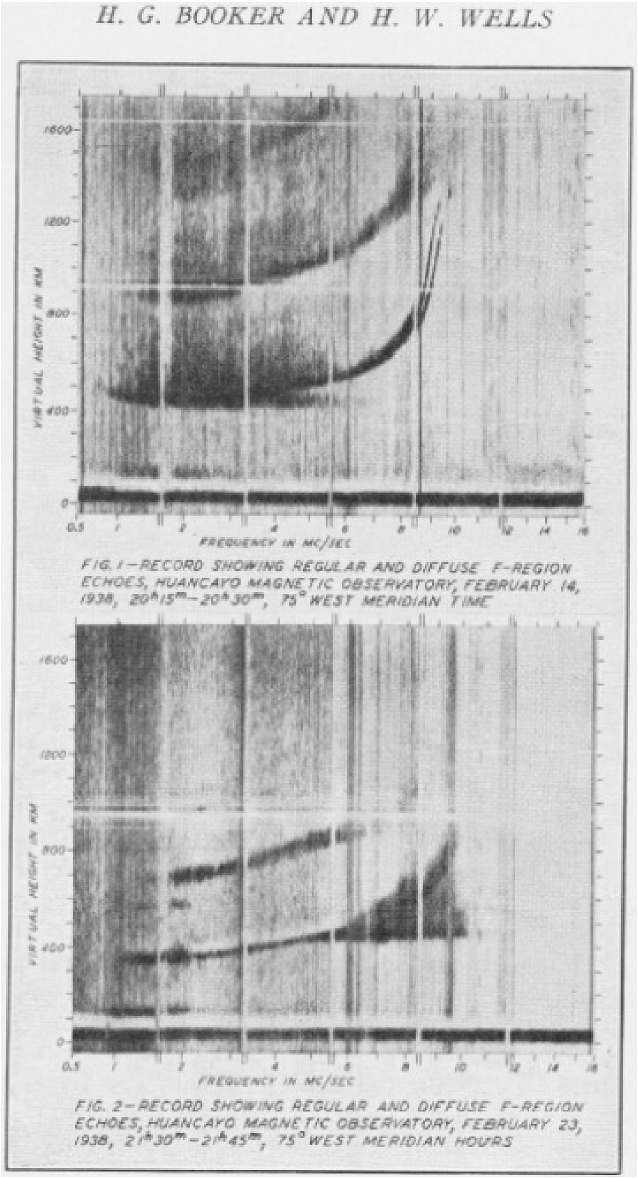

H. G. BOOKER AND H. W. WELLS

FIG. 1—RECORD SHOWING REGULAR AND DIFFUSE F-REGION ECHOES, HUANCAYO MAGNETIC OBSERVATORY, FEBRUARY 14, 1938, $20^{h}15^{m}-20^{h}30^{m}$, 75° WEST MERIDIAN TIME

FIG. 2—RECORD SHOWING REGULAR AND DIFFUSE F-REGION ECHOES, HUANCAYO MAGNETIC OBSERVATORY, FEBRUARY 23, 1938, $21^{h}30^{m}-21^{h}45^{m}$, 75° WEST MERIDIAN HOURS

Figure 3.1: The first published ionosonde measurement that illustrates the spreading of returned signals as a result of *F* region instabilities. After Booker and Wells (1938)

even with less powerful transmitters. Spread *F* instabilities, such as those shown in Figures 2.6 and 2.10, are an example of structures that can be detected using coherent scatter.

There are two radars that are widely utilized for spread F studies. The first and most well-known is the Jicamarca Radio Observatory, located near Lima, Peru (11.95° S, 76.87° W). This location falls very near the geomagnetic equator and makes it an ideal location to study equatorial phenomena such as spread F. The other radar that is sometimes used for spread F studies is the Agency Long-Range Tracking and Instrumentation Radar (ALTAIR) radar located in the Kawajalein Atoll in the Marshall Islands at 4° north geomagnetic latitude (9.38° N, 167.47° E geographic).

The Jicamarca radar operates at 50 MHz radar and is phase-steered with a range of about 3 degrees off vertical, allowing measurements to be taken slightly off-zenith as well as directly above the radar, providing some added spatial coverage. This narrow, near-vertical view is often thought of as a slit camera image (Kelley et al., 2011). Jicamarca is capable of operating in both incoherent scatter and coherent scatter modes. Incoherent scatter provides information about electron density, plasma temperature, and electric fields, based on doppler shifts and widths in the backscatter spectrum. In coherent scatter mode, the radar is used to track larger-scale plasma structures such as spread *F* instabilities, producing backscatter maps like those seen in Chapter 2 with a Bragg scale equal to half the radar wavelength, or 3 meters.

Originally designed for tracking ballistic missiles, ALTAIR is a fully steerable dish, with a slew rate up to 10° per second (Ingwersen and Lemnios, 2000). The radar operates at 160 and 422 MHz frequencies and, like Jicamarca, is capable of operating in both incoherent and coherent scatter modes. The steerability of the radar dish allows ALTAIR to effectively track spread *F* depletions as they propagate across the sampling volume throughout the night.

An incoherent scatter radar provides information about the electron densities, temperatures, and plasma velocity in the ionosphere at any time of day, while coherent scatter from instability structures allows us to track the movement and development of ionospheric instabilities. This flexibility has made coherent and incoherent scatter radars into a focal point for ionospheric studies, but it is generally quite difficult to obtain data about the neutral atmosphere from radar measurements, simply because the radar is incapable of directly probing the neutrals. It is possible to measure neutral drifts in the E region by exploiting the fact that the ion-neutral collision frequency, ν_{in}, is much larger than the ion gyro frequency in the E region, while the opposite is true of the electron-neutral collision frequency (Manju et al., 2012). The ion motions are thus controlled by collisions with neutrals, while the electrons are controlled by the magnetic field, meaning that the ion and neutral drifts are approximately equal. We can then solve the ion momentum equation, from Kelley (2009),

$$0 = e(\mathbf{E} + \mathbf{v_i} \times \mathbf{B}) - m_i \nu_{in} (\mathbf{v_i} - \mathbf{u}) \tag{3.1}$$

in order to obtain information about the neutral motions. A method of solving this equation from an incoherent scatter measurement is detailed by Heinselman and Nicolls (2008). However, in the upper E and lower F regions, this condition breaks down. The ion-neutral collision frequency drops rapidly due to the decrease in overall density of the atmosphere, and the neutral and ion drifts are no longer strongly coupled. We are thus forced to turn to other techniques to obtain information about F region winds.

3.2 Fabry-Perot Interferometry and airglow

In addition to electrically probing the *F* region ionosphere, we are also able to remotely gather information about the neutral thermosphere by optical methods. Atomic oxygen, the primary ion constituent in the F-region, undergoes a two-step recombination process that produces two well-known emissions at 630 nm and 557.7 nm. Using narrow filters, it is possible to isolate these atomic transitions from the background sky. Two types of instruments commonly utilize these emissions: airglow images and Fabry-Perot interferometers.

Airglow imagers are typically all-sky cameras, meaning they have a very wide field of view that includes all of the sky visible from that particular ground location. These produce large-scale image sequences that can be used to study the motion of ionospheric irregularities that propagate through the region, disturbing the background O^+ concentration. Spread *F* signals are observed as dark spots due to the plasma depletions in these images, i.e., regions of low O^+ concentration (and thus low recombination) that correspond to the plasma depletions that result from the development of the Rayleigh-Taylor instabilities. Airglow imagers typically have very wide fields of view that can cover hundreds of kilometers, making them useful for studying the structure and propagation of spread *F* depletions (e.g., Krall et al. (2009)). An example of spread *F* observations using an airglow imager is shown in Figure 3.2.

Fabry-Perot interferometers (FPIs) acquire spectral information about a line-of-sight integrated signal. Velocities and temperatures are obtained from the Doppler shift and line broadening, respectively. FPIs have been used extensively in the South American sector in conjunction with Jicamarca radar measurements (Meriwether et al., 1986). They are optics-based instruments, meaning they cannot operate in poor sky conditions or in daylight, but they are otherwise reliable and able to operate

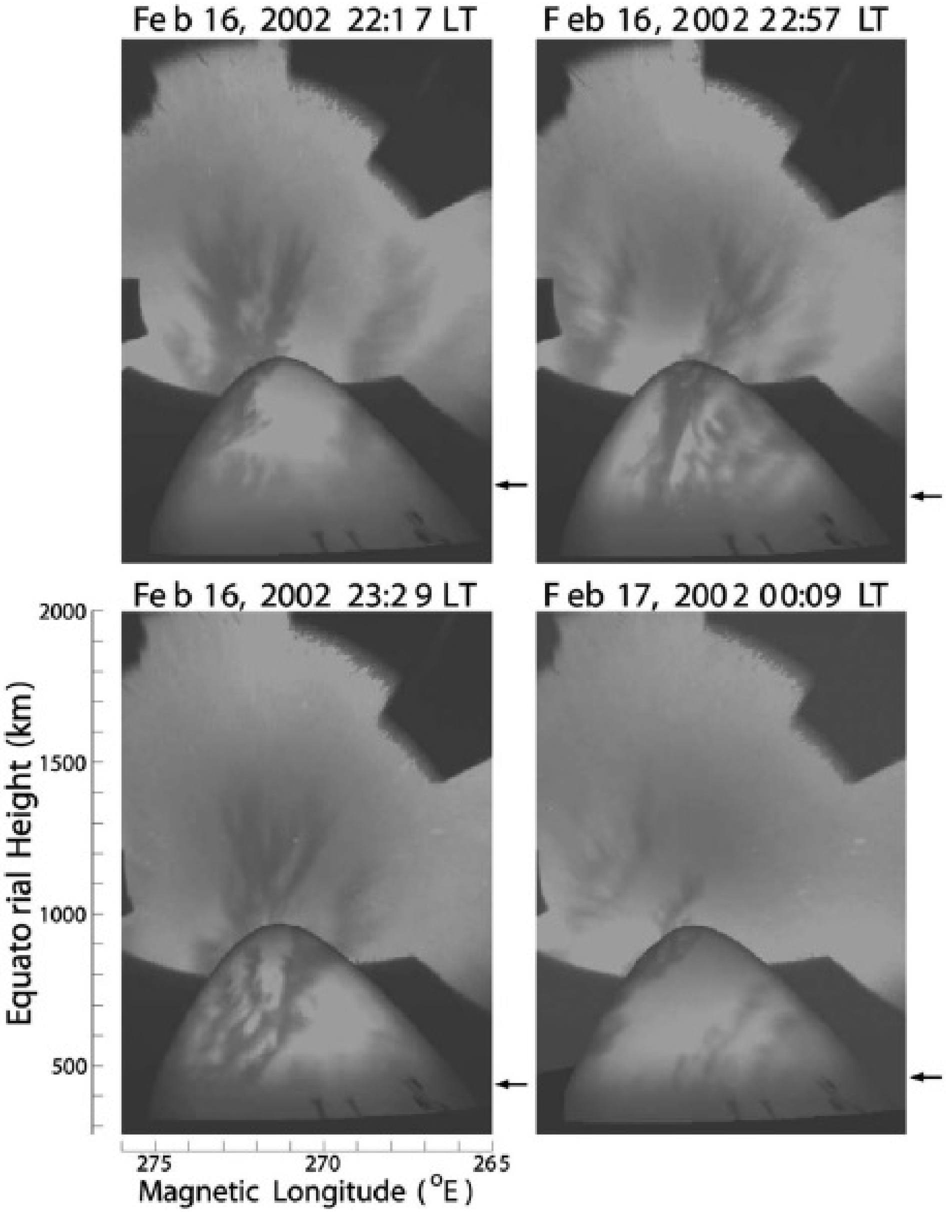

Figure 3.2: Example of spread F depletions observed in an airglow imager on top of the Haleakala Volcano in Hawaii. The dark patches in the images represent the plasma depletions associated with spread F. After Kelley et al. (2002)

nearly every day once installed. This makes them useful for climatological studies of neutral wind behavior near the F peak after sunset.

The primary limitation of FPI and other optical measurements is that they are derived from a line-of-sight integration of the optical emission. The emission reaches a maximum between 250 and 300 km depending on the altitude of the F peak. This produces a single data point in altitude that is positioned at the maximum of the emission profile, but this does not give any information about the vertical structure of the winds. The measurements are further limited by the requirement for darkness in the viewing area, since the broad spectrum of sunlight will contaminate any optical data. This means that measurements cannot begin until there is significant darkness. Because the neutral wind reversal from daytime westward flow to nighttime eastward flow occurs near sunset, FPIs often fail to capture the transition from westward to eastward winds in the F region.

3.3 In-situ Measurements

Ground-based remote sensing techniques comprise the longest-running ionospheric data sets thanks in large part to the simple practicality of their installation and operation. However, they have many limitations in what they can tell us and how accurate they can be. It is therefore desirable to conduct *in situ* measurements in order to obtain direct, high-resolution information about the dynamics of the F region, as well as for validation of ground-based results. This is done either by use of sounding rockets that fly through the F region or by use of satellites that orbit there. Much of the instrumentation that is capable of measuring plasma parameters is common between these two methods, but they measure neutral winds in different ways.

Satellite missions allow for long-term *in situ* studies of the upper atmosphere and thus are desirable for climatology studies. However, most satellites maintain a small range of altitudes throughout their orbit and measure only locally, meaning they cannot provide any information about vertical gradients in atmospheric parameters. There are exceptions to this, which will be discussed below.

Sounding rockets operate on the other end of this spectrum. They fly in parabolic trajectories, up and down within a few minutes. This allows them to provide information about vertical gradients, but makes them ill-suited for any climatology studies because each rocket effectively provides just a pair of snapshots of the atmosphere, one on the way up and one on the way down.

3.3.1 Satellite neutral wind measurements

The most typical method for measuring neutral winds in recent years via satellite is by use of a very precise accelerometer (Doornbos, 2012). Once the satellite enters orbit, an accelerometer can detect small perturbations in the satellite's orbit due to forcing by neutral winds. Because the densities are so low, even a fast wind will produce only a very small acceleration on the satellite. This requires very precise calibration of the accelerometer (e.g., van Helleputte et al. (2009)).

There have been many satellites, such as CHAMP (Reigber et al., 2002), and GRACE (Tapley et al., 2004) that have produced F region neutral wind data in the past; however, the orbits of these satellites are nearly polar, meaning they sample along a line of constant longitude from north to south (or south to north) without changing altitude significantly. The DE-2 satellite also produced wind measurements in a similar orbit using a spectrometer (Spencer et al., 1982). Over time, this type of orbit provides good local time coverage of the winds, but this does not give us any information about potential vertical variability, only information about the local time changes in the winds at the altitude of the satellite. Moreover, it generally takes a long time for satellites to sample all local times near one location. For example, it takes the CHAMP satellite 90 days to do so (Liu et al., 2009), meaning it cannot tell us anything about how the winds evolve over the course of a full night, at least not on any given night.

An example of what these polar-orbit satellites *can* tell us about neutral wind behavior is shown in Figure 3.3.1. These measurements show a strong eastward neutral wind jet near the equator during the magnetic evening hours (Figure 3.3.1, top), but, most importantly, it shows that this jet follows the geomagnetic equator rather than the geographic equator, indicating that there is a strong magnetic influence on the neutral wind behavior, which the authors attribute to ion drag forcing.

The only satellite to date capable of taking neutral wind measurements in an equatorial orbit was the Communication/Navigation Outage Forecasting System (C/NOFS) satellite was launched in May 2005. Its primary objective was to study the processes that drive spread F through direct measurements of ionospheric parameters, with the ultimate goal of developing a forecasting system for predicting when spread F is likely to occur (de La Beaujardiere, 2004). The satellite was launched into a low-inclination (13°) orbit, meaning that it remained near the equator at all times. The orbit was elliptical, with initial apogee near 850 km and perigee near 400 km (Huang et al., 2013).

Unfortunately, problems with the neutral wind sensor aboard C/NOFS have meant that no neutral wind data has yet to be released. The elliptical, low-inclination orbit could have provided good coverage of multiple altitudes at the same local time so that any vertical variability in the average wind field at a given local time could be assessed. To date, there has been no satellite with a similar orbit that has produced

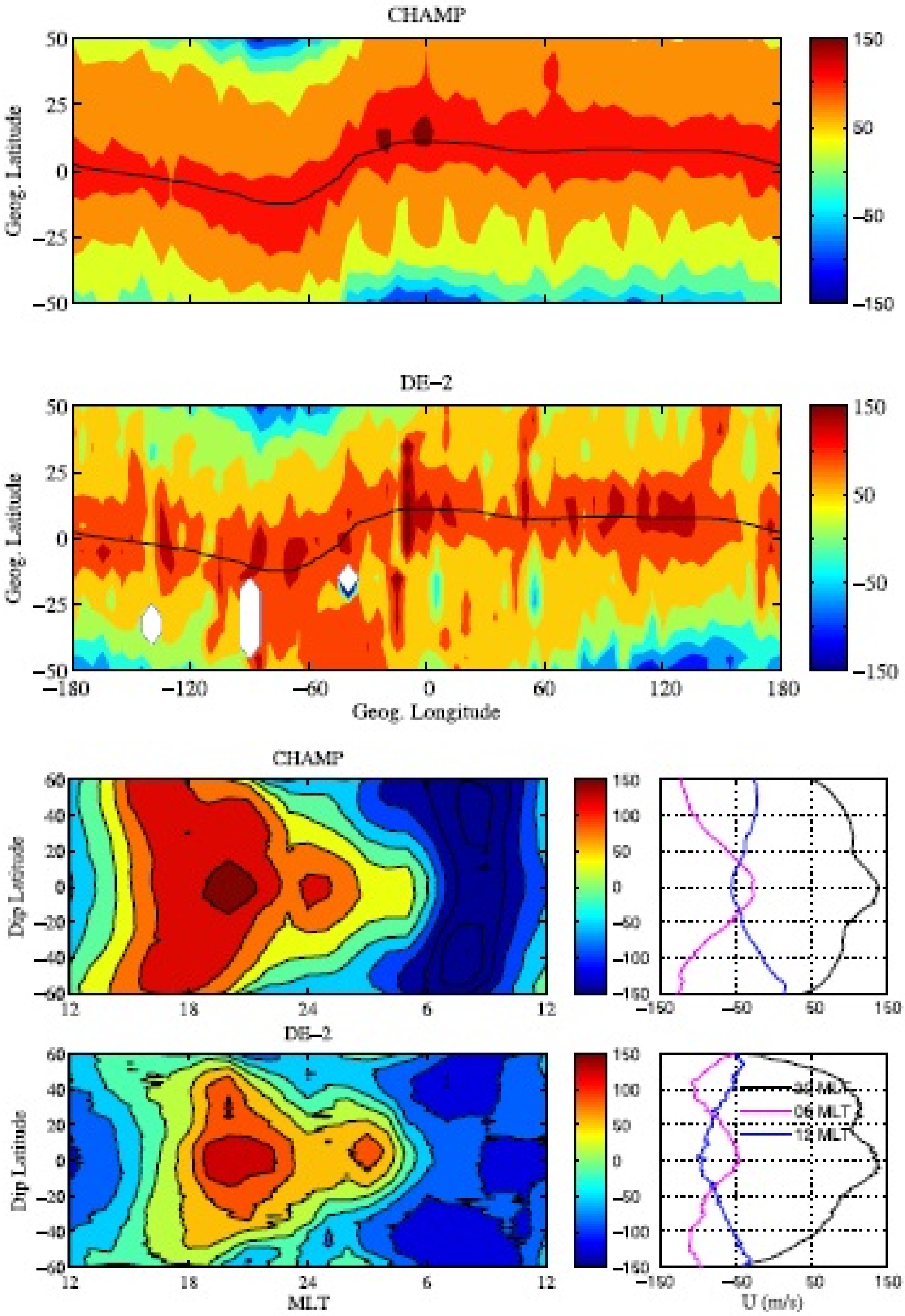

Figure 3.3: Comparison of CHAMP and DE-2 neutral wind measurements from two perspectives. (Top): Comparison near the geomagnetic equator in the 18-24 magnetic local time sector. (Bottom): Local time distribution of seasonally averaged winds, along with corresponding latitudinal profiles at three magnetic local times. Altitude for CHAMP was approximately 410 km during 2002. DE-2 had a much more variable altitude, ranging between 200 and 700 km during its measurement period. Figures from Liu et al. (2009).

neutral wind data in the *F* region.

Another technique that has recently been developed to measure neutral winds with satellites is the use of optical data to derive winds, much like ground-based FPIs. Satellites have the advantage of looking at angles other than roughly vertical, meaning they can resolve winds as a function of altitude. The TIMED satellite carries The TIMED Doppler interferometer (TIDI), which is one such instrument (Killeen et al., 1999). The satellite operates in a limb scan configuration, which allows it to probe the airglow layers of the upper atmosphere. Neutral winds can be computed from the doppler shift in the airglow emission. Both TIDI and an older instrument, WINDII (Shepherd et al., 1993) were capable of taking oxygen red line measurements in the *F* region similar to ground-based techniques. However, the data quality of the nighttime *F* region measurements from these instruments is questionable, and the data has not been widely used as a result. The WINDII nighttime data at low latitudes contained unexplained offests that contributed to discrepancies with observational data (Drob et al., 2015).

3.4 Sounding rocket neutral winds

The idea of deploying a visible chemical trail from a rocket in order to track air motions dates back to the work of Bates (1950). Various tracers have been tested over the years, with the most prevalent being trimethyl aluminum (TMA). Other tracers include sodium, lithium, barium, neodymium, and samarium. These tracers are released along the rocket trajectory, where they fluoresce either by chemical reactions with the ambient atmosphere or by photoexcitation from sunlight. The majority of chemical release experiments have focused on the E region and lower F region below 200 km. Above 200 km, rapid diffusion of the tracer renders analysis difficult. These difficulties, and how they can be overcome, are discussed further in Chapter 4.

TMA releases have many advantages that have made them the most common among chemical release experiments. Foremost, TMA reacts with ambient atmospheric oxygen, even in the absence of sunlight, to produce AlO, a reaction which produces a vibrant chemiluminescence that can be tracked via photography from the ground (Rosenberg et al., 1963). It also has blue resonant emissions that occur when it is sunlit (see Chapter 4). TMA also exists in its stable state as a liquid, which makes it much more easily manipulated than other tracers that exist as solids and must be vaporized by high-temperature reactions. This allows for the TMA release to be easily controlled via a solenoid valve (Larsen, 2002).

In the E and lower F regions, the TMA releases form distinct, narrow trails along the rocket trajectory. These trails are rapidly distorted by the neutral wind and gradually thin out due to molecular diffusion. The drift and contortion of the trail over time can be triangulated using photographs from several look angles to find the atmospheric wind profile (Groves, 1960). Modern rocket triangulation is semi-automated thanks to advances in computer analysis. Ingersoll (2008) developed the triangulation code that we have used to obtain the neutral wind measurements presented in Chapter 4. In essence, this routine uses the background star field in camera images to convert image coordinates to equatorial coordinates (right ascension and declination), which then allows for the projection of the line-of-sight from one image to the next. Along that line-of-sight, we can track individual points on the rocket trail. An example of a TMA triangulation is shown in Figure 3.4

Above 180 km, diffusion is much more rapid and other, brighter tracers must be used. Barium, which also contains a fraction of Strontium, is the most commonly used ionospheric tracer, but it ionizes rapidly, leaving only a small neutral constituent that can be difficult to track. The addition of strontium to the mixture helps to intensify

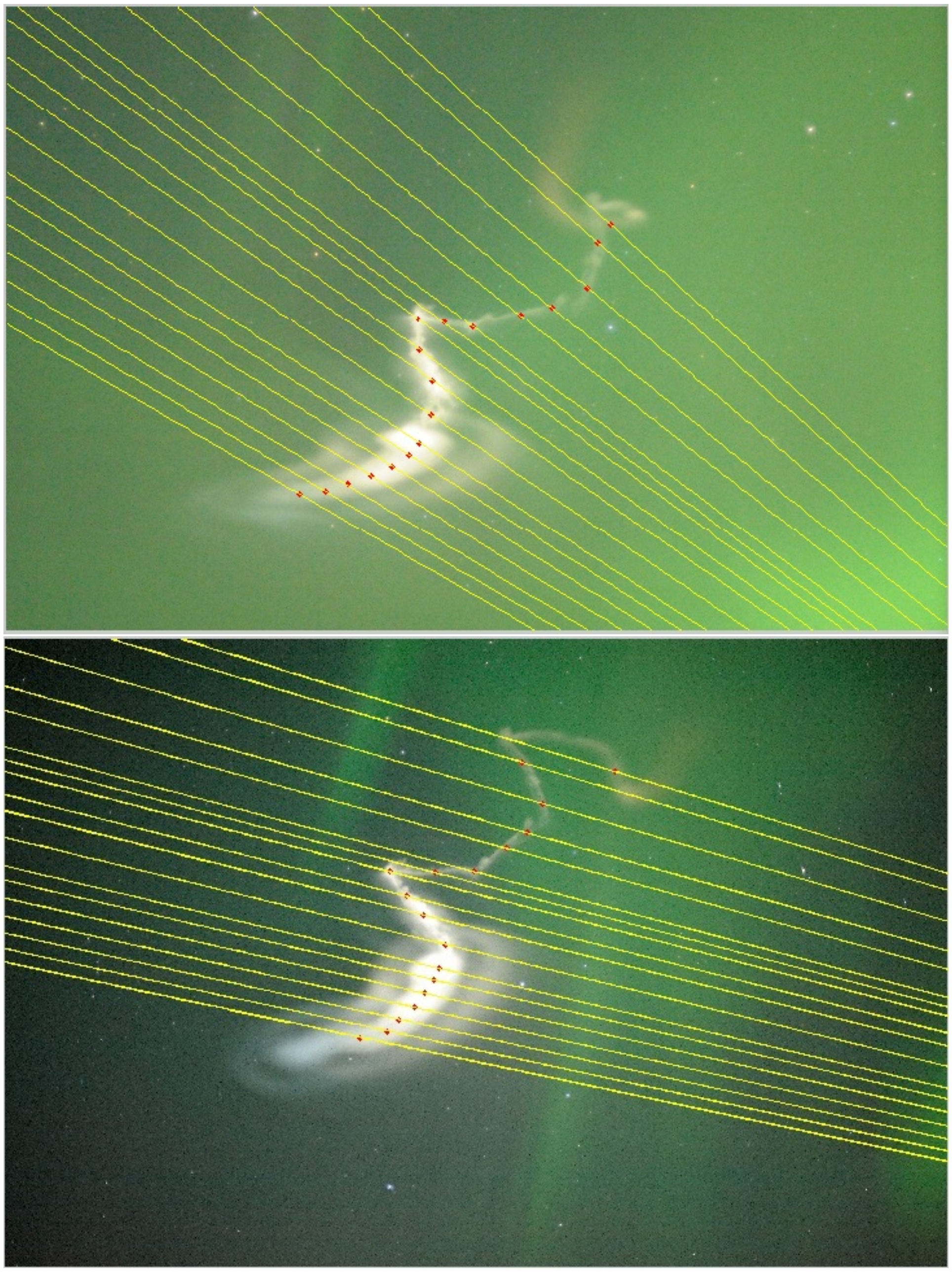

Figure 3.4: Example of line-of-sight projection in a chemical tracer triangulation. Each of the points on the trail will produce a three-dimensional position based on the image pixel coordinates of the point and its corresponding pair in the second image. These images were taken from an auroral rocket launch, the MIST/M-TEX campaign Poker Flat, Alaska, but the triangulation procedure remains the same for equatorial launches.

the neutral emissions. Recently, lithium has become more widely used, both because it remains neutral in the F region and because it has a well-defined fluorescence near 670 nm, enabling daytime releases using narrow filters to track the cloud. Both barium/strontium and lithium measurements in the F region are shown in Chapter 4.

3.4.1 Other in-situ measurements

In addition to neutral wind measurements, sounding rockets and satellites are capable of carrying instrumentation that can measure plasma parameters as well as atmospheric density and composition. Because C/NOFS contributed data to one of the experiments that is a part of this study, we will use it as an example. C/NOFS contained five instruments besides the previously mentioned neutral wind sensor that are overviewed by (de La Beaujardiere, 2004). A Langmuir probe (e.g., Jahn et al. (1997)) measured electron density and temperature, as well as the power spectral density of the electrons. An ion velocity meter measured the ion drift vector, ion temperature, and ion composition.

C/NOFS also combined with GPS satellites and ground receivers to gather information about electron density. It contained a tri-band radio beacon, which was used in scintillation studies in order to determine plasma conditions between C/NOFS and the Earth. The distortion of the signal at different frequencies provided some idea of how much turbulence was in the plasma beneath C/NOFS. The satellite also featured a dual-frequency GPS receiver that could measure total electron content along the line-of-sight between C/NOFS and a GPS satellite. This allowed for reconstruction of electron density profiles through combination of many line-of-sight TEC measurements.

The Vector Electric Field Instrument (VEFI) consisted of three orthogonal double probe antennas that measured electric fields. Similar sensors are deployed aboard rockets (Pfaff et al., 1998). The potential difference between each orthogonal set of probes gives a measurement of electric fields in two directions, and an estimate for the complete vector $\mathbf{E}$ is determined by assuming $\mathbf{E} \cdot \mathbf{B} = 0$. Measurements from C/NOFS were included as a part of the EVEX campaign, which is discussed in Chapter 4. An example of data from a C/NOFS pass near the EVEX experiment can be found there, in Figure 4.9.

More recently, a probe capable of measuring E region neutral winds has been developed by Manju et al. (2012). It employs the same principle for measuring winds with incoherent scatter. Because the neutrals and ions are strongly coupled at E region altitudes, a measurement of ion velocity is approximately a measurement of the neutral wind. The probe collects ions by applying a negative potential to attract the positively charged ions (NO^+ and O_2^+, primarily). The applied potential will impart some velocity, $\mathbf{V_i}$ to the ions, which are drifting along with the neutrals with a velocity $\mathbf{v_i}$. Thus, when oriented in the direction of the flow, one arm of the probe will collect ions with a velocity of $\mathbf{V_i} + \mathbf{v_i}$ and the opposite end will collect ions with a velocity of $\mathbf{V_i} - \mathbf{v_i}$. This means that each end of the probe will encounter a different net current, from which the ion velocity (and thus neutral velocity) can be calculated. Just as with measuring winds from incoherent scatter, this technique is limited to E region measurements only, where the ions and neutrals are strongly coupled. For this reason, chemical tracer measurements remain the primary method through which we can obtain vertically resolved neutral wind profiles in the F region.

3.5 Chapter Summary

In this chapter, the most widely-used experimental methods for studying the Earth's upper atmosphere were presented. Of the techniques that can measure neutral winds, which are a key driver of the sunset processes that can lead to the development of spread F, only sounding rocket chemical tracer experiments provide reliable vertically-resolved measurements. What we currently know of F region neutral wind behavior is primarily derived from satellite and ground-based optical techniques that do not provide the vertical resolution of chemical release techniques. They do, however, provide consistent, daily measurements that sounding rockets cannot, making each of these techniques valuable assets for F region studies that can be used in conjunction with sounding rocket experiments to produce full snapshots of the upper atmosphere.

Chapter 4

F Region Sounding Rocket Measurements

As discussed in Chapter 2, the zonal neutral wind near sunset is a key driver of nighttime ionospheric instabilities. Measurements of F region neutral winds by satellites or ground based optics are very limited in in what they can tell us about vertical variations in the wind field. Previously, this was not of large concern, since zonal winds are typically assumed to be constant with altitude above ~200 km near and after sunset, due to the large increase in effective atmospheric viscosity that inhibits the development of vertical shears in most cases (Drob et al., 2008). In this chapter, we present new vertically resolved E and F region neutral wind measurements conducted near sunset from three sounding rocket experiments that show that the assumption of no vertical gradients in the zonal winds near sunset may not be valid at all times.

Described in this work are three sounding rocket campaigns that were carried out in northern Brazil and in the Kwajalein Atoll in the Marshall Islands. The first, earlier experiment was carried out close to the autumnal equinox, and the latter two close to the vernal equinox. The results from the *F* region releases show a remarkable consistency in spite of the large difference in location and time of year, as described in detail below. Barium/strontium releases were used to obtain plasma drifts and neutral winds in the Brazil experiment. Lithium and samarium were used to obtain the neutral winds in the Kwajalein experiments.

4.1 Motivation: Background and Previous Experiments

The experiments and data analysis carried out in this work represent some of the only vertically-resolved measurements of the bottomside *F* region neutral wind. However, there have been several campaigns aimed at studying the ionospheric sunset dynamics near the equator that generated the motivation for the *F* region wind measurements conducted in the two campaigns discussed here.

The earliest rocket experiment conducting *in situ* measurements of spread *F* was launched in 1973 from Natal, Brazil. This early experment focused on analyzing the power law behavior of the bottomside electron density power spectrum in order to identify the scales on which spread *F* acts (Costa and Kelley, 1978). Before chemical release measurements were a part of spread *F* study, rocket measurements were used in the context of spread *F* primarily as a source of high-resolution, vertically resolved electric field measurements, which yields information about the scales on which the instabilities operate.

Building on the early result, the PLUMEX campaign was conducted in the Kwajalein Atoll in 1979. This took the measurements a step furthier, combining sounding rocket probe measurements with ALTAIR backscatter measurements at 0.96

and 0.36 m (Szuszczewicz et al., 1980). The rocket probes took plasma density measurements during a spread *F* event, as well as measured the electric field fluctuations and ion composition. Kelley et al. (1982) used the power spectrum of the electron density fluctuations to determine the scales at which the instabilities operate, finding a power law spectrum that produced good agreement with the ALTAIR backscatter at 0.96 m.

Two rockets were subsequently launched as a part of project Condor in Peru, along with ground support from the Jicamarca radar, a Fabry-Perot interferometer, and several other small radars and ionosondes (Kelley et al., 1986). These rockets took measurements of densities and electric fields that were presented by LaBelle et al. (1986). The results of the Condor launches showed a similar power-law dependence of the electron density spectra, with breaking near scales of 100 m, which showed that spread *F* instabilities operate over a wide range of scales, from hundreds of km down to a few meters, spanning both the inertial and diffusive subranges.

Following the PLUMEX and Condor experiments, a second campaign was carried out at at Kwajalein in 1990, the EQUIS/CRRES campaign. Based on the earlier results of Kelley et al. (1986), the EQUIS rockets flew with refined instrumentation capable of producing measurments of the plasma density spectrum spanning wavelengths from 10 m to tens of km (Hysell et al., 1994b). EQUIS once again combined rocket and radar measurements from both ALTAIR and a the Cornell 50 MHz (3-meter) portable radar interferometer (CUPRI) on Kwajalein (Hysell et al., 1994a).

Absent in these experiments were chemical tracer measurements. The first extensive equatorial campaign using chemical tracers to investigate neutral winds took place in 1994 in Brazil. Launched as a part of the Guara campaign, two rockets flew on each of two consecutive nights. In each of these salvos, a barium cloud was released in the *F* region, along with *E* region TMA trails near the barium release and about 480 km north, near the base of the *F* region field lines where the barium was released.

The collisional shear instability theory of Hysell and Kudeki (2004) was not yet developed at this time, and so the primary concern of the barium *F* region release was a measurement of the ion drifts. This, combined with poor seeing conditions on the night of the launch, meant that the *F* region neutral barium release was never analyzed. However, modern computer analysis and enhanced film digitization technology has allowed us to revisit the Guara barium measurements as a part of this work. Further discussion on the Guara campaign is given in section 4.3.

The next equatorial experiment incorporating neutral wind measurements was the EQUIS II experiment, which took place in August, 2004, once again in the Kwajalein Atoll (Hysell et al., 2005). A chemical release payload was included, but releases only occurred in the *E* region. Nonetheless, the EQUIS II experiment showed that the preferred wavelengths observed in the plasma irregularities matched with the collisional shear instability modeled by Hysell and Kudeki (2004). As discussed in Chapter 2, the difference in the zonal wind and ion drifts is the key driver of collisional shear instability. This led to the conclusion that an experiment simultaneously measuring the *F* region zonal wind and plasma drifts could be useful for future spread *F* forecasting. To that end, the second campaign discussed in this work, the EVEX/MOSC campaign, was proposed to measure simultaneously *E* and *F* region winds in conjunction with ground-based radar measurements. Further discussion on EVEX/MOSC is given in Sections 4.4 and 4.5.

4.2 The Chemical Tracer Method

Sounding rocket chemical release experiments have provided accurate in-situ neutral wind measurements in the mesosphere and thermosphere for five decades. Larsen (2002) collected and studied many such *E* region measurements. Many chemicals have been used as tracers, with the most common being trimethyl aluminum (TMA), barium, strontium, lithium, and sodium. The latter four require solar illumination in order to excite the atomic transitions that make them visible. Their use is thus mostly restricted to twilight conditions, where the high altitude releases can be sunlit, but ground-based camera sites have enough darkness to photograph the releases. Daytime lithium measurements have also been conducted using narrow filters in order to observe the dominant transition (Bedinger, 1973). Barium ionizes rapidly, when exposed to solar radiation, which enables ion drift observations in addition to the neutral wind measurements from the motion of the residual neutral barium cloud (Mendillo et al., 1989). Neutral strontium produces a bright emission that significantly enhances the cloud visibility.

TMA releases are ideal for *D* and *E* region measurements (Larsen, 2002). The reaction of TMA with ambient oxygen in the atmosphere produces chemiluminescence even in the absence of sunlight, making it possible to conduct measurements at any time of night. Compared to other tracers, TMA emissions are relatively weak. The weaker emissions combine with higher diffusion rates at higher altitudes to make TMA unsuiatble for measurements above 170 or 180 km altitude. Barium/strontium mixtures and lithium are bright enough when sunlit to be tracked for tens of minutes. The dominant emissions of those chemicals are sufficiently bright to be tracked long enough to obtain accurate neutral drifts.

All of the releases discussed below were analyzed using the same general procedures. The chemical releases were photographed from three spatially-separated camera sites, providing simultaneous images from three different angles. Wind profiles were obtained from each launch by combining images from pairs of commercial Nikon cameras located at different sites. The star field present in each image was matched to the Smithsonian Astronomical Observatory (SAO) database, which was then used to map the image pixels to equatorial coordinates, i.e., right ascension and declination based on the known positions of the stars. The geographic location for the camera site and the local time of each photograph defines the conversion from equatorial to horizon coordinates, i.e., azimuth and elevation. GPS devices connected to the cameras ensure that images are simultaneous. Software combines the photographs from a pair of sites to compute the intersection point for lines-of-sight to different points within the releases. Details on this software can be found in the work of Ingersoll (2008). The output from this procedure is a full three-dimensional position for each cloud point. Velocities are calculated by computing a linear fit from the position data obtained from the image sequence, with uncertainties estimated based on the variance in the time series.

An example of error estimation for the F region lithium release of the EVEX experiment is shown in Figure 4.1. The figure shows the longitude position generated as a result of triangulation for an altitude of 300 km as a function of time, along with the linear fit applied to the position data. The linear fit produces a 95% confidence interval of ±10.4 m/s, with a slope equivalent to 49.7 m/s.

There are several potential sources of error in this analysis. The first basic assumption is that the vertical winds are negligible, which is generally true in the equatorial thermosphere. This means that we assume that all points at a particular altitude during the triangulation procedure are, in fact, the same point along the trail. The second assumption involves the fitting of the final position points to a

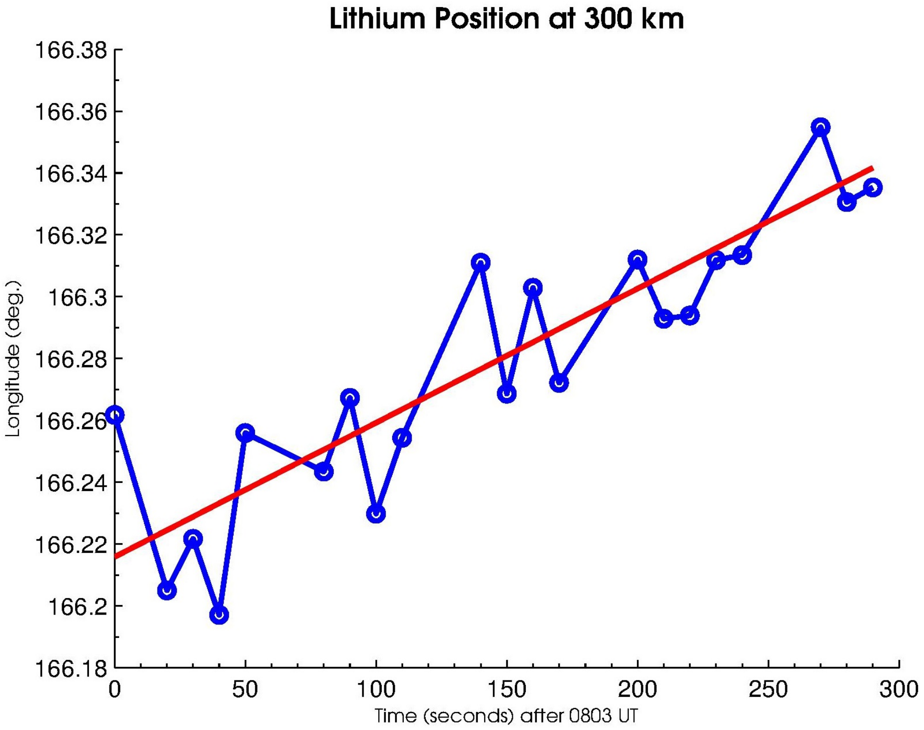

Figure 4.1: Example of position fitting and error analysis for the EVEX lithium trail. The longitude as a function of time is used to produce a linear fit. The slope of the linear fit is the velocity, with a 95% confidence interval estimated based on the goodness of fit. For this case, the velocity slope is 49.7 ±10.4 m/s.

curve, from which we can derive a velocity. Typically, the velocity is assumed to be constant over the course of the trail lifetime, meaning we can apply a linear fit to position as a function of time. However, as shown in the studies presented here, this may not be a valid near sunset, and thus some error may arise as a result of that assumption. There have been too few rocket studies to quantify the time scale at which the assumption of constant velocity begins to break down.

The second source of errors comes from the fitting itself. The trails are far enough from the cameras that even a single pixel represents a significant distance. This means that even slight errors in the triangulation process can create variance in the position that affects the fitting. In typical TMA experiments, the triangulation process is robust enough and the number of images used is great enough that the error introduced as a result of this is on the order of only a few meters per second. However, the larger F region blobs studied in the EVEX and MOSC campaigns require assumptions to be made about the Gaussian nature of the cloud diffusion, to which a fit is applied. Because the image is several thousand pixels wide, the Gaussian fit may be off from the true center by a few pixels in any direction. This would still be considered a good fit, but it nonetheless introduces some error into the position estimate.

Local seeing conditions have a large impact on the F region releases as well. In equatorial experiments, which are typically launched from coastal areas such as the Marshall Islands, fast, low-lying clouds are very common. The clouds may cover part of a narrow TMA trail for only a few seconds, resulting in one or even no unusable exposures. However, the F region releases diffuse so rapidly that they cover a large portion of the sky. When clouds pass over, covering part of the blob, this has an effect on the Gaussian fit. The large nature of the cloud means that a single, rapidly moving cloud can still obscure several consecutive images. Some data points are therefore thrown out by hand because their accuracy could not be trusted due to clouds along the line-of-sight.

4.3 The Guara Campaign

The Guara campaign was a series of rocket and radar investigations that were carried out from August to October, 1994. The studies targeted both *E* and *F* region dynamics associated with spread *F* activity (Pfaff et al., 1997). The rocket investigations of interest here were conducted as a part of the sunset electrodynamics investigation at a rocket range near Alcantara, in northern Brazil. Two rocket salvos were launched on back to back nights, Septemper 23-24, 1994, just after local sunset. Each salvo included two rockets. One rocket flew eastward, releasing a barium/strontium payload in the *F* region, followed by a TMA trail in the *E* region. The second rocket was launched nearly simultaneously with the first and flew northward, producing a TMA trail near the *E*-region base of the magnetic field line that passed through the *F* region above Alcantara. The *E*-region TMA measurements were originally published by Larsen and Odom (1997), but hazy seeing conditions prevented the *F*-region barium film from being used in manual triangulation. Modern film digitization technology and computer analysis techniques have allowed us to revisit the barium data. High-resolution image scans allow for a much better specification of the trail position and have enabled us to revisit the barium data in order to produce *F* region ion and neutral drift measurements.

A key feature of Ba/Sr chemical releases is that a large fraction of the barium cloud photoionizes rapidly. Magnetic influence causes the ionized portion to rapidly align with the magnetic field lines, elongating and drifting with the ambient ions. This occurs only when the Ba/Sr mixture is sunlit, meaning such launches at the equator are limited to local twilight, where the ground camera sites are in darkness, but the *F* region is still sunlit. The primary transition of Ba^+ produces a bright red emission that stands out from the blue-green emissions of the neutral Ba/Sr cloud. The neutral and ionized portions of the cloud quickly separated, producing drift measurements for both the neutrals and ions. This is evident in the sample image from the Sept. 23 launch, shown in Figure 4.2. The look direction of this camera site is almost directly north, meaning the magnetic field lines run overhead in the image. The separation of the Ba/Sr mixture has begun, with the ionized barium elongating along the magnetic field. Located below the Ba/Sr cloud is a typical TMA trail. Sunlight causes the top portion of the TMA trail to fluoresce blue, while the bottom portion that is located in darkness fluoresces a milky-white color.

Three sets of cameras were used for the chemical release experiments. One was located at the launch site of Alcantara, and one at Parnaiba, further east along the coast. A NASA aircraft carried a third set of cameras. Figure 4.3 shows the positions of the camera sites and the aircraft, as well as the initial positions of each release. Using the process discussed in Section 4.2, we have obtained the position of the trails as a function of time. The zonal and meridional winds obtained from the triangulation are shown in Figures 4.4 and 4.5 for the first and second nights, respectively. Uncertainties for the TMA releases are approximately ±5 m/s, and the uncertainties for the barium releases are ±10 m/s. The reason for the narrow altitude range of ion measurements is that the ion motions are constrained by the magnetic field, while the neutral cloud is free to rapidly diffuse upon release.

The vertical profile of the zonal wind exhibits a strong negative (westward) shear in the *F* region. This was quite unexpected. Much modeling work that has been done regarding the equatorial *F* region (e.g., Zalesak et al. (1982); Hysell et al. (2006) has assumed that the neutral winds have either no shear or slightly positive

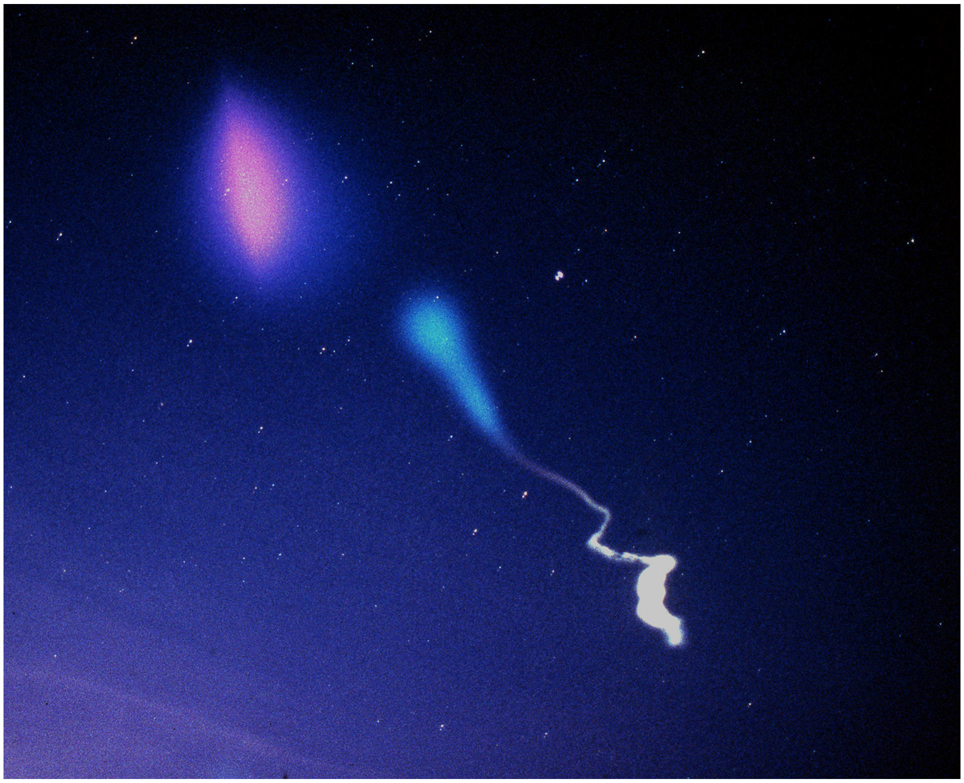

Figure 4.2: Sample image from the Guara campaign showing the partially ionized barium/strontium cloud (top) and the TMA trail (middle and lower). Figure from Kiene et al. (2015).

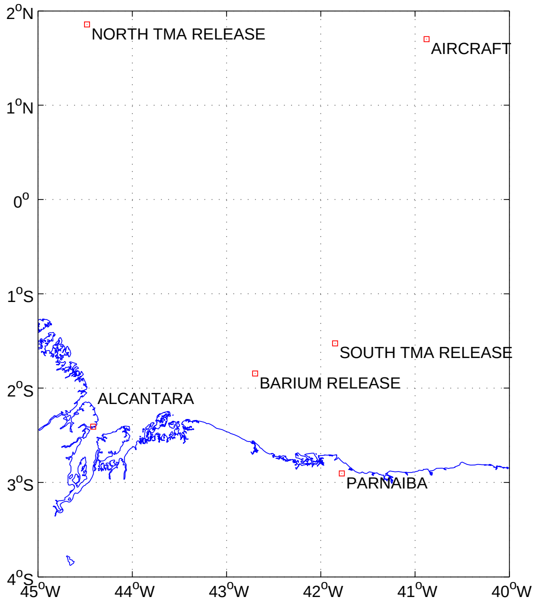

Figure 4.3: Geographic map of the Guara campaign, illustrating the initial positions of the chemical releases, as well as those of the ground-based and aircraft observation sites. Figure from Kiene et al. (2015).

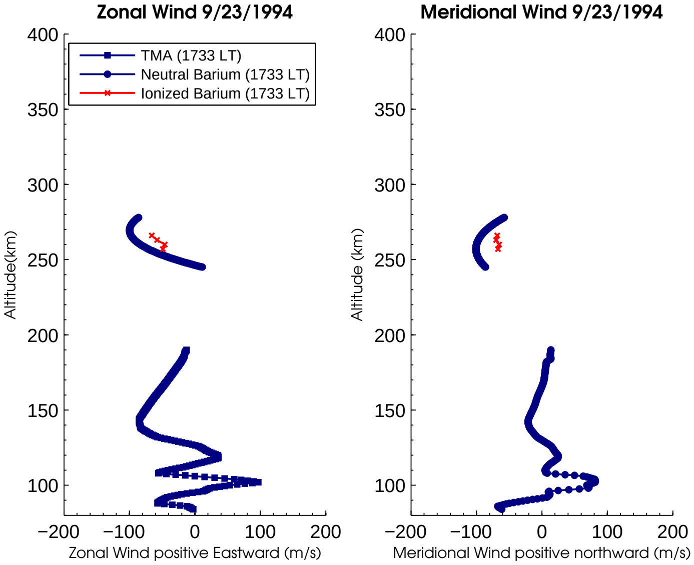

Figure 4.4: Zonal (east-west) and meridional (north-south) neutral wind and ion drift profiles measured during the Guara launch on Sept. 23, 1994. In each plot, blue lines represent the TMA and barium/strontium neutral wind measurements, while the red dots indicate the Ba^+ ion drifts. The TMA profiles in the lower altitude range were originally published by Larsen and Odom (1997). Uncertainties are ±5 m/s for the TMA trails and ±10 m/s for the barium/strontium release. Figure from Kiene et al. (2015).

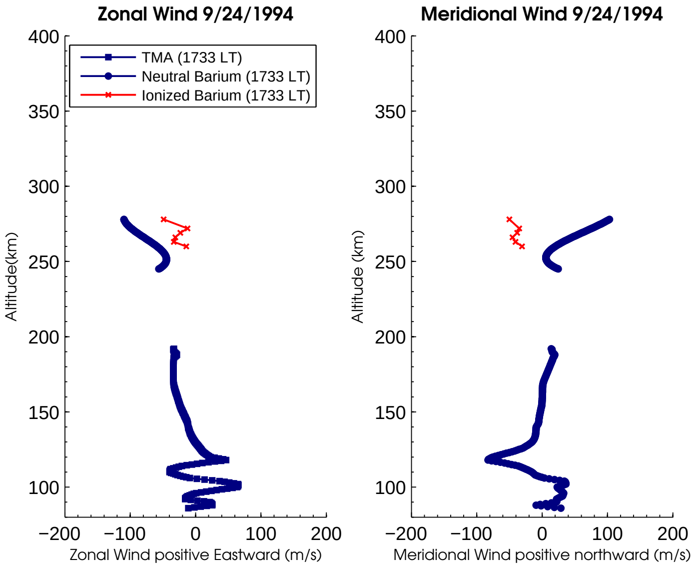

Figure 4.5: Same as Fig. 4.4, but for the second Guara launch on Sept. 24, 1994. Uncertainties in the drift measurements are ±5 m/s for the TMA trail and ± 10 m/s for the barium/strontium release. Figure from Kiene et al. (2015).

shear during twilight. Previous theoretical work has shown that this should be a valid assumption because the effective viscosity increases sharply with altitude due to the higher mean free path as the total density decreases (Hedin et al., 1991). The high viscosity inhibits the growth of vertical shears. Indeed, this has been the classical empirical model output for many years, but this has been, in part, due simply to the lack of vertically resolved data on which to rely (Drob et al., 2008). Previous ground-based experiments have shown an eastward flow in the F region near 250 km, but these were primarily single-altitude measurements, as discussed in Chapter 3. The Sept. 23 launch does show an eastward flow in the lower altitude range, but the direction of the flow transitions to westward near 250 km. The altitude range of the barium release was still sunlit at the time of the release. This is evident in Figure 4.2, which shows that the top of the lower-altitude TMA trail is still sunlit. The second experiment, conducted the follwing night, showed westward flows over the entire altitude range. No spread *F* measurements were directly conducted as a part of the rocket experiments, though (Abdu et al., 1997) conducted spread *F* measurements that showed that spread *F* did occur on both nights, though we do not have detailed information about its time of occurence or behavior.

4.4 The EVEX campaign

The Equatorial Vortex Experiment (EVEX) was carried out on May 7, 2013, with the objective of obtaining simultaneous measurements of *E* and *F* region neutral winds, electric fields, and plasma densities. The ultimate goal of the experiment was to better understand the evening pre-reversal vortex presented and discussed by Kudeki and Bhattacharyya (1999) and Kudeki et al. (2007). Two sounding rockets were launched just after sunset from the Roi-Namur rocket range in the Kwajalein Atoll of the Marshall Islands. The launch site was located at 4° N geomagnetic latitude and 9° geographic latitude. Two TMA trails were released along the up-leg and down-leg portions of the low-apogee rocket trajectory. The high-apogee rocket released two lithium trails along the down-leg. The lithium trails were ignited sequentially between 350 and 250 km altitude. Figure 4.6 shows a composite image of the lithium and TMA releases from the Roi-Namur camera site. Similar to the Guara image above, the top of the TMA trail is still sunlit, fluorescing blue, while the bottom portion is no longer sunlit and fluoresces white.

Camera sites for this experiment were located at three ground-based locations spread throughout the Marshall Islands. Figure 4.7 shows a map of the observation sites, the initial position of the TMA release, and the position of the lithium trail both initially and approximately 20 minutes after release. Both the lithium and TMA releases occurred at 1945 local time (UT+12 hr). Sunset at the initial point of release

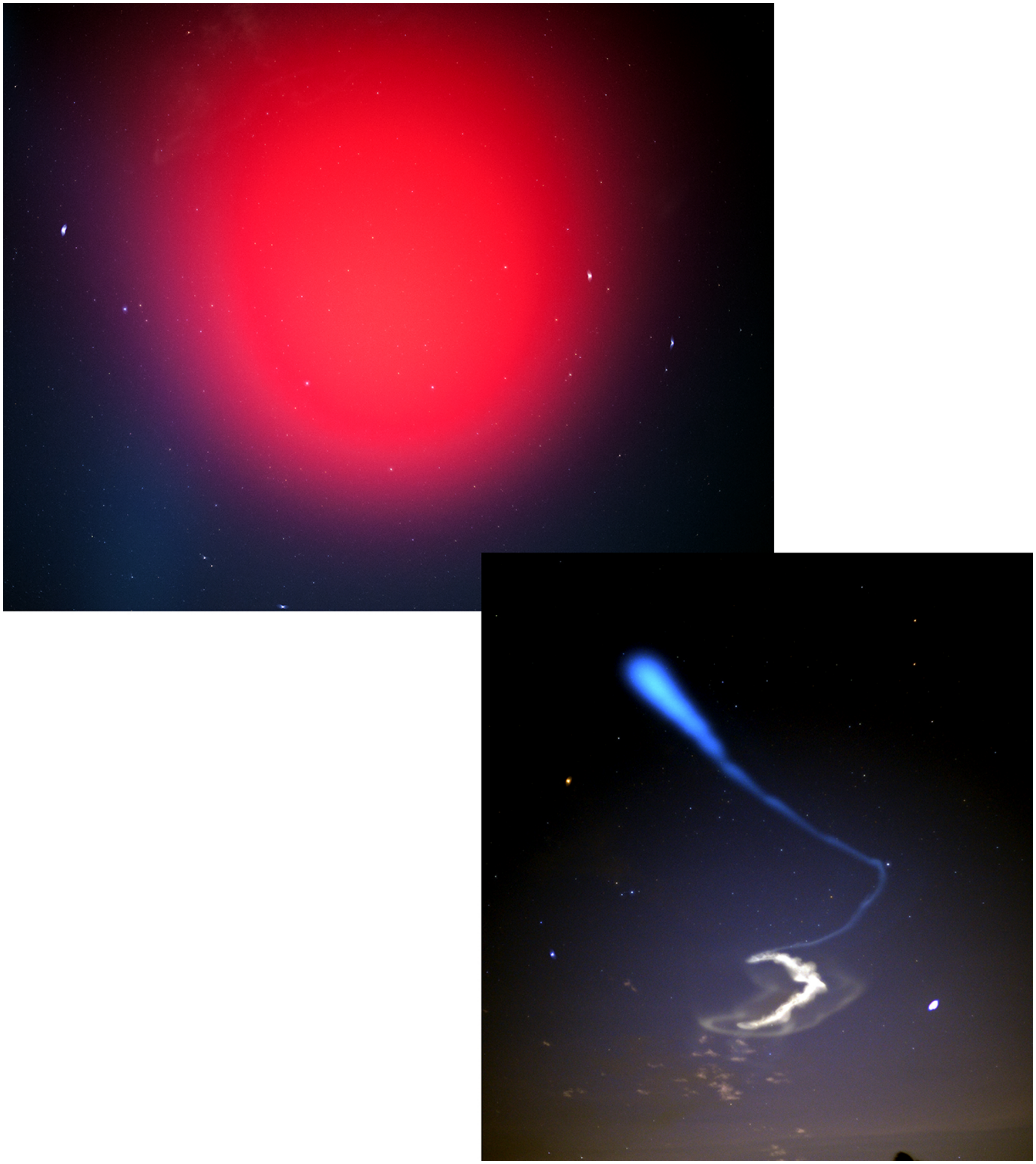

Figure 4.6: Composite image from the EVEX launch. The high-altitude lithium cloud fluoresces bright red and has diffused rapidly into a large ball, while the lower-altitude TMA trail fluoresces blue where lit by the sun and milky-white where it is in darkness. Figure from Kiene et al. (2015).

occurred at 1849 local time, and the releases occurred at a solar depression angle of 8°.

For the purposes of neutral wind experiments, lithium has the significant advantage over barium, in that it remains neutral for a long period after release. The dominant emission of lithium is at 670.1 nm, which allowed for observations using narrow 2-nm filters centered on the primary transition. White-light cameras were also used in the observations. The rapid diffusion of the lithium clouds (see Figure 4.6) made identifying the center of the trail difficult. The initial emissions were also brighter than expected, which caused the saturation of many of the images early in the observation period. In order to track the center of the trail, which is also the point of maximum lithium concentration, we followed the method of Watanabe et al. (2013), who employed a Gaussian fit along a slice through the lithium trail. Because the diffusion of the neutral gas should be horizontally symmetric, the bulk neutral drift can be found by tracking the center point of the trail. We applied a similar Gaussian fit to the non-saturated images in order to fit the intensity of the red channel along a single-pixel slice through each image.

The orientation of the Roi-Namur camera site made it ideal for this type of analysis. Its look direction was almost directly west, along the rocket trajectory. The X- and Y-dimesnions of the image, therefore, correspond to horizontal (north-south) and vertical, respectively. This means that a cross-section at constant altitude can be approximated by taking a horizontal slice across the image. The Gaussian fit will thus produce a maximum lithium density that can be tracked with time. Figure 4.8 shows a pair of examples of slices through a concecutive lithium images. The cameras used in the experiment had an exposure cadence, meaning that consecutive images had different exposure times, resulting in one image being saturated while the next was not. For the bottom slice, a Gaussian fit will obviously produce a good estimate for

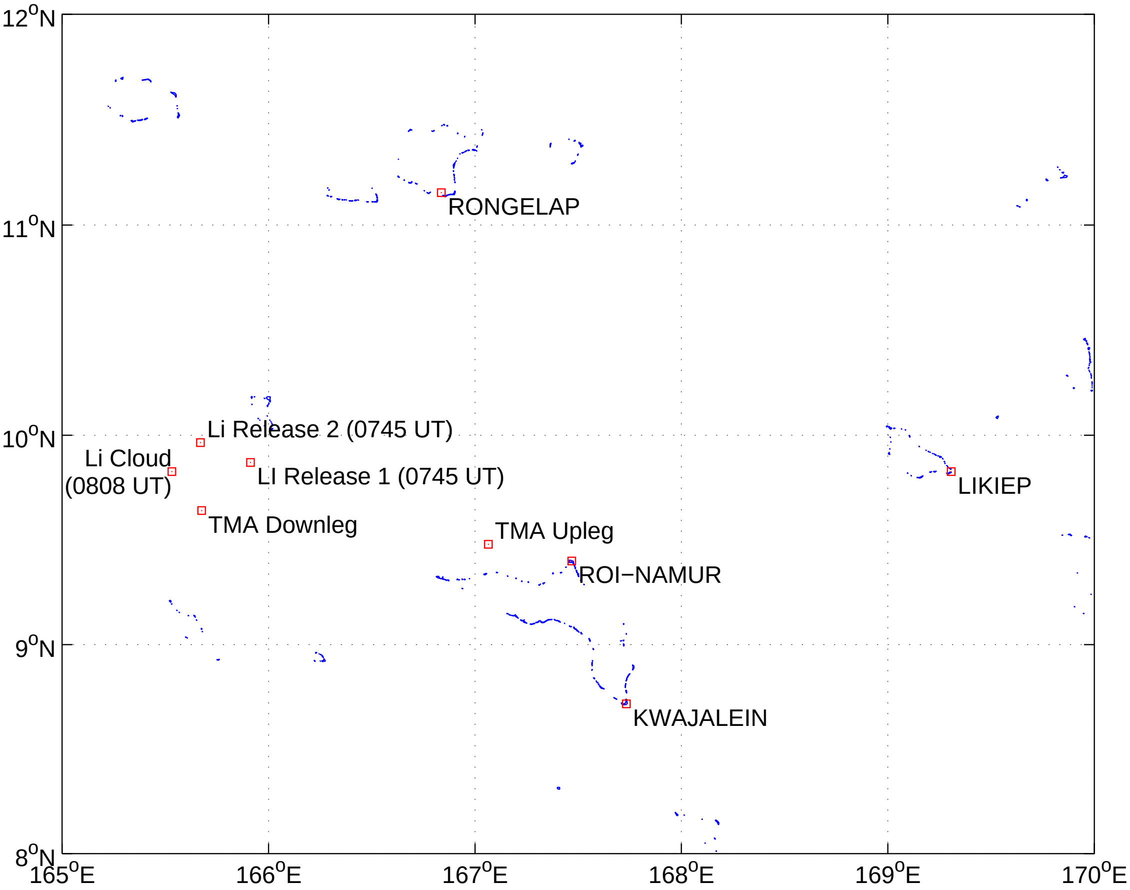

Figure 4.7: Geographic map of the EVEX campaign, showing the release positions of the lithium and TMA trails, along withlocations of the ground observation sites. Also shown is the position of the lithium cloud during the second observation window (0808 UT). Figure from Kiene et al. (2015).

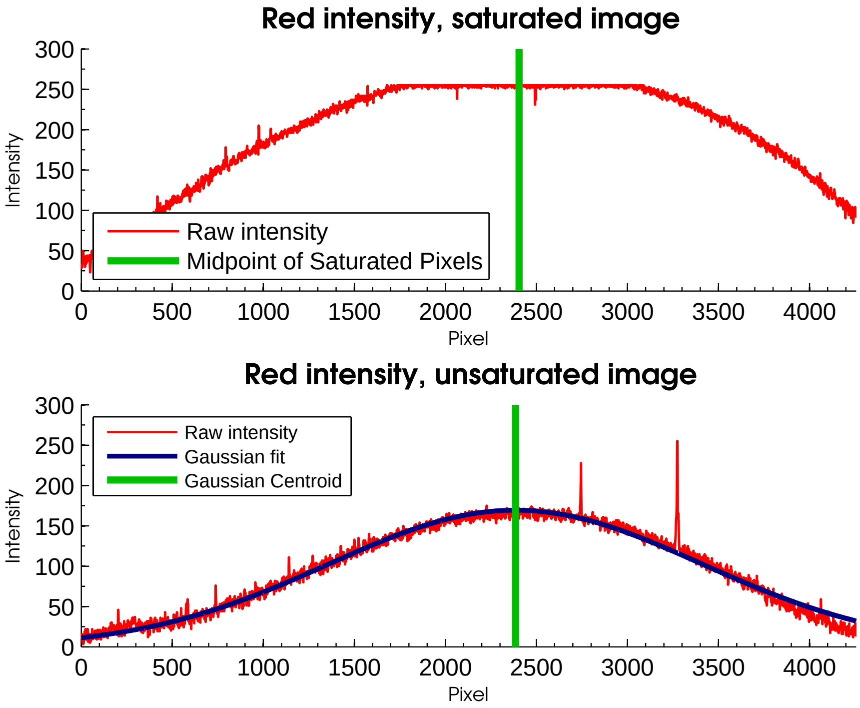

Figure 4.8: From two consecutive images, one which is saturated and one which is not, horizontal cross-sections are taken through the lithium cloud. Different methods are used to determine the point of maximum lithium concentration, represented by the green line in each plot. Figure from Kiene et al. (2015).

the maximum. The top slice is an example of one of the saturated images that cannot be properly approximated by a Gaussian. Instead, they are saturated enough that the midpoint of all saturated pixels is a good approximation of the maximum. The green line shows the location of the maxium obtained by the respective techniques.

The Likiep camera site was not used for this analysis. Its look direction was very similar to that of Roi-Namur, nearly directly west. The lenses used for the photography at Likiep also had a smaller field of view than the other cameras. The unexpected rapid diffusion of the lithium releases expanded beyond the camera's field of view. We therefore used the camera sites located at Roi-Namur and at Rongelap for the triangulation. Being limited to two camera sites had some drawbacks, as scattered low-level clouds did sometimes obscure the trail during the observation window. At Roi-Namur, the initial release period was mostly clear from 0745 to 0755 UT, with only small (< 1 min) gaps in useable images. However, from 0755 to 0805 UT, thicker clouds passed through, obscuring the trail at both sites. This left two windows of useable images with a separation of about 20 minutes.

The above method allowed for good estimates of the trail center that were sufficient to produce vertical profiles with an altitude resolution of 5 km in the *F* region. Figre 4.9 shows the zonal and meridional neutral winds derived from both observation windows. The lower altitude TMA profiles have uncertainties of ±5 m/s, while the uncertainty in the lithium profiles is ±15 m/s.

The *F* region zonal winds measured approximately 40 minutes after local sunset during EVEX show strong westward vertical shear. The winds in the lower altitude range are eastward, transitioning to westward around 270 km altitude. These wind profiles are similar to those measured during the Guara campaign. The winds are eastward and of moderate magnitude, which is similar to average Fabry-Perot interferometer measurements taken near the equator (Emmert et al., 2006). The EVEX results also show that the zonal winds are rapidly changing. In a period of only twenty minutes, the zonal wind has shifted toward the east, with the shear all but vanishing. This is consistent with theoretical and empirical expectations.

4.4.1 Additional data taken during EVEX

In addition to the chemical releases, EVEX measurements included rocket-mounted probes as well as ground-based radar measurements. The C/NOFS satellite

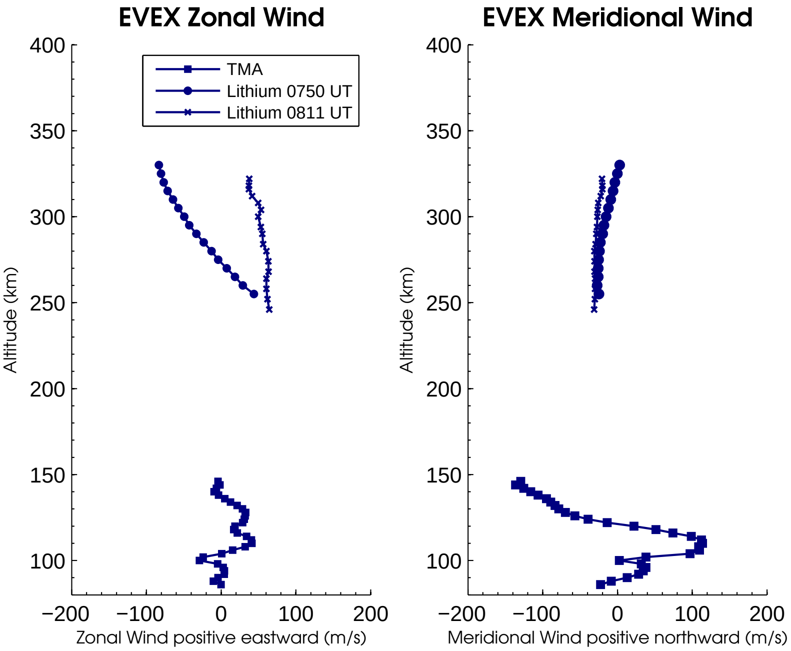

Figure 4.9: Zonal (east-west) and meridional (north-south) neutral wind profiles obtained from the EVEX experiment. The lower region, between 80 and 150 km, represents the winds obtained from the TMA release. The upper region winds are those derived from the lithium release in the *F* region. About twenty minutes separates the two upper profiles (0747 UT to 0808 UT), where scattered clouds created two distinct observation windows. Uncertainties for the two releases are ±5 m/s for the TMA release and ±15 m/s for the lithium releases. Figure from Kiene et al. (2015)

also passed overhead on the night of the launch, providing additional data. These instruments are capable of measuring ion drifts, electric fields (and thus ion $\mathbf{E} \times \mathbf{B}$ drifts indirectly), and plasma density. These other measurements will allow for the specification of the background ionospheric parameters. This would allow for a data-driven modeling study, such as those conducted by Hysell et al. (2014) and Hysell et al. (2015), using the vertically resolved EVEX winds as input. Such a study would be the first to fully specify the neutral wind profile. Unfortunately, the full radar data set is not yet available for study. When it becomes available, the modeling work shown in Chapter 5 of this dissertation will be expanded to include the ionospheric measurements in place of empirical model data.

Data from the C/NOFS satellite on its pass through the Kwajalein sector near launch time is shown in Figure 4.10. The satellite produced 10-second averaged measurements of the zonal and meridional electric fields, which can be used to calculate the ion $\mathbf{E}\times\mathbf{B}$ drifts. The ion drifts show both a prereversal enhancement of the vertical component as well as the vortical motions expected based on the work of Kudeki and Bhattacharyya (1999). The altitude of the satellite is shown in the bottom plot (red line), along with the geographic position of the magnetic equator (blue line) and the satellite itself (black line). Near Kwajalein, the satellite reached its perigee of approximately 400 km.

The rocket probes themselves also captured electric field measurements. These are shown in Figure 4.11. These are vertical profiles, which show the altitude of reversal in the zonal drifts near 275 km. In this figure, the rocket flew from right to left, a westward trajectory. It is particularly noteworthy that the upleg measurements show very little in the way of vertical gradients, with drifts remaining eastward throughout the entire altitude profile, while the downleg measurements show a similar sheared structure to that found by, e.g., Kudeki et al. (1981).

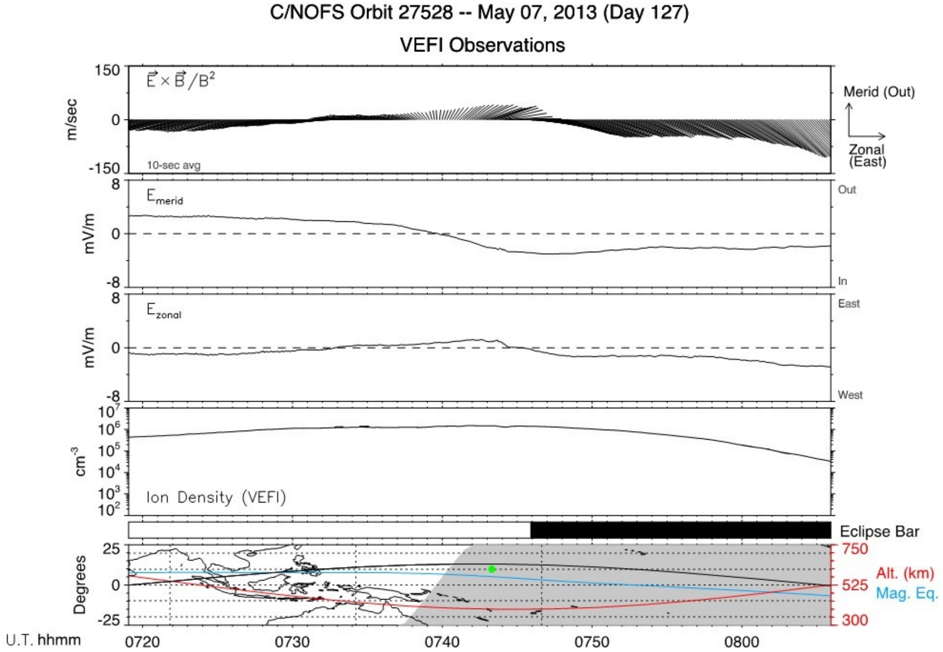

Figure 4.10: Measurements from a C/NOFS satellite pass near the launch time of the EVEX experiment. The top panel represents the vector $\mathbf{E} \times \mathbf{B}$ drift, while the bottom panel depicts the satellite orbit. The black line is the geographic location of the satellite, while the red line represents its altitude, and the blue line is the location of the magnetic equator.

In addition to the rocket and satellite measurements, radar measurements were conducted with a portable UHF radar from the University of Illinois. A snapshot of data from this radar taken approximately 1 hour after the EVEX launch is shown in Figure 4.12. The top panel is a plot of electron density that shows a spread F plume that has developed. The bottom panel shows plasma drifts derived from UHF long-pulse data based on the Doppler shift. Blueshifting represents drift toward the radar location, and redshifting represents drift away from the radar location. The drifts measured here therefore imply an eastward plasma motion throughout the observation area one hour after launch.

If the plasma drifts follow a typical equatorial nightly pattern, there will be a shear node in the plasma drift profile, as seen in Figure 4.11, with eastward drifts above the node and westward drifts below. This shear node will propagate vertically, but the westward drifts below the shear node will gradually reverse toward an

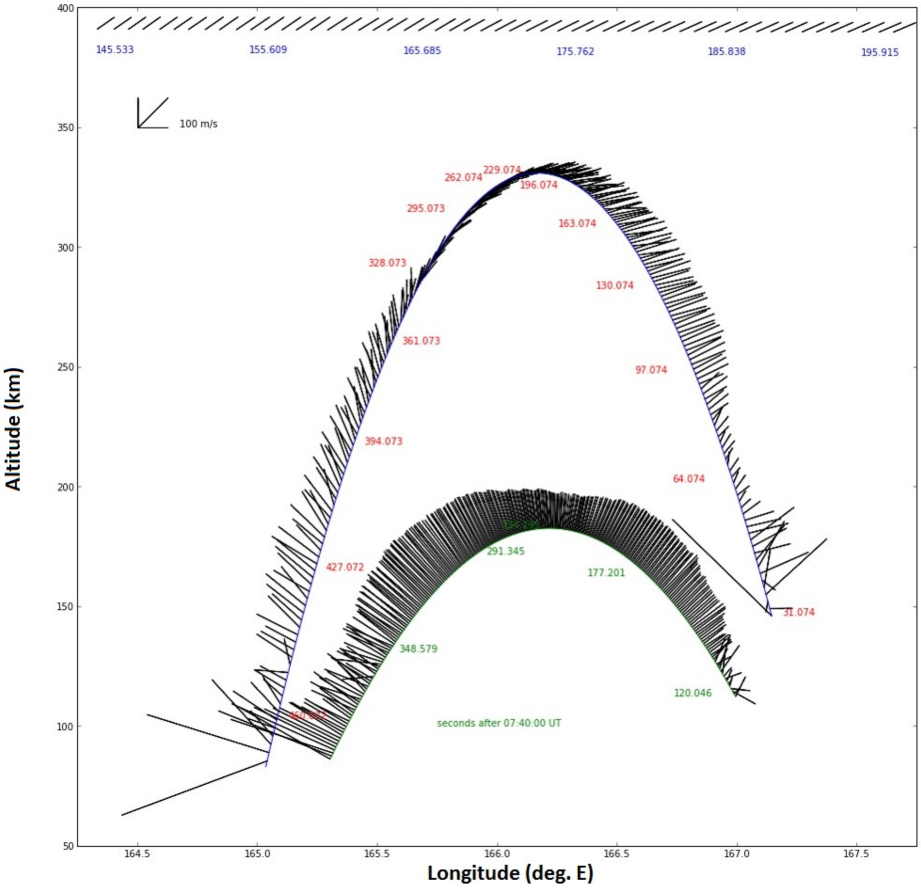

Figure 4.11: Plasma drift measurements from the Langmuir probes aboard the two EVEX rockets. The rockets flew from west to east (right to left). There was very little vertical structure in the plasma drifts on the upleg, but significant shears appeared on the downleg, 2 degrees to the west. Data courtesy of Dr. Rob Pfaff.

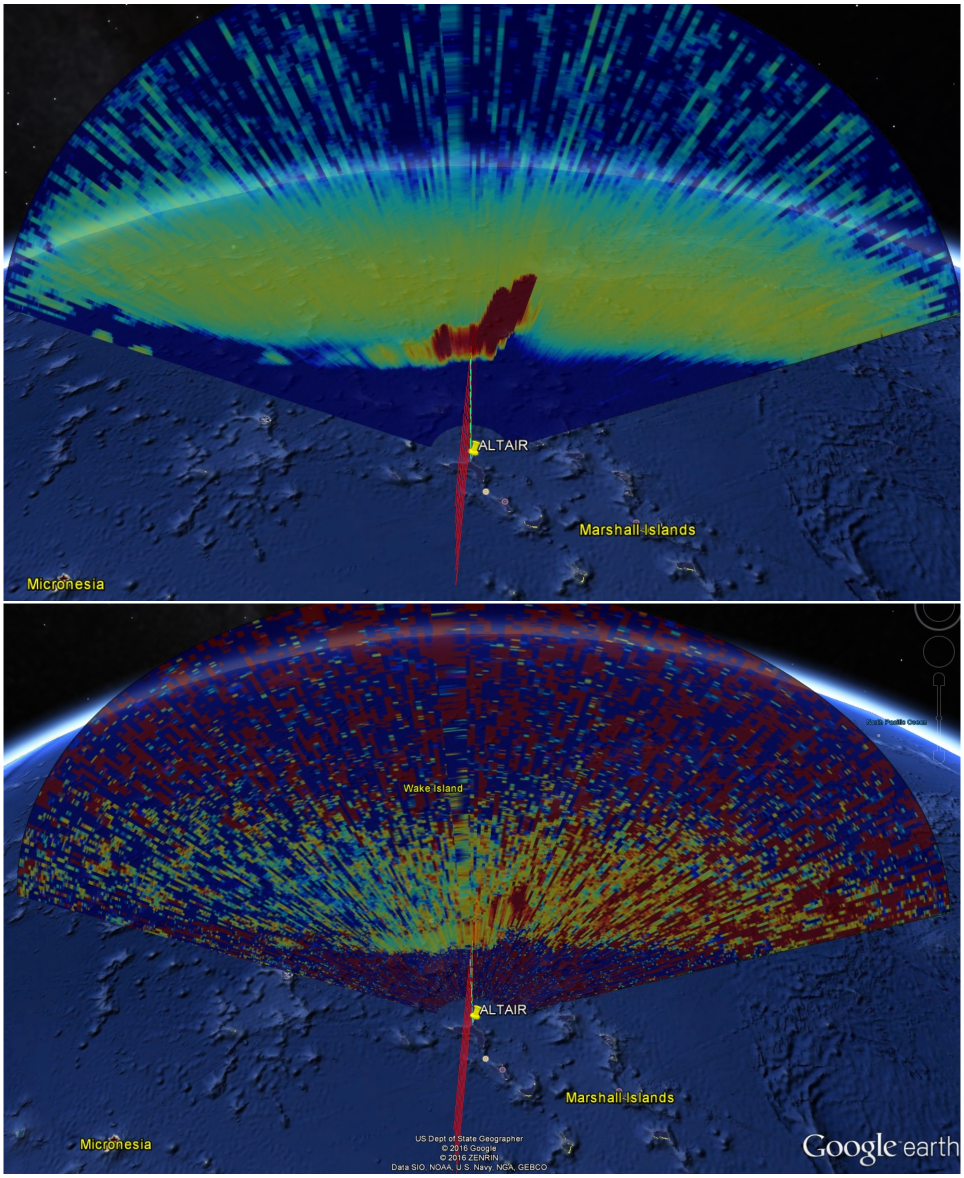

Figure 4.12: Plasma density from the University of Illinois portable coherent scatter radar (top) and plasma drift from ALTAIR (bottom) measurements taken approximately 1 hour after the EVEX launch. In the top plot, the red areas represent high signal-to-noise ratio, indicating there is significant 3-m structure present. In the plasma drift plot, blueshifts represent drift toward the radar, and redshifts indicated drift away from the radar, implying an eastward drift throughout the observation area. Data courtesy of Dr. Erhan Kudeki, University of Illinois at Urbana-Champaign.

eastward drift at all altitudes. This is what we see in Figure 4.12. An hour after the EVEX launch, the plasma drift has lost the sheared structure and adopted a uniformly eastward flow, consistent with the vortical flow pattern seen in Figure 2.10.

The currently available radar data are unfortunately limited. In Figure 4.12, we see a single small spread *F* plume that has developed near the bottomside, with very little in the way of other structures, particularly in the bottomside region. The neutral wind measurements from EVEX indicate that the wind is still westward in the *F* region early in the night, eventually reversing to a more uniform eastward profile. The timing of this reversal is quite important when considering collisional shear instabilities, previously discussed in Section 2.5.4. Shear instability growth is controlled by the difference between the zonal wind and the plasma drift. If zonal winds and plasma drifts are both eastward and of similar magnitudes, shear instability will fail to contribute to the overall growth of spread *F* near sunset, leading to a reduced bottomside instability layer and, presumably, to smaller, less turbulent plumes. The EVEX results, therefore, present an interesting question that compels further study: If sheared, westward zonal winds are a common feature of the sunset *F* region, can we find a relationship between the timing of the neutral wind reversal and subsequent spread *F* morphology? Further experiments are needed to answer this question fully, since there simply are not enough coincident neutral wind profile measurements and spread *F* observations to draw any sort of conclusion. Nonetheless, in Chapter 5 we will attempt to examine the effects of sheared neutral flows on plume development by means of a numerical model.

4.4.2 Summary of EVEX results

The EVEX launches are the most complete set of measurements taken in the equatorial *F* region near sunset, combining radar, rocket probe measurements, and chemical release analysis to produce a data set of simultaneous neutral and plasma behavior. The zonal neutral wind data derived from the EVEX releases are unexpected based on classical assumptions about the vertical structure of the wind profile near sunset, but they are corroborated by earlier experiments during the Guara campaign. Plasma shears like those first measured by Kudeki et al. (1981) were found to be present on the western downleg of the rocket trajectory. Radar measurements in the period after the launches reveal a small spread *F* plume did develop an hour after sunset, indicating that the westward winds and gradients in the neutral wind did not completely inhibit plume development. Still, the EVEX results have urged the question: How much can sheared neutral winds near sunset affect spread *F* development? This question will be explored in Chapter 5.

4.5 The MOSC campaign

The MOSC campaign shared the Roi-Namur rocket range with the EVEX campaign during April and May of 2013. Two rockets were launched as a part of the MOSC campaign, one on May 1 and one on May 9. In each, the rocket released a single samarium cloud near 190 km altitude. The chemical releases occurred 40 minutes after sunset on May 1 and 25 minutes after sunset on May 9. A sample image from the first release is shown in Figure 4.13. The same camera sites were used as for the EVEX launch, and a similar analysis procedure was used to fit the diffuse samarium cloud. The samarium separated into two clouds, one blue and one red, which were fit with separate Gaussians. This separation is illustrated in Figure 4.14.

Figure 4.13: Sample image from the May 9th MOSC release showing the two-color samarium cloud.

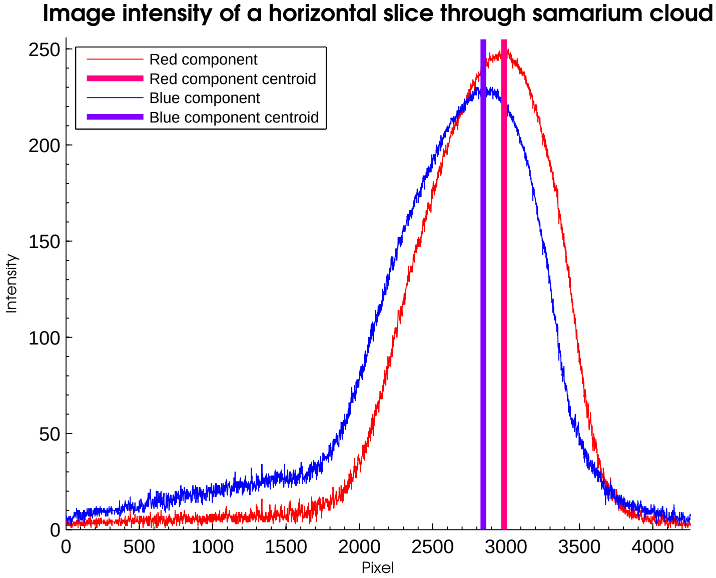

Figure 4.14: Horizontal cross section through the samarium cloud from an image at the Roi-Namur camera site. The separation between the blue and red maxima is clear. Vertical lines are placed at the point of maximum concentration of the Sm and SmO, determined by a Gaussian fit.

4.5.1 Samarium Chemistry

As illustrated in Figure 4.13, the samarium release separated into two components, corresponding to a neutral cloud and an ionized cloud. Holmes et al. (2016) studied the chemical reactions between the samarium metal and the ambient atomic oxygen in the atmosphere. The visible ionized cloud is produced by a combination of SmO+ and Sm+, with the latter dominating approximately 100 seconds after release. The neutral cloud becomes dominated by molecular SmO emissions after 100 seconds. Spectrograph measurements shown by Caton et al. (2016) indicate that the cloud is initially dominated by transitions in the blue, with red transitions near 650 nm developing after approximately 1 minute. Samarium reacts rapidly with the ambient oxygen upon release, eventually forming distinct populations of elemental Sm and molecular SmO. These, along with their ionized forms, produce emissions in both the red and blue ends of the visible spectrum, which can be tracked separately, with the red comprised primarily of SmO and the blue comprised primarily of Sm (Holmes et al., 2016). It is not known precisely which spectral lines come from the molecular SmO, but the elemental Sm and Sm^+ spectra are well known to have transitions only in the blue region of the visible spectrum. This, combined with the development of the red emission some time after the release, suggests that the red emission must be primarily due to molecular SmO that is formed through reactions with the ambient oxygen.

As shown in Figure 4.14, the samarium release separated into two components, a red component and a blue component. Holmes et al. (2016) analyzed the chemical reactions between the samarium metal and the ambient oxygen in the atmosphere. The visible red cloud is produced by a combination of emissions from SmO and SmO^+, with SmO dominating due to higher concentration. The precise contribution of SmO^+ is unknown because no spectra of the gas phase exist in the literature, but it is assumed to be small. The blue cloud is produced by Sm and Sm^+ emissions, with neutral Sm comprising >90% of the emissions. The population of the aggregate samarium cloud is primarily neutral, with SmO being more populous than Sm.

This analysis indicates that both the red and blue clouds are populated by a combination of ions and neutrals. This is validated qualitatively by observations of a samarium cloud released as a part of the COPE 2 experiment in Greenland (Larsen et al., 1989). The development of the samarium cloud exhibits behavior similar to both neutral and ionized clouds released near the same time during the COPE 2 experiment. A few snapshots illustrating the behavior of the samarium cloud in Greenland are shown in Figure 4.15. At polar latitudes, the large neutral and ion drifts are sufficient to cause significant visible changes in the trail that are not apparent in the MOSC images. The red SmO emission remains readily visible in the Greenland images, while the blue diffuses and melds with the blue background; however, it is clear that the red cloud both aligns with the magnetic field (see the purple striated barium clouds) and elongates perpendicular to the field, presumably drifting with the neutral wind.

4.5.2 MOSC neutral wind results for Sm and SmO

The separation of the samarium release into two distinct clouds meant that each could be tracked separately. We applied filters to the camera images that separated the Sm and SmO emissions, thus producing two drift profiles for each MOSC launch. The drifts are shown in Figure 4.16 for the MOSC-1 launch on May 1 and in Figure 4.17 for the MOSC-2 launch on May 9.

The color of the background twilight sky slightly contaminated the blue end

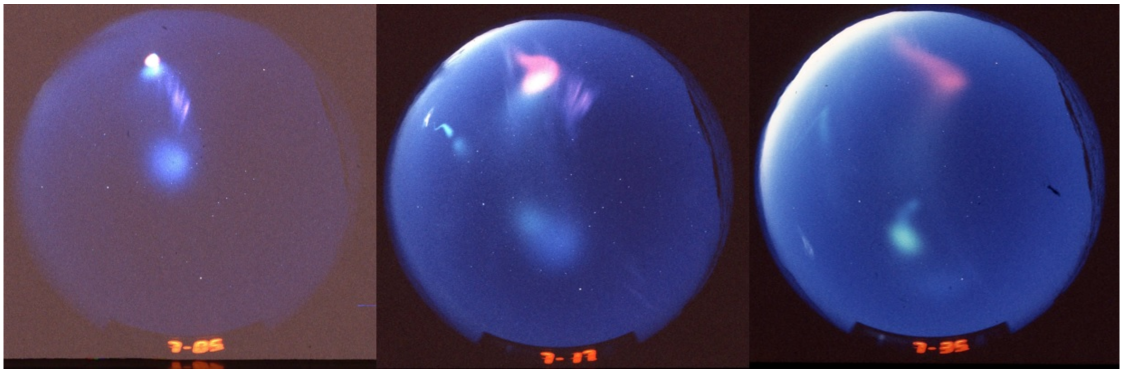

Figure 4.15: Three successive all-sky images from a samarium release over Greenland. The pink samarium cloud seems to evolve in two different ways, aligning with the magnetic field and drifting perpendicular to it, implying that it is responding both to ion and neutral forcing. Also visible are striated purple Ba^+ trails and a TMA trail on the far left.

of the spectrum, meaning that cross-sections of the red SmO cloud produced better Gaussian fits than those of the blue Sm cloud. This is evident in Figure 4.14, with the blue intensity being broader and noisier than the red. The uncertainties are ±5 m/s and ±10 m/s for the red and blue drifts, respectively. Because low-lying clouds passed over the camera sites later in the observation window, the drift measurements were done using images from between 5 and 10 minutes after the release. The positions and direction of motionresults are consistent with the qualitative results of (Caton et al., 2016) and quantitative measurements of (Pedersen et al., 2016).

4.6 Discussion of Neutral Wind Measurements

4.6.1 Implications of the *F* region measurements

The neutral wind measurements discussed in this chapter represent the total data set that is currently available for sounding rocket equatorial *F* region winds The three nights of available *F* region data show consistent vertical, westward shear

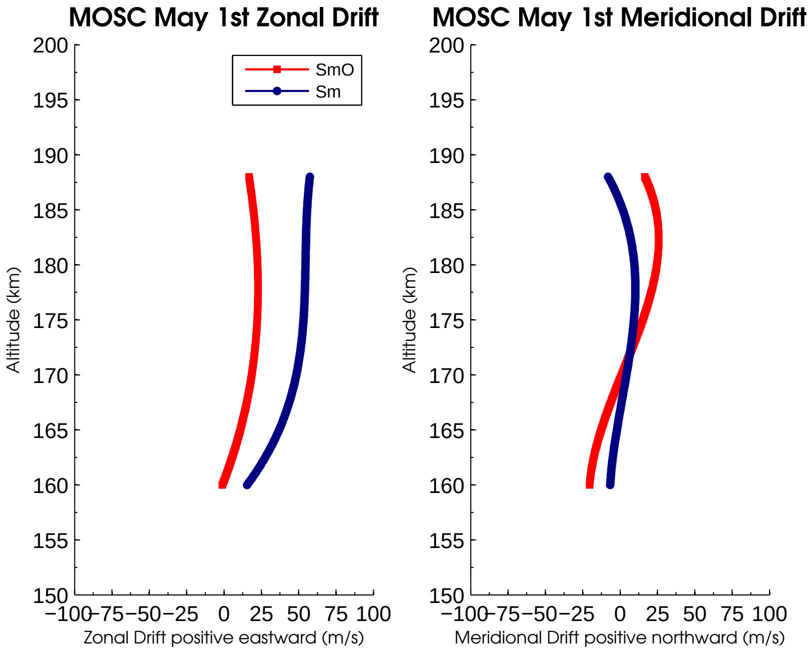

Figure 4.16: Zonal (east-west) and meridional (north-south) drift profiles measured from the MOSC launch on May 1, 2013. Red lines indicate the molecular SmO cloud, while blue lines indicate the elemental Sm cloud. A smoothing fit has been applied to the vertical profile. Uncertainty estimates are ±5 m/s for the red SmO cloud and ±10 m/s for the blue Sm cloud.

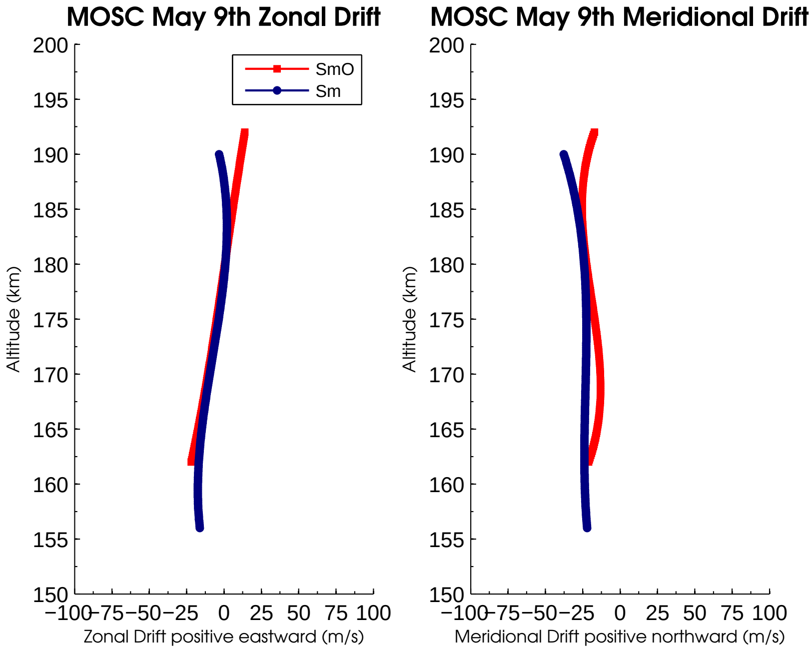

Figure 4.17: Same as the previous figure, except for the second MOSC launch on May 9, 2013. A smoothing fit has been applied to the vertical profile. Uncertainty estimates are ±5 m/s for the red SmO cloud and ±10 m/s for the blue Sm cloud.

in the zonal wind, implying that the reversal from westward flow during the day to eastward flow near sunset occurs gradually with altitude. Higher altitudes retain westward flows longer than lower altitudes. This is consistent with the motion of the solar terminator. Typically, we think of the terminator as simply propagating westward across the Earth's surface, representing the boundary between day and night. However, the boundary also propagates vertically, as the Earth's rotation begins to shield lower parts of the atmosphere first. The altitude of the terminator can be described by simple geometric considerations (Shah, 1970). A plot of the altitude of the terminator versus time, along with its rate of change in km/min, is shown in Figure 4.18.

Local sunset on the night of the EVEX launch occurred at 1909 LT, meaning the initial release occurred 35 min after sunset, when the shadow height was located near 100 km. The shadow height crossed 250 km at approximately 2011 LT, and it crossed 300 km at 2018 LT. During the experiment, the altitude of the terminator was varying at approximately 7 km/min, with trails remaining observable for up to 40 min. Thus, the shadow height rose from 100 km to nearly 300 km during the entire observing window. This may result in rapidly changing thermal conditions that create the observed gradients as the F region begins to adjust to the decreasing solar input. The Guara measurements took place during similar times, with shadow height varying from 120 km to 250 km during the observation window.

The MOSC releases do show a shift between the two releases, with the MOSC-2 release occurring 15 minutes earlier in local time. The MOSC-2 release showed westward winds of $\sim$25 m/s in the lower altitude region, trending toward zero with increasing altitude. The MOSC-1 release showed winds ranging between zero and 15 m/s eastward. It is difficult to simply tie this difference to the local time difference between the two launches, since this difference could also be a result of the strong

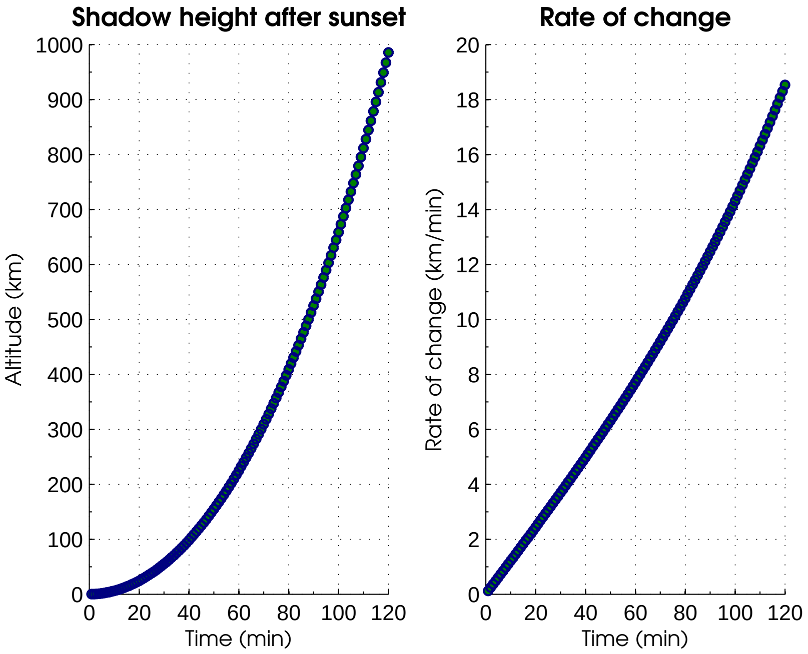

Figure 4.18: Solar shadow height as a function of time, in minutes after local sunset at the equator. The chemical releases discussed in the above sections occurred approximately 40 minutes after local sunset, persisting for up to 40 minutes. Figure from Kiene et al. (2015).

geomagnetic activity on the night of MOSC-1.

Jicamarca radar measurements have shown that the evening reversal time of equatorial *F* region zonal plasma drifts from westward to eastward is highly variable (Fejer et al., 1991). Vertical shear is also observed in the zonal plasma drift (Fejer et al., 1985). On days exhibiting strong prereversal enhancements of vertical drifts that lead to spread *F* activity, the plasma drift often takes the form of a well-defined postsunset vortex (Kudeki and Bhattacharyya, 1999). The neutral wind structure that accompanies these plasma drifts is largely unknown to this point because the plasma drifts and neutral winds are expected to equalize only after the *F* region dynamo is established a few hours after local sunset. The EVEX observations indicate that the neutrals may be responding quickly to the rising of the shadow height during sunset, reversing over a period of 20 min. or less. This is a new result, previously unexpected by the Horizontal Wind Model (HWM14), which shows that the transition from westward to eastward winds occurrs at approximately the same time for all altitudes above 200 km (Drob et al., 2015).

4.6.2 Comparison of the full measurement profiles with model winds

Though the neutral wind is a critical driver of *F* region dynamics, the lack of vertically-resolved data has led to the assumption of vertically unstructured winds above 200 km. When constructing a model of, for example, spread *F* instabilities, the neutral wind inputs are usually taken from empirical models based on satellite accelerometer and ground-based optical measurements. The Horizontal Wind Model (HWM) is the most commonly used model for this purpose. The latest version is HWM14 (Drob et al., 2015). For quite some time, HWM and models like it failed to produce the strong *E* region winds and shears seen in the results above, but recent updates have done a much better job of reproducing the *E* region winds based on sounding rocket chemical tracer data.

The primary limitation of HWM and empirical models like it is that they are based on fitting of many compiled measurements, all of which come from different instruments, places, and times. Due to their aggregate nature, empirical models tend to do a good job of predicting climatology, but they do a very poor job of predicting behavior of the atmosphere on a single specific night, simply because this is not what they are designed to do. HWM is widely used to generate neutral wind input for ionospheric models, but when considering a specific few measurements, HWM makes for a poor comparison.

Until now, there have been very few studies that provide comparisons for the region above 170 km. The majority of sounding rocket experiments conducted in the past few decades have focused on deploying TMA trails, which are limited to measuring winds below 170 km (Larsen, 2002). Very few measurements above that limit have been conducted using chemical release techniques. Together, the EVEX/MOSC and Guara experiments provided a rare opportunity to directly sample neutral winds above 170 km.

While no other chemical tracer measurements exist in the bottomside *F* region, there have been previous studies in the altitude range of the MOSC releases that validate our results. Bhasvar et al. (1965) measured the winds in the region from 180 to 200 km, above that of typical TMA tracer limits, from Thumba, India. They measured an increase in the zonal wind from 0 to 50 m/s eastward between 186 and 190 km. Valenzuela et al. (1980) also observed a shift from 180 m/s westward to 40 m/s eastward winds between 176 and 207 km from Thumba.

The EVEX results discussed by here indicate that the neutrals may respond

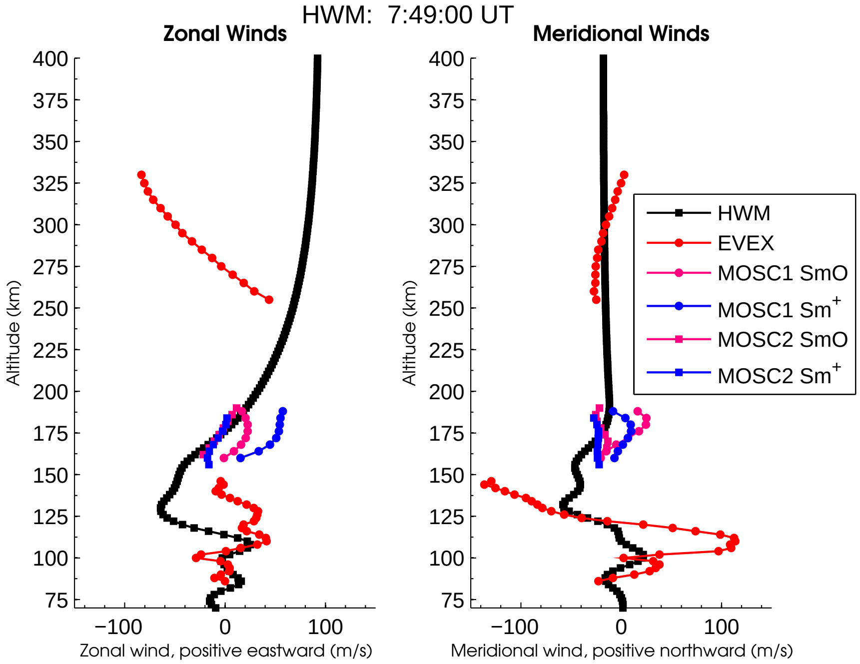

Figure 4.19: Horizontal Wind Model (HWM14) output, in black, compared with measurements from the EVEX and MOSC campaigns. The model does a decent job reproducing the structure of the wind profiles in the E and lower F regions, but it fails to replicate the large F region shear that was observed during the early period of the EVEX experiment.

very rapidly to the rising of the shadow height during the sunset period, reversing direction over a period of 20 min. or less. Caton et al. (2016) qualitatively observed a directional shift in the motion of the MOSC clouds on both nights. The MOSC-1 cloud initially drifted eastward, but rapidly turned toward the west, while the MOSC-2 cloud began drifting southeast and slowly turned westward. These observations show that the winds and plasma drifts in the region between 160 and 190 km are also rapidly changing near sunset. The difference in the magnitude of the shifts between the two launches may be due in part to the geomagnetic activity on the night of the MOSC-1 launch.

As discussed in above, the EVEX F region lithium wind measurement was significantly more sheared than was expected. Commonly used models, such as HWM14, predict smooth, eastward winds above approximately 200 km. The F region measurements from EVEX showed a strong westward shear with increasing altitude, varying significantly from HWM predictions. Figure 4.19 shows both the EVEX and MOSC winds and ion drifts, along with the HWM14 neutral wind output from the night of the EVEX launch. The MOSC launches occurred several days before and after EVEX, but the HWM14 output is very similar for all days between May 1 and May 9. It is readily apparent that there is fairly good agreement between the MOSC neutral data and the HWM output near sunset. The profiles differ slightly between the two MOSC releases. This could be due to simple day-to-day wind variability, such as that shown by Larsen (2002) at slightly lower altitudes. However, there was also significant geomagnetic activity ($k_p = 5$) during the MOSC-1 launch. The MOSC-1 Sm drifts (blue), as a result, are significantly larger than those observed during MOSC-2. The stronger plasma drifts present during MOSC-1, due to the magnetic activity, may have affected the neutral motion via drag forcing. The exact chemistry is still unclear, but the early work suggests that the Sm cloud may be more densely ionized than the SmO cloud, which would lead to it being more susceptible to geomagnetic influences, explaining why the Sm cloud showed more deviation from the drift of the SmO cloud in that case. The samarium cloud launched by Larsen et al. (1989) was released in the auroral region where plasma drifts can be very large. The neutral samarium cloud that developed during that experiment was dragged significantly by the ionized portion while also following a similar drift pattern to the neutral TMA trail released near the same time, thus suggesting that the neutral and ion portions of the samarium cloud can and do interact with one another. It is therefore difficult to say to what extent the stronger eastward neutral wind during MOSC-1 was due to geomagnetic activity, day-to-day variability, or the 15-minute local time difference between the two launches.

4.7 Summary

In this chapter, we have discussed several chemical tracer experiments in the F region near sunset. Previous equatorial sunset rocket experiments did not incorporate F region wind measurements, but they have provided data that encouraged simultaneous measurements of E and F region neutral and plasma drifts. We report here the first vertically-resolved F region sounding rocket wind profiles, as well as new wind measurements in the E region.

The observed F region zonal neutral wind profiles do not agree with conventional assumptions of little to no vertical gradients above 200 km. The meridional winds do agree with model predictions. This led us to the suggestion, published in Kiene et al. (2015), that the vertical propagation of the solar terminator may create thermal gradients with altitude that cause the daily reversal of the zonal wind near sunset to be later at higher altitudes.

In addition, examination of the plasma density and drift data available for the night of EVEX has raised the question of the role of the sheared F region neutral wind in suppressing spread F plume growth. This question is investigated in Chapter 5, where we develop a wind field based on these chemical tracer observations, then input that wind field into an established model of spread F development.

Chapter 5

Spread F modeling using observed neutral winds

One of the primary end goals of spread *F* research is the isolation of driving factors and the subsequent prediction of disruptive ionospheric irregularities. This has led to a rapidly developing field of spread *F* modeling. Thus far, most modeling work has focused on correlating model output with experimental observations of spread *F* and the ionospheric parameters measured near the same time. When the community at last has a model that reproduce realistic spread *F* instabilities given the observed atmospheric conditions, we can turn that model forward, hopefully using it to predict spread *F* development in real time.

Naturally, this task is not as simple as it sounds, and not just from a computational point of view. Of course, a fully robust, high-resolution, nonlinear model of the ionosphere is computationally expensive, and it is currently unrealistic to expect models to produce predictions in real time, given that the response of the ionosphere to changing conditions near sunset generally occurs over time scales of two hours or less.

However, streamlining the computing process is not the only challenge in the spread *F* modeling field. As discussed in Chapter 2, there are many potential seeding mechanisms for spread *F* instabilities, and each of them has its own driving parameters that must be fully specified in order for a model to produce realistic output. These parameters, particularly those of the neutral atmosphere, are difficult to measure. In Chapter 4, we presented a unique set of vertically-resolved neutral wind measurements that do not agree with typical assumptions about the behavior of the winds near sunset.

A neutral wind profile generated from HWM is typically used in numerical models, since there have not previously been direct, vertically-resolved neutral wind measurements. HWM and other empirical models have, by necessity, incorporated only satellite and ground-based data that produce single-altitude measurements in the *F* region, extending them vertically to cover the entire altitude range.

The neutral wind experiments presented in this work have allowed for the investigation of experimentally-measured neutral winds on the development of spread F. This chapter will detail the numerical models available, with a focus on the model developed by Aveiro and Hysell (2010). We have used an updated version of this model, courtesy of Dr. David Hysell of Cornell Univeristy, to investigate the effect of the observed neutral winds on the development of spread *F*.

5.1 Previous spread *F* modeling work

Linear theory of spread *F* growth shows clearly that the generalized Rayleigh-Taylor instability is the primary instability responsible for the large plumes commonly associated with spread *F*. Linear theory elucidates the complexity of the growth rate dependence on the background state of the ionosphere and neutral atmosphere and potential outside influences like gravity waves from night to night. In order to fully understand and model the growth of spread *F* plumes, we must turn to nonlinear computer models, which have had considerable effort devoted to them over the last quarter century.

The work of Ossakow, Zalesak, and other colleagues at the Naval Research Lab in the late 1970s and early 1980s [Scannepieco and Ossakow (1976); Ossakow et al. (1977); Ossakow and Chaturvedi (1978); Ossakow et al. (1979); Zalesak and Ossakow (1980); Zalesak et al. (1982)] represents the earliest nonlinear numerical modeling of spread *F* development. These early computer models investigated the horizontal scales over which spread *F* bubbles could develop. These models grew progressively more complex, culminating in the paper by Zalesak et al. (1982), which incorporated larger scales, neutral winds, and *E* region effects on background Pedersen conductivity. This was the first simulation to accurately show the C-shaped structures, as well as westward tilts of the plasma bubbles that are typically observed in radar data.

The next major steps in spread *F* modeling came when Sekar et al. (1994) incorporated vertical winds and zonal electric fields into a model. The results of this study, namely that downward vertical winds and eastward electric fields accelerated the growth of spread *F*, cemented the idea that the large plumes seen in spread *F* events are due to nonlinear evolution of the Rayleigh-Taylor instability.

Building upon this, Huang and Kelley (996a) incorporated gravity wave forcing into their model, finding that zonally propagating gravity waves were an efficient seeding mechanism for spread *F*. Huang and Kelley (996b) furthered this work by considering background density perturbations in more than one dimension. In this work, the neutral wind was included by specifying a gravity wave perturbation without considering the nightly atmospheric conditions.

Full three-dimensional modeling of spread *F* at last reached prominence in the late 2000s, resulting in a number of studies. Huba et al. (2008) developed a 3-D model that reproduced the large plumes and vertical velocities associated with spread F, but this model did not consider neutral winds and treated field lines as equipotentials, which reduces the dimensionality of the potential equation, simplifying the computation considerably. Huba et al. (2009) updated the model to include time-independent zonal winds, showing that model winds, e.g. HWM07, would produce tilted plumes like those seen in experiments.

Another recent model is that of Retterer (010a). This model incorporates a variable background ionosphere in an attempt to reproduce and investigate daily variability in spread F. The model is able to produce detailed small-scale scrutcure both directly in plasma density and through inferring the change in airglow emissions based on the plasma density shifts. Retterer (010b) furthered the study by using the simulation results to recreate radio scintillation maps, producing realistic spread F signals as a radar might see them. These studies incorporated neutral wind data from Hedin et al. (1991) that was based upon satellite and ground-based measurements.

Keskinen (2010) investigated the effect of gravity waves on spread F bubble development. This model solved the plasma density, momentum, and current continuity equations for the volume between 100 and 250 km altitude near the equator. Results from the study showed that gravity wave perturbations can generate drive large electron density perturbations in the lower F region, but the model did not extend to altitudes above 250 km.

Hysell and Kudeki (2004) were the first to model the contribution of collisional shear instability to the growth of larger Rayleigh-Taylor spread F plumes, building upon the formalism developed by Keskinen et al. (1988). The theoretical work begun in that study was used to construct another fully three-dimensional model, that of Aveiro and Hysell (2010), an updated version of which was used to produce the results of this study. It is discussed in greater detail below.

5.2 The Aveiro-Hysell model

Building on the work of Hysell and Kudeki (2004), Aveiro and Hysell (2010) detailed a model that produced full 3-D solutions to the potential equation, rather than assuming equipotential magnetic field lines. This model also accurately described the ionospheric valley region, which is important to the development of collisional shear instability (see section 2.5.3). The growth of CSI depends on where the vertical shear node falls with respect to the background plasma density gradient. Hysell et al. (2014) and Hysell et al. (2015) later used an updated version of the model in a series of case studies in the Peruvian sector using Jicamarca data. The model solves for the abundances of four ion species (O^+,NO^+,O_2^+, and H^+) as a function of time, starting from inital conditions.

The first major calculation performed by the model is the solution to the potential equation. This arises from the quasi-neutrality condition, $\nabla \cdot \mathbf{J} = \nabla \cdot (\sigma \cdot \mathbf{E}) = 0$, where the electric field $\mathbf{E}$ is divided into a background component $\mathbf{E_0}$ and the gradient of the scalar potential ϕ. The current density itself can be expressed (summing over all the species, s):

$$\mathbf{J} = \sigma \cdot (\mathbf{E} + \mathbf{u} \times \mathbf{B}) - \sum_s q_s \mathbf{D_s} \cdot \nabla n_s + \Xi \cdot \mathbf{g} \tag{5.1}$$

where σ is the conductivity tensor, $\mathbf{D_s}$ is the diffusivity tensor for species s, and Ξ is a tensor that contains the total current driven by gravity. The values of these quantities are given by Shume et al. (2005) for cases neglecting Coulomb collisions. Coulomb collisions are incorporated by decoupling the paralell velocities of each species through linear transformations. The full partial differential equation that is solved is then

$$\nabla \cdot (\sigma \cdot \nabla \phi) = \nabla \cdot [\sigma \cdot (\mathbf{E_0} + \mathbf{u} \times \mathbf{B}) - \sum_s q_s \mathbf{D_s} \cdot \nabla n_s + \Xi \cdot \mathbf{g}] \tag{5.2}$$

which is an elliptic partial differential equation for ϕ. This is free of cross-terms when posed in a magnetic dipole coordinate system (p, q, Φ), where p is the McIlwain parameter (akin to the L-shell, measured in Earth radii), Φ is longitude, and q is the other orthogonal coordinate similar to latitude. For a more detailed discussion of the magnetic coordinates, see Swisdak (2006). Equation 5.2 is solved using the BiConjugate Gradient Stabilized (Bi-CGStab) method [e.g., van der Vorst (1992)] by employing the SPARSKIT algorithm toolbox developed by Saad (1990).

The second computation performed is

$$\frac{\partial n_s}{\partial t} + \nabla \cdot (n_s \mathbf{v_s}) = P - L \tag{5.3}$$

which is the time advance of the ion continuity equation for species s. The updated electrostatic potential from above is used to calculate $\mathbf{v_s}$, and P and L represent chemical production and loss via charge exchange between oxygen and hydrogen, as well as between oxygen and molecular ions and dissociative recombination of molecular ions. The rate coefficients for these reactions are taken from Schunk and Nagy (2004). Inertia is not included in the model, meaning the convective derivative term in Equation 5.3 is the only remaining nonlinear term. This term does not cause turbulence or chaotic behavior, instead producing small-scale structure without involving an energy cascade (Hysell, 2016).

The simulation is run on a grid that is 159 x 133 x 189 points wide in (p, q, Φ) space. The vertical extent is from ~90 to ~570 km and is 10 degrees longitude by 30 degrees latitude, centered on the geomagnetic equator. Instability is artificially seeded by the addition of gaussian white noise to the background electron density at a maximum relative amplitude of 20% (Aveiro and Hysell, 2010). This noise causes the small displacements that destabilize the boundary layer, facilitating the growth of shear instabilities (Aveiro et al., 2012). The model output is not sensitive to the seed of the white noise distribution; longitude and local time variations of the background parameters are more important (Hysell, 2016).

5.2.1 Model Inputs

Because the growth rates of equatorial ionospheric instabilities depend heavily on the background state of the atmosphere, accurate specification of these background parameters is of great importance to producing realistic output. These background quantities are derived from a variety of empirical models, most of which are widely used and are standard in the field.

The background plasma density is derived from the Parameterized Ionospheric Model (PIM) (Daniell et al., 1995), with minor tuning based on the daily value of $F_{10.7}$ solar flux. PIM has been compared favorably with other empirical models and, with the tuning, reproduces electron density profiles observed from Kwajalein and Jicamarca (Aveiro and Hysell, 2010).

Plasma composition is derived from the International Reference Ionosphere (IRI-007) Model (Bilitza and Reinisch, 2008). Neutral composition and temperature estimates are obtained from the Mass Spectrometer and Incoherent Scatter (NRL-MSISE00) model (Picone et al., 2002). By default, zonal neutral winds are obtained from the Horizontal Wind Model (HWM-14) (Drob et al., 2015), though these winds are replaced with the wind field described in Sec. 5.3 when modeling the EVEX case. Expressions for the ion-neutral and electron-neutral collision frequencies are taken from Richmond (1972), and expressions for the Pedersen, Hall, and parallel mobilities and diffusivities are found in Kelley (2009).

As a default, the background electric field is specified based on vertical plasma drifts from the model established by Scherliess and Fejer (1999). This empirical model is based on average plasma drifts from several years of Jicamarca measurements. The model specifies a vertical plasma drift in the bottomside F region, but only at a single altitude point. Based upon the vertical plasma drift from the model, and the known magnetic field, the model works backward from $\mathbf{v} = \mathbf{E} \times \mathbf{B}$ to calculate a zonal electric field. The electric field is then scaled by a hyperbolic tangent function centered near 300 km in order to create representative magnitudes above and below the F peak. This has the added benefit of suppressing lower-altitude, small-scale E region instabilities that have a destabilizing effect on the code.

Simply scaling plasma drifts produced by the Scherliess-Fejer model captures only the changing magnetic field magnitude as a function of altitude. It does not account for any shears in the neutral winds. This is a valid assumption when the background neutral wind is specified by, e.g., HWM-14; however, the winds we have presented here do not show the same patterns in the F region as HWM-14.

Zonal neutral winds are the primary driver of the zonal electric fields that cause the vertical $\mathbf{E} \times \mathbf{B}$ drifts of the prereversal enhancement. Thus, the behavior of the prereversal electric fields will show significant dependence on the behavior of the zonal wind. Based on the model drifts of Scherliess and Fejer (1999), the magnitudes of the vertical drifts are approximately 50% of that of the neutral wind. For these model runs, we have replaced the model plasma drifts with this approximation in order to ensure consistency between the timing of the neutral wind reversal and the enhancement of the zonal electric fields, which should be strongly correlated during the two-hour period near sunset.

5.2.2 Measured neutral wind input

The aim of this study is to examine the effects of the unexpected westward drifts and cross-terminator shears observed in the EVEX experiment on the development of spread-F in the model. The EVEX measurements are obviously constrained to a single point in space, but we were able to show that the neutral winds change rapidly with local time, reversing direction in a period of around 20 minutes. The simulation window of 10 degrees longitude corresponds to 40 minutes of local solar time. Thus, we can set the center of the window at the local time of the EVEX measurements to correspond to the earlier EVEX wind profile, with the eastern edge corresponding to the later EVEX profile. We set the field to evolve with time, propagating westward with the terminator. The winds then evolve over the course of an hour toward the winds retrieved from HWM-14. The wind field derived from the EVEX winds that is used as an input for the model runs in this work is shown in Figure 5.1 for the initial time (0745 UT), as well as simulation times of 15, 30, 45, and 60 min. Initially, there are very sharp vertical and longitudinal gradients. The field evolves to the point that the winds are nearly uniformly eastward, with very small longitudinal and vertical gradients.

5.2.3 Model results

In the above sections, we have described the various inputs to the numerical model. Here, we present the results for two neutral wind cases. The first case is a baseline run using winds from HWM14. This is the typical input for numerical models. Electron density plots from this run are shown in Figure 5.2 for simulation times of 0, 15, 30, 45, and 60 min. The longitude is centered at 167° E, near the launch site.

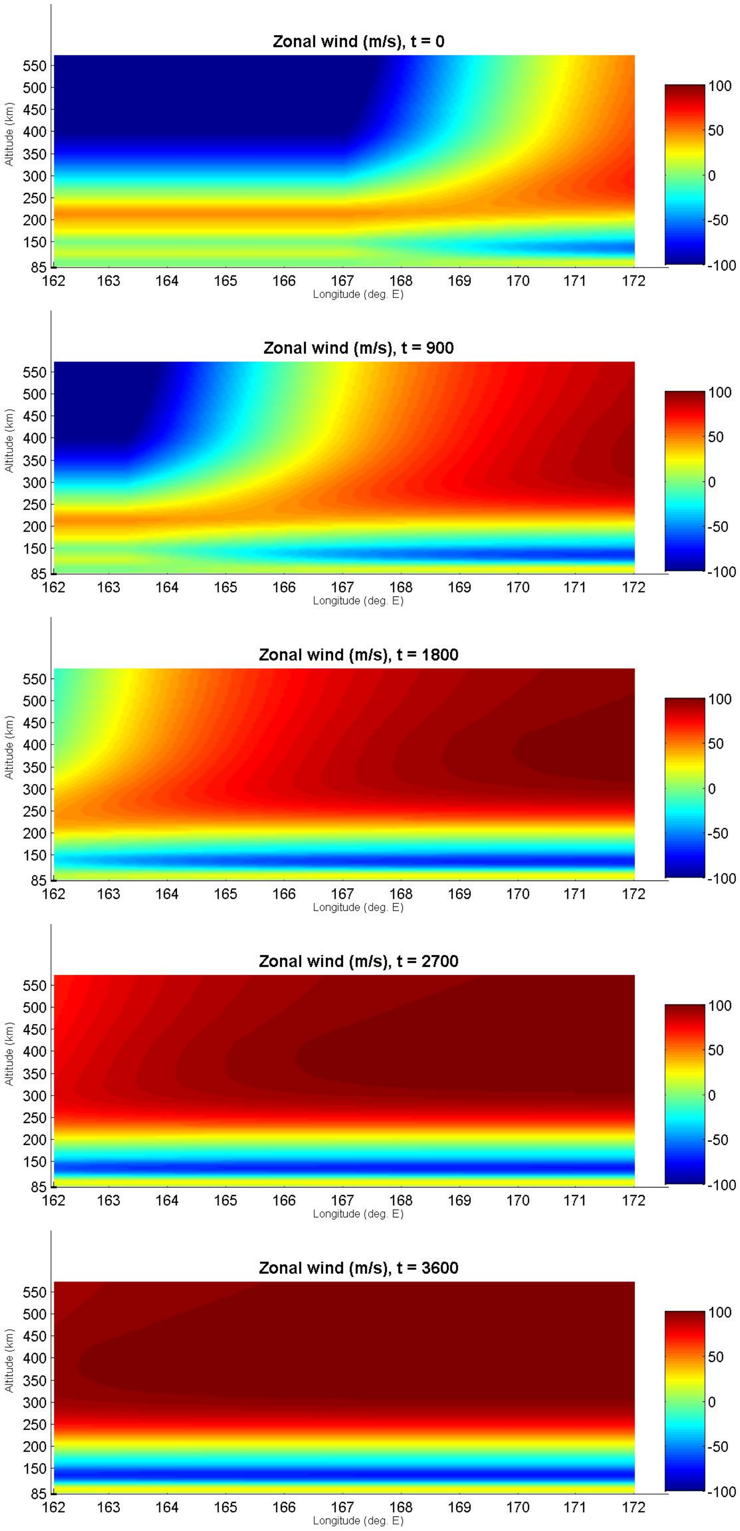

Figure 5.1: Wind fields over Kwajalein from for simulation times of 0, 15, 30, 45, and 60 min. after the EVEX launch.

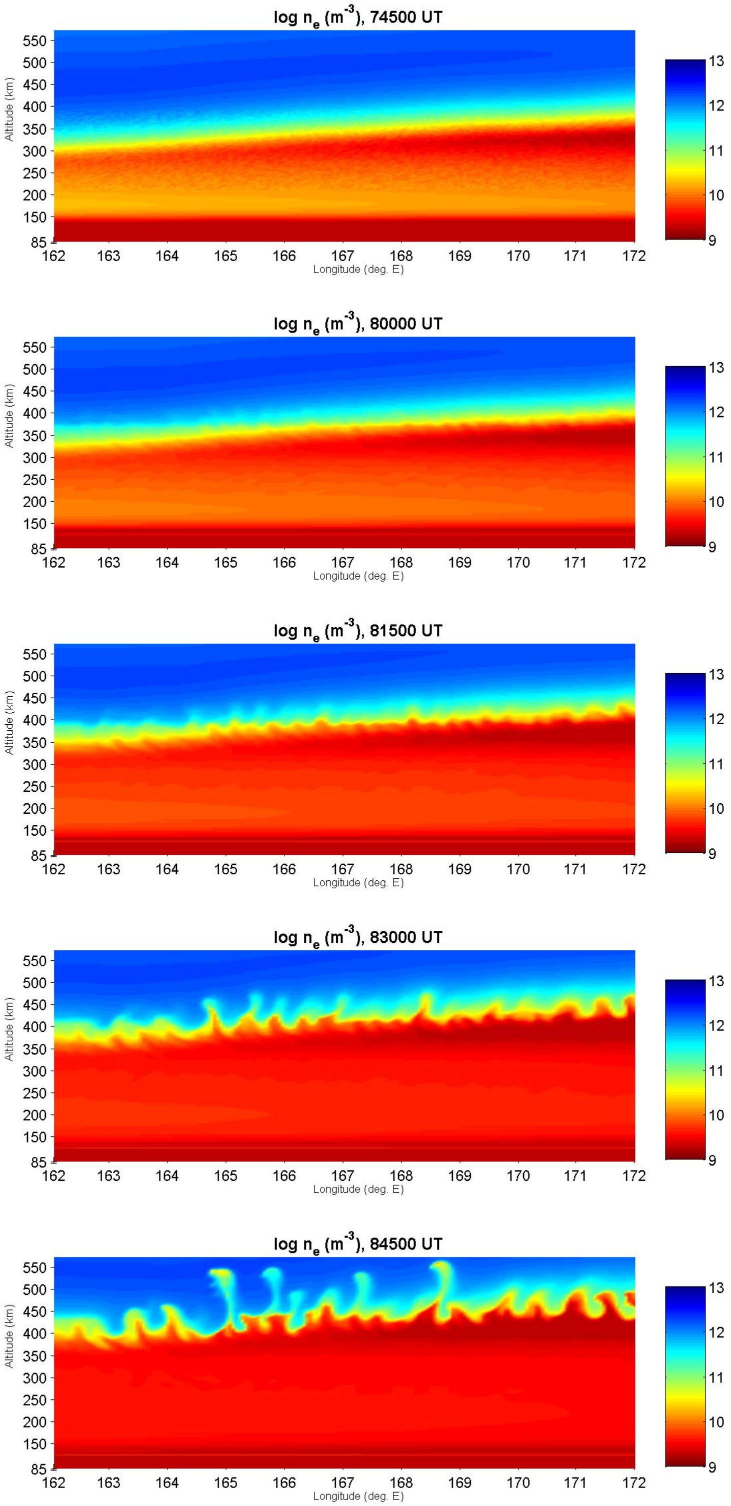

Figure 5.2: Results from the model run that used HWM winds throughout the simulation. Electron density at 0, 15, 30, 45, and 60 min. after the EVEX launch.

We then ran the model with a wind field based on the EVEX measurements, as shown in Figure 5.1, with the electric fields based on the approximation discussed above. A series of plots are shown in Figure 5.3 for simulation times of 0, 15, 30, 45, and 60 min., after which the plumes extended beyond the boundaries of the simulation.

As discussed in Chapter 4, the EVEX winds showed two different unexpected characteristics. First, winds were westward near sunset in the *F* region. Second, the wind profile was strongly sheared with altitude. Either of these effects could be a contributor to spread *F* variability, and so two further simulations were conducted using wind profiles that individually accounted for these effects. The first simulation used a wind profile that was strongly sheared beginning near 250 km, but remaining positive (eastward) throughout the altitude range of the simulation. The second model run used a wind profile that reached a 50 m/s westward wind near 250 km altitude, then stayed constant with altitude. Results from these model runs are shown in Figures 5.4 and 5.5, respectively.

5.3 Discussion of model results

The four model runs presented in the previous section illustrate the effect of eastward winds and shear instabilities on the development of spread *F* plumes. This is the first time experimentally measured neutral winds have been directly applied to this model.

The development of large plumes even in the presence of westward, sheared wind is a particularly interesting result. One of the principal advances of the modeling work of Aveiro and Hysell (2010) was the inclusion of collisional shear instability (CSI) in the bottomside *F* region. We discussed the instability in Section 2.5.3, along with

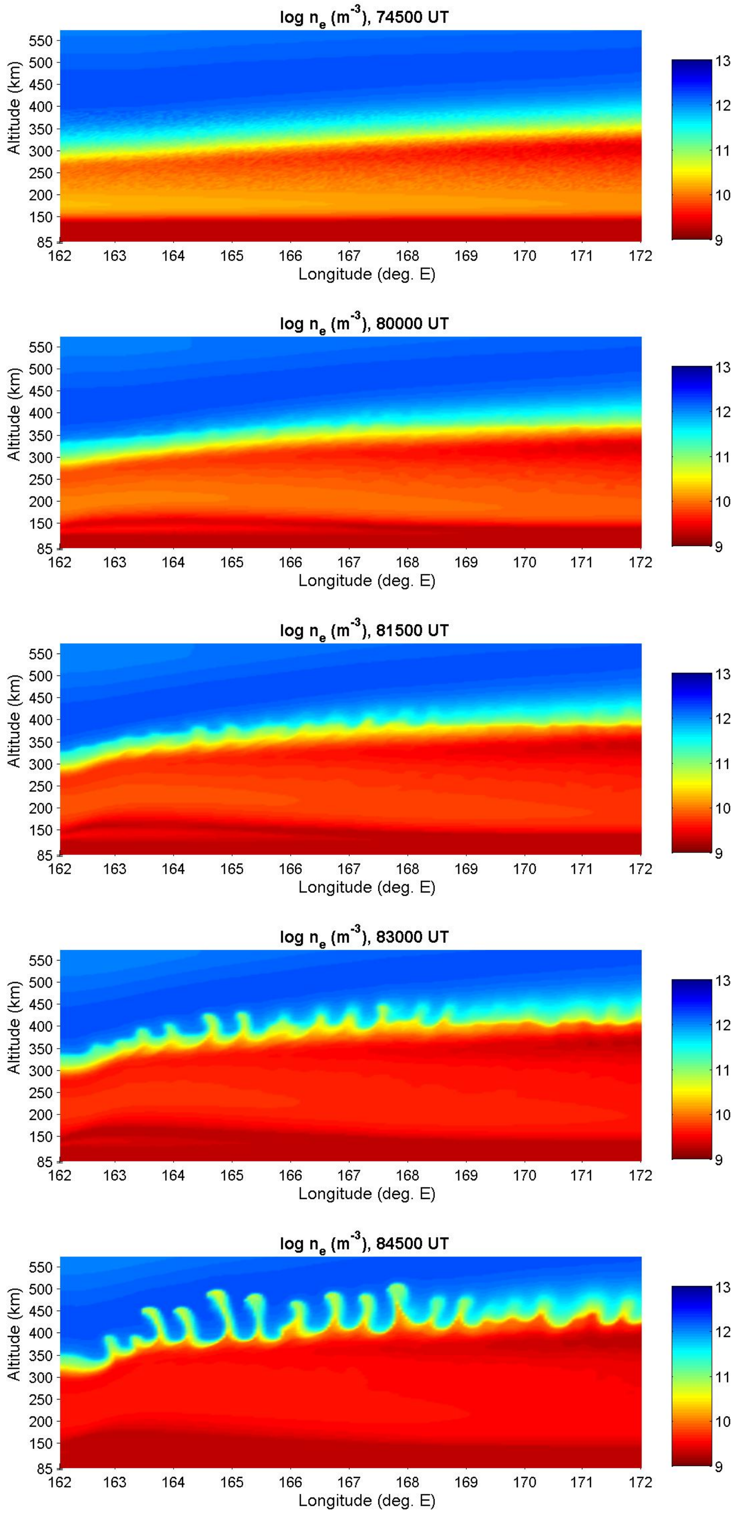

Figure 5.3: Results from the model run that used EVEX wind profiles to derive the wind field. Electron density at 0, 15, 30, 45, and 60 min. after the EVEX launch.

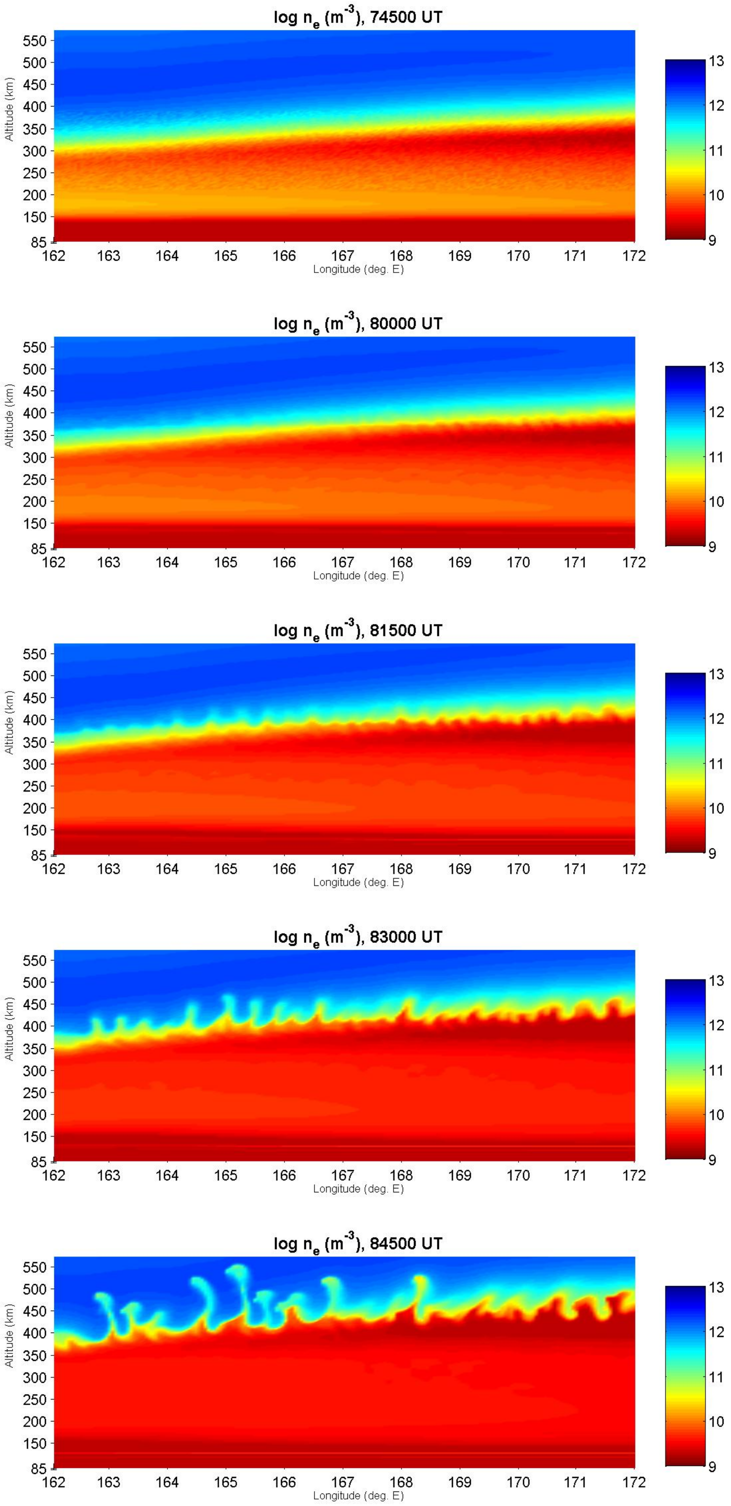

Figure 5.4: Results from the simulation run that used a sheared, eastward wind profile above 250 km to derive the wind field. Electron density at 0, 15, 30, 45, and 60 min. after the EVEX launch.

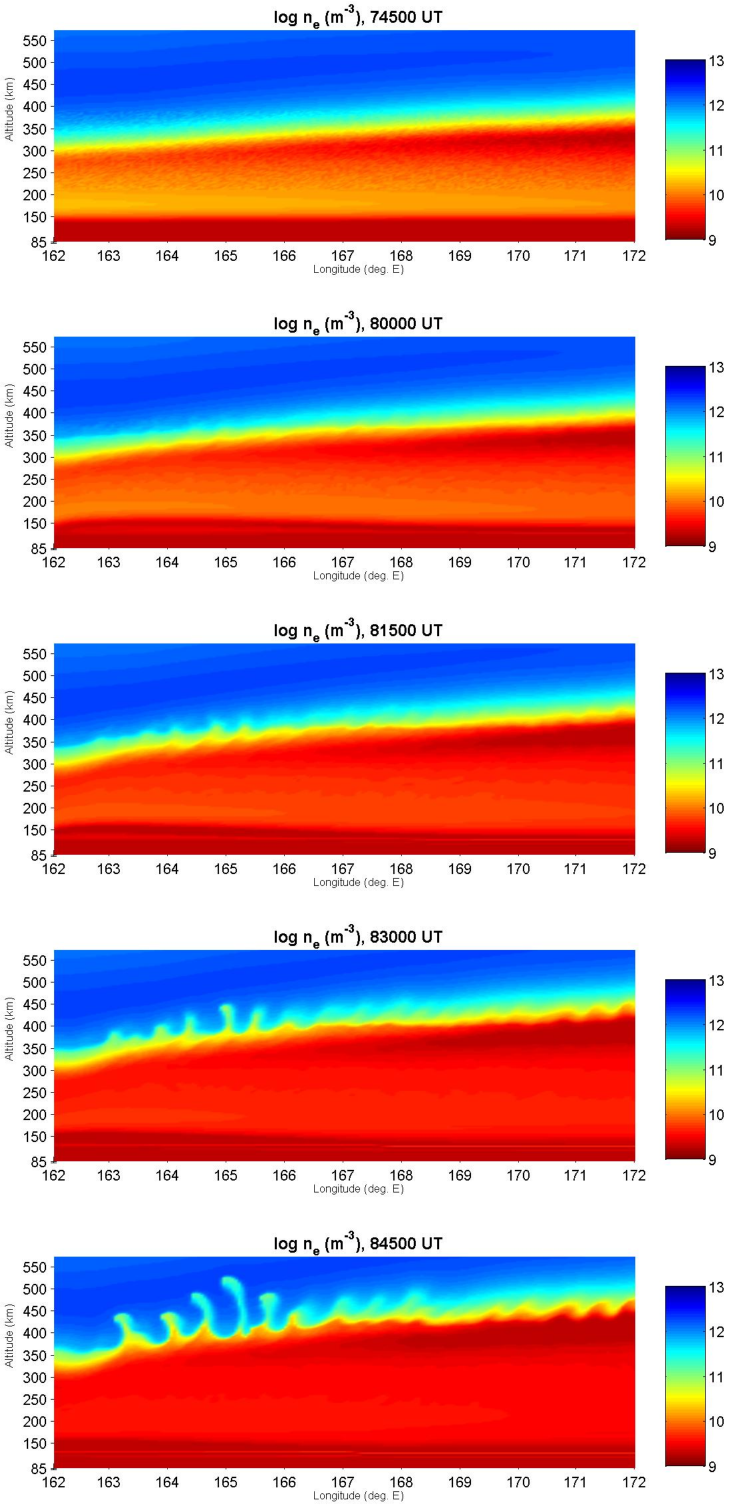

Figure 5.5: Results from the simulation run that used a constant westward wind profile above 250 km to derive the wind field. Electron density at 0, 15, 30, 45, and 60 min. after the EVEX launch.

its potential contributions to the development of large Rayleigh-Taylor plumes later in the evening. The growth rate of the instability depends on the magnitude of the difference between the neutral velocity and plasma velocity and is approximated by Hysell et al. (2006) as (in dipole coordinates):

$$\gamma_{CSI} \propto \langle \frac{h_q}{h_p} \sigma_P (u - v_o) n_o' / n_o \rangle \tag{5.4}$$

where the angle brackets denote integration over a flux tube. The direct dependence in the integral of $(u - v_o)$ implies that, if the zonal neutral wind is uniformly eastward (as models suggest) and the zonal ion drifts are positively sheared (as seen by Kudeki et al. (1981)), the contribution of the $(u - v_o)$ term to the integral will be large when the altitude range in which the ion drifts are westward is captured in the flux tube integration and small when it is not. According to typical model winds, u is almost always greater than v_o early in the evening, and thus the contribution of the wind term to the growth rate is always positive.

However, in the case of a vertically sheared wind, when the wind term is integrated over the entire flux tube, the altitude regions where $(u < v_o)$ will contribute negatively to the overall integral. Given that plasma drifts typically follow an eastward shear pattern with altitude, with the transition altitude from westward to eastward rising as the night goes on (Kudeki et al., 1981), the plasma drift is therefore likely to be eastward in the bottomside F region near sunset when the chemical tracer experiments occurred. This means that the westward winds would create a region of small growth rate for the collisional shear instability.

The obvious question is whether the model output shows this effect. The results presented by Aveiro and Hysell (2010) are very useful for comparison. In that paper, the authors show model output for three separate cases. First, they fix the neutral wind at zero, which suppresses shear flow, inhibiting the shear instabilities and allowing only Rayleigh-Taylor instability to develop. The second case switches off the background electric fields and gravity, while restoring the neutral wind. This suppresses the R-T instability, leaving the resulting ionosphere to be dominated by collisional shear instability. The third case includes all inputs, resulting in a combination of both instability processes.

Results from these model runs at t = 60 min are shown in Figure 5.6. The Rayleigh-Taylor instability alone causes smooth, laminar plumes that have much smaller depletion magnitudes relative to the background. Collisional shear instability, when operating alone, causes much stronger, more structured depletions, but they do not extend nearly as far vertically. It is only when combined that the instabilities produce plasma depletions that are both strong in magnitude, large in vertical extent, and highly structured like those seen by radar measurements.

The morphology of the plumes produced by the run using EVEX winds is very similar to the structure shown by the zero-wind case of Aveiro and Hysell (2010), which was designed to suppress CSI growth. This is consistent with the above conclusion that CSI growth would be small in the F region under the sheared neutral wind conditions. The plumes penetrate higher and are significantly more laminar than the turbulent plumes created when CSI is present in the Aveiro and Hysell (2010) model.

Some very interesting effects also crop up near the edges of the EVEX simulation. On the eastern edge, the plumes are less well-defined, and electron densities are lower. This may be due to the fact that the sheared wind structure vanishes earliest on the eastward side of the simulation, allowing for a larger window of CSI growth that creates more turbulent plumes than the western side. These eastern plumes look much more similar to the plumes seen in Figure 5.2, indicating that CSI may be responsible. Another difference between the two simulations is in the altitude of

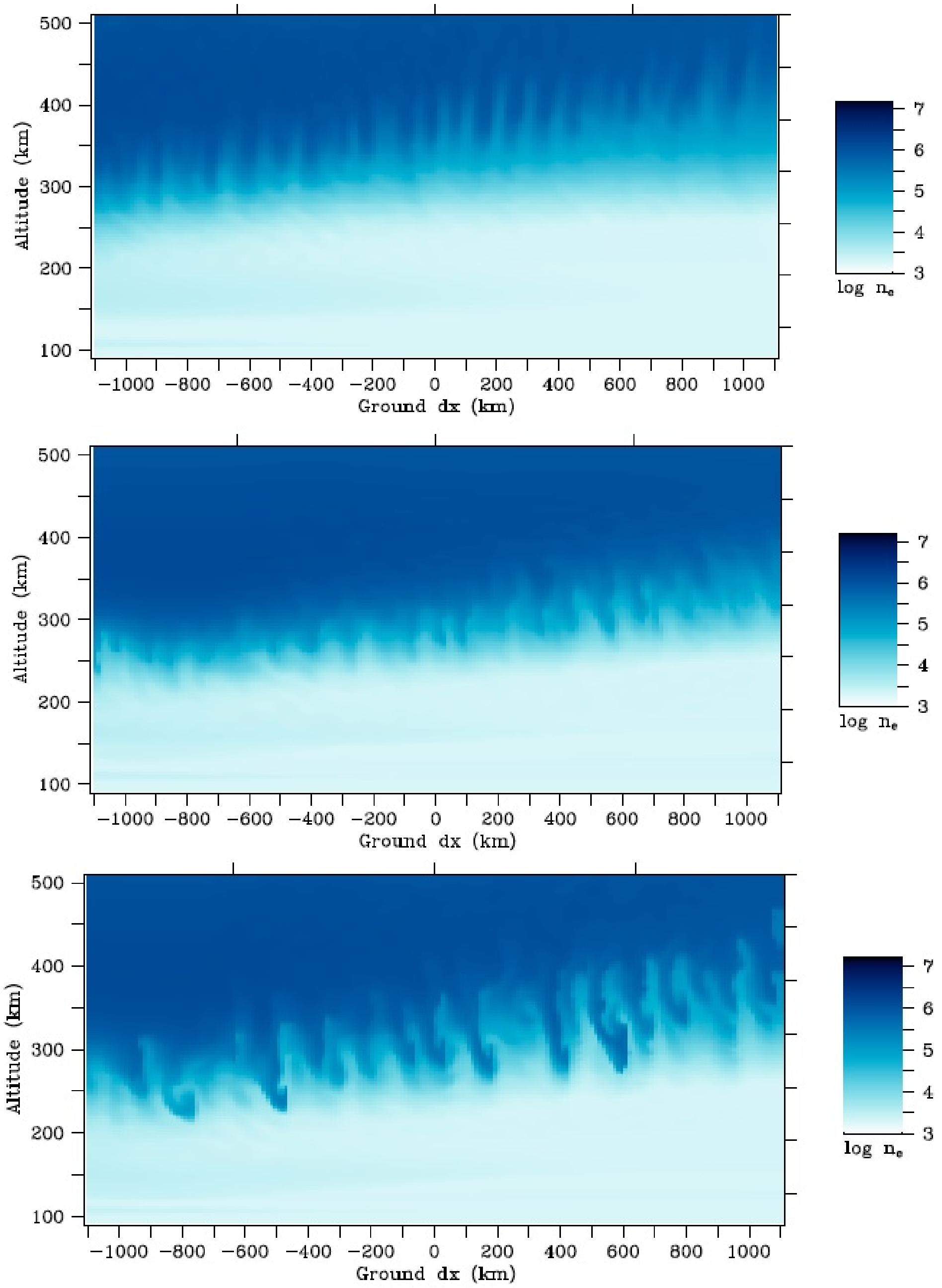

Figure 5.6: Simulation results presented by Aveiro and Hysell (2010) showing three different cases: (Top) strictly Rayleigh-Taylor instability; (Middle) strictly collisional shear instability; (Bottom) both instabilities present.

the layer in which the instabilities occur. In the EVEX case, where there are strong longitudinal gradients in the zonal wind, the western side, where the westward winds persist for longer, shows a significantly lower layer height than the eastward side. No plumes develop in this area. There are longitudinal gradients in the HWM case, but they are much smaller than in the EVEX case, and so there is not much of a difference in altitude of the layer in the HWM case.

The differences in these two cases illustrate how variations in the neutral wind can affect the development of spread *F*. The measurements from the EVEX and Guara campaigns represent only three nights of data (two of them consecutive), so it is unclear how representative these sheared wind profiles are of the typical sunset thermosphere. Further studies would be required to definitively say how often such shear is present and whether it varies in magnitude.

The HWM case shows larger depletions that extend to higher altitudes. The plumes that develop also exhibit much more structure when compared to the smooth, well-shaped plumes of the EVEX case. This is the same effect that is shown in Figure 5.6 when CSI is included in the simulation along with the Rayleigh-Taylor instability.

The model results presented in Figures 5.5 and 5.4 show that it is primarily the westward wind that suppresses CSI development, rather than the fact that the wind is sheared. The case of eastward, sheared wind in Figure 5.4 shows similar morphology to the HWM case, indicating that the shear did not contribute significantly to the suppression of CSI observed in the EVEX case. The case of the westward wind profile without shear showed similar morphology to the EVEX case, suppressing the bottomside turbulence and creating smooth, weaker plumes. The westward wind, though smaller in magnitude than the maximum westward wind observed during EVEX, actually created even weaker spread *F* activity than the EVEX case. This is likely due to the region of eastward winds below 260 km observed early in the EVEX experiment. These eastward winds were not sufficient to generate bottomside turbulence, but may have contributed positively to the spread *F* plumes that did develop.

The westward flow observed in the EVEX case suppresses the CSI growth rate, thus reducing the strength of the seed instabilities that lead to fully developed plumes. If the westward flow is strong enough, or if it persists for long enough, it may be enough to suppress spread *F* entirely. Daily variability in the shear flow may therefore be a contributing factor to the daily variability of spread *F* development.

The model results of Aveiro and Hysell (2010), while useful for comparison due to the nature of the study, come from an older version of the model. Updated versions produce much more realistic plumes. The most recent published study using the model is that of Hysell et al. (2015), who continued the data-driven simulation campaigns begun by Hysell et al. (2014). Hysell et al. (2015) did not include FPI winds because the solstice season does not have good weather conditions for ground-based observations. Instead, they used the newly-released HWM14 winds. This makes for a useful comparison to the HWM case presented here. Our model run differed in that we directly defined the electric fields using the HWM neutral winds, while the default model uses the Scherliess and Fejer (1999) model to compute electric fields sepearately from the HWM neutral winds, and so it is useful to have a check on whether this is a good approximation. Hysell et al. (2015) were also modeling in the Peruvian sector, while our model runs are for the Kwajalein sector. Their results are shown in Figure 5.7. Despite the different longitude, the two results show similar morphology, with a few larger plumes extending out of a turbulent bottomside layer. This suggests that our electric field approximation is valid because it produces output similar to that of the Scherliess and Fejer (1999) model.

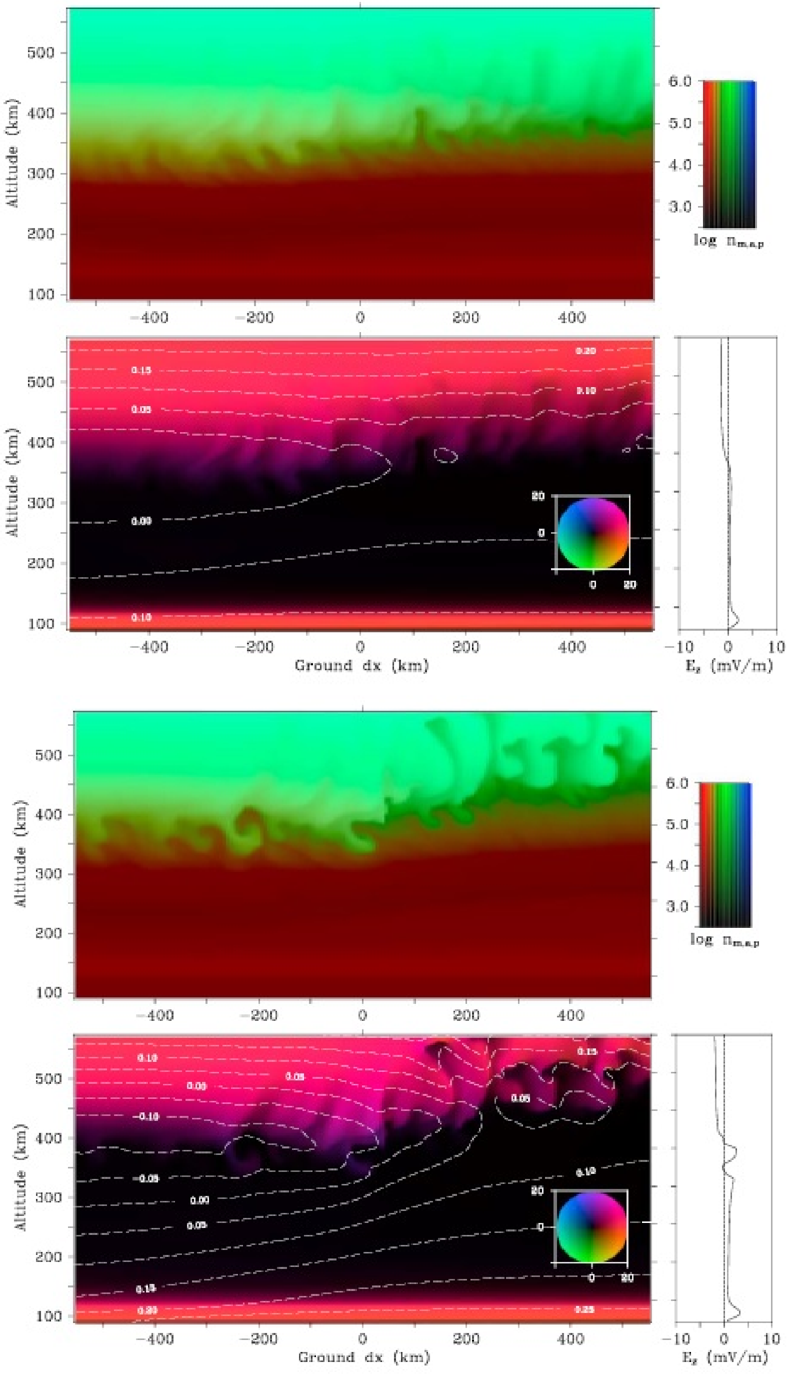

Figure 5.7: Data-driven numerical simulation results for two nights in Dec. 2014, one with low ESF activity (left) and one with high activity (right). The top row shows plasma density with red, green, and blue tones representing molecular, atomic, and protonic ion abundance, respectively. The bottom row shows current density in nA/m^2. The white lines are equipotentials, and the vertical electric field profile is plotted to the right. Figures from Hysell et al. (2015)

Hysell et al. (2014) did incorporate Fabry-Perot neutral winds as a part of their data-driven study of spread F over Jicamarca, but these winds came from a single altitude near 250 km. The authors created a profile based on HWM winds that shifted the shear node up or down based on whether the FPI showed westward or eastward winds. This approach produced results that contradicted the radar observations, leading the authors to conclude that further experimental results were needed. The model runs of Hysell et al. (2015) did not include FPI data because the campaign was conducted in the rainy season, which did not have sufficient clear skies for reliable FPI measurements. That study performed somewhat better at reproducing the observed spread F plumes. The modeling study performed here builds upon these studies, being the first to incorporate direct, vertically-resolved wind measurements. The chemical tracer measurements show an environment that is not conducive to shear instability growth, and the model results agree with that conclusion.

The plume morphology differs significantly between the HWM and EVEX cases. The EVEX winds lead to much smoother, laminar plumes, with very little bottomside turbulence. The plumes are also relatively evenly spaced, with roughly 50 km between plumes. The HWM winds lead to a much more turbulent bottomside region, with irregular plumes. The large differences in structure between the two modeled spread F events are also observed in radar measurements. Figure 5.8 shows eighteen different nights of spread F measurement using the JULIA radar at Jicamarca, compiled by Kelley and Ilma (2016). These were deemed “more or less similar” by the authors, yet there are still significant differences in the behavior of the plumes. Some plumes are very smooth and show little structure, while some are much more turbulent. The width of the plumes, as well as the spacing between plumes in local time are highly variable. These plots represent but a small fraction of the available radar data. Other events reproduced here (Figure 2.6 and Figure 2.10), as

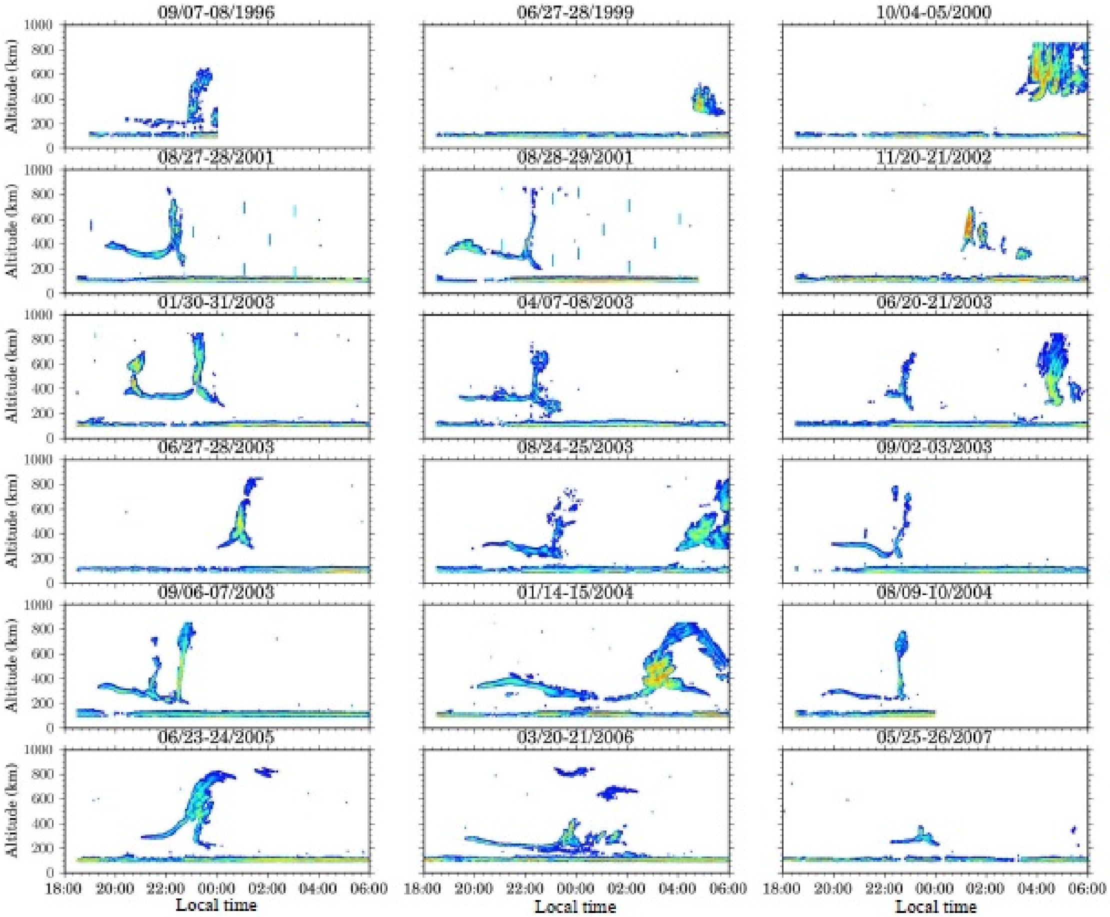

Figure 5.8: Eighteen range-time-intensity plots of spread F nights from the JULIA radar. Figure from Kelley and Ilma (2016).

well as those displayed throughout the literature, show many different morphologies. Based on the modeling results shown here, the neutral winds are likely a significant factor in the variability observed in the daily morphology of spread F plumes. While Chapter 2 was devoted to the many ways in which spread F could be modulated on a daily basis, these modeling results show that neutral winds have a significant effect on the plume shape, bottomside turbulence, and overall magnitude of spread F events.

5.3.1 Potential shortcomings

As discussed previously, the model is initialized using white noise. While it does a good job of producing instabilities generated as a result of this generic perturbation upon the specified background conditions, the model does not include any of the external factors which are often cited as producing day-to-day variability in spread *F*. These include the external factors discussed in Section 2.4.1: gravity waves, sporadic *E* layers, and LSWS. The model also does not consider medium-scale traveling ionospheric disturbances (MSTIDs) that propagate equatorward from middle latitudes and destabilize the equatorial zone. Krall et al. (2011) successfully modeled this phenomenon, which was directly observed by Miller et al. (2009). MSTIDs remain a prime candidate for a source of daily variability in spread *F*. The model also does not consider any geomagnetic storm effects, though there was no activity on the night of the EVEX experiment.

The seed of the white noise itself does not have a large impact overall evolution of the instabilities (Hysell, 2016). This is evident in Figure 5.9. Shown are model runs conducted with different random seeds, two using the HWM wind field and two using the EVEX wind field. The differences between the two cases are very minor. The presence of turbulence in the bottomside region and in the subsequent plumes is consistent between the two HWM cases, while its absence is consistent in the EVEX cases.

In addition to the above factors, we must simply consider the fact that our model inputs may not fully specify the actual background parameters present during the spread *F* event. While empirical models have been shown to be relatively accurate, they are large, fitted aggregations of many data sets over many years. They provide weighted averages, which will fail to account for the potential day-to-day variability

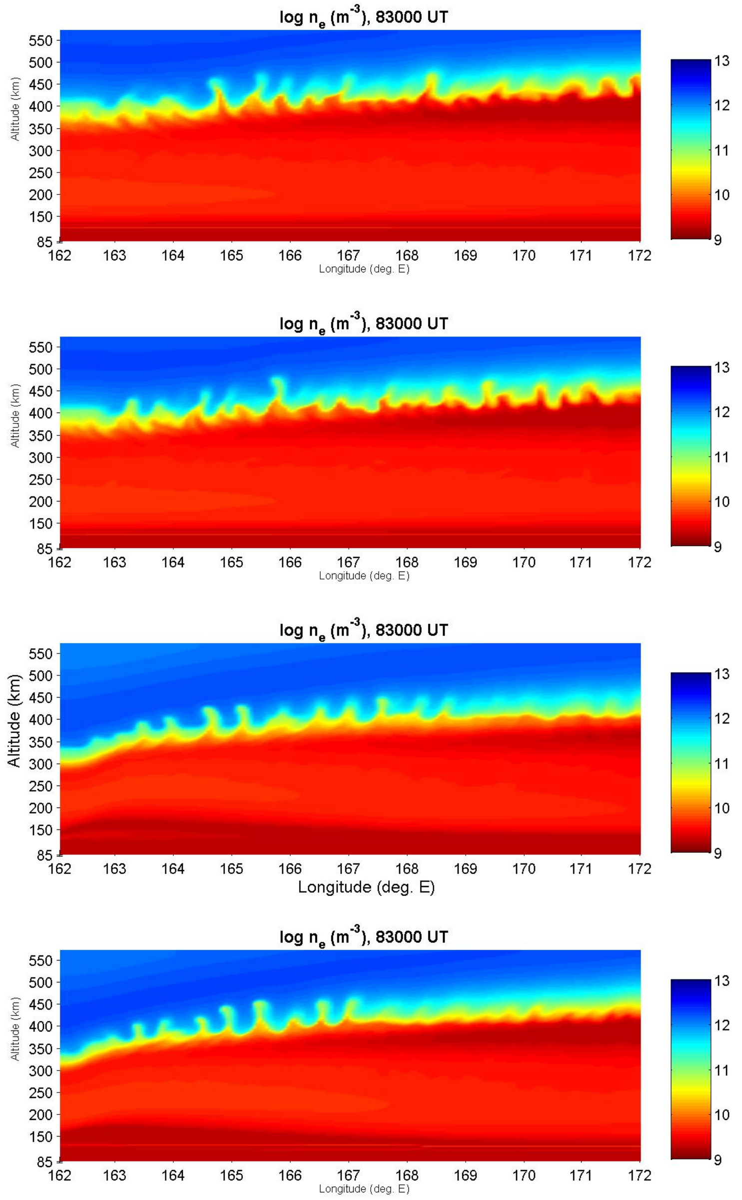

Figure 5.9: Model results comparing the effect of different white noise seeds. The top two plots represent runs using the HWM14 wind field, while the bottom two plots represent runs using the EVEX winds field. The presence or absence of turbulence is consistent between the different seeds, indicating that changing the noise seed will not have a major effect on the evolution of spread F in the model.

that may be present in background parameters. When considering a model such as the one used here, which spans a volume approximately 1000-by-3000-by-400 km, some deviation in the actual background parameters of a night in question from averaged empirical models must be expected. This is especially true for the wind field constructed to mimic the EVEX winds. We have no knowledge of how the winds were behaving away from the rocket trajcetory. It is likely that the wind field behaves qualitatively as described, but many of the external drivers mentioned above are capable of causing disturbances in the wind field. Without a detailed measurement campaign, it is difficult to be completely sure that all background parameters are correctly specified. The data-driven campaigns of Hysell et al. (2014) and Hysell et al. (2015) are a good start to such a data set, and the eventual goal of this project is to further that work by using the EVEX winds in conjunction with other measurements taken during the campaign, once those results become available.

5.4 Chapter Summary

In this chapter, we have discussed various numerical spread F models. In particular, we focus on the model of Aveiro and Hysell (2010), which we ran in conjunction with the neutral wind observations presented in Chapter 4. We compare model results using the observed neutral winds with results obtained using model winds that are typically used for model inputs.

The modeling studies beginning with Aveiro and Hysell (2010) have shown that stronger plasma depletions develop when both shear instability and Rayleigh-Taylor instability are in full effect. The modeling work presented here supports that result. When westward, sheared flow is present in the F region, the instability plumes that develop are smaller both in size and magnitude, regularly spaced, and very smooth, with little bottomside turbulence. When the sheared flow is ignored in favor of typical model winds, the plumes are larger, more irregular, and much more turbulent. To date, this is the first modeling study that has employed vertically-resolved neutral wind measurements as input. Several data-driven campaigns have been conducted using the Aveiro-Hysell model, but they have lacked good neutral wind information. A future campaign combining both rocket measurements and ground-based observations would do much to illuminate the influence of neutral winds on ionospheric instabilities.

Chapter 6

Conclusions and future work

Fairly recently, Woodman (2009) wondered whether the spread *F* question had, in principle, been solved. His conclusion was that the theory was very well understood, and that we would soon have the capability to predict the occurrence of spread *F*, provided that we had information about the background state of the ionosphere and neutral atmosphere. The problem would then be, for all practical purposes, solved. This would require accurate nightly measurements of both the neutrals and the plasma well enough in advance of spread *F* development to potentially mitigate its effects.

In Chapter 2, we discussed the various processes that can influence the development of spread *F* instabilities. When the sun sets on the ionosphere, ion production ceases, and recombination processes combine with thermal gradients to create conditions that are sucseptible to many types of instabilities and destabilizing influences such as gravity waves. We showed that nearly all of these instability process share a key parameter in their growth rates, which is the neutral wind. The neutral wind is thought to control the magnitude of the prereversal enhancement (Eccles, 1998a), directly modulates the growth rate of the $\mathbf{E}\times\mathbf{B}$ instability discussed by Kudeki et al. (2007), and controls the magnitude of the collisional shear instability growth rate through its relationship to the local ion drifts (Hysell et al., 2006).

As is made clear by the discussion in Chapter 2, the neutral wind is a critical parameter for understanding the dynamics of the sunset equatorial thermosphere. Unfrotunately, the database of neutral wind measurements is rather sparse. In Chapter 3, we gave an overview of measurement techniques used in the equatorial *F* region. The techniques used to measure plasma parameters on a daily basis are well understood and robust. Radar measurements continue to improve, and so the bottleneck on spread *F* prediction is the neutral atmosphere, and the *F* region neutral wind in particular. It is widely known that *F* region neutral winds reverse from westward during the day to eastward at night simply based on single-altitude measurements. It is assumed that this reversal occurs at nearly the same time for all altitudes in the *F* region above approximately 200 km. However, chemical tracer measurements presented here have shown that this is not always the case.

We do have the capability to measure winds on a nearly-nightly basis with ground-based optics, provided local weather conditions are not an issue. In many cases, these instruments are located at high altitudes and/or in dry climates near the equator so that there are clear skies as often as possible. Altitude-integrated optical measurements do not, however, provide vertically-resolved wind profiles that fully specify the wind field in the *F* region, as they are only capable of producing a single-point measurement. Similarly, polar-orbit satellites pass through the equatorial region many times per day. Thus, there is good coverage of wind measurements, but these measurements take place only at the altitude of the satellite, with no information about the behavior of the winds above or below that altitude.

Sounding rockets have previously been used in the *E* region to produce vertical chemical tracer profiles that can be tracked from the ground. However, the much lower neutral density in the *F* region causes rapid diffusion of any neutral chemicals, which complicates F region tracer measurements. As a result, there have been very few F region chemical tracer experiments. In Chapter 4, we discussed three experiments that have, for the first time, produced vertically resolved F region wind measurements. These data have revealed sheared structure in the winds that was not known from single-altitude measurements. We have theorized that this structure is due to the gradual setting of the sun with altitude, which creates different thermal conditions at different altitudes near sunset, leading to the observed shear in the vertical profile. Since we have only three nights of F region data, further experiments are required to fully understand whether this is a common occurrence and whether such sheared structure in the wind profile can be correlated with spread F occurence, or lack thereof.

While there are too few measurements here to conclude anything about the climatological structure of the F region neutral winds at sunset, we have examined what effect such winds would have on spread F development. In Chapter 5, we applied our neutral wind measurements to the well-tested numerical model of Hysell et al. (2015). When compared with the nearly-uniform eastward wind produced by HWM14, the sheared westward wind of EVEX produced weaker, less structured spread F plumes. This is in line with the theory presented by Hysell et al. (2006) by which the structure of the EVEX wind profile suppresses the collisional shear instability growth rate, leading to less turbulence in the bottomside region. Further experimental data from the EVEX experiment was not currently available at the time of this writing. In the future, once the radar data is made available, further modeling studies will be conducted similar to the data-driven studies begun by Hysell et al. (2014).

The goal of this work was to show that the neutral wind is a critical, yet poorly understood driver of sunset F region dynamics near the equator. As shown by the rocket data presented in Chapter 4, there is much left to study regarding the behavior of the neutral winds at sunset. The modeling results of Chapter 5 show that variations in the neutral wind near sunset can have significant effects on the development of spread *F* instabilities later in the evening. Thus, we conclude that a proper understanding of how neutral winds behave on a daily basis is critical to prediction of spread *F* events.

6.1 Future Work

Woodman (2009) may have wondered whether the spread *F* question had been solved, but there is still a great deal of work to be done. We have shown that the neutral wind in the sunset equatorial thermosphere is rapidly changing and more structured than conventional assumptions. Accurate prediction of spread *F* events requires knowledge of the background parameters, including the neutral wind. Models have advanced a great deal in recent years, to the point that they can produce realistic three-dimensional spread *F* instabilities on a variety of scales; however, these models make a number of assumptions about the neutral wind behavior that may not be valid at all times. As numerical models continue to improve, proper specification of the neutral wind will become more and more important. Further study on *F* region neutral wind dynamics near sunset is warranted based on the results presented here. With a broader data set, we could begin to see a clear picture of whetver the zonal winds observed by the EVEX and Guara campaigns are a usual feature or something more anomalous.

The future ICON mission (Rider et al., 2015), scheduled for launch in 2017, has the potential to contribute significantly to the lack of *F* region neutral wind data. ICON will be launched into a low-inclination orbit of 27°, meaning it will sample equatorial latitudes. The MIGHTI instrument aboard ICON will be capable of sampling the green line and red line emissions in the thermosphere, with *F* region red line vertical resolution of about 30 km (Englert et al., 2015). Though the resolution is limited, having daily measurements of sunset neutral winds in the *F* region will be a great boon to future spread *F* studies.

In addition to conducting more wind measurements in the future, there is more modeling work to be done investigating the effect of neutral wind variability on plume growth. Ideally, we could produce a model run similar to the data-driven modeling studies of Hysell et al. (2014), where Jicamarca radar density and drift measurements and FPI wind measurements were used as model inputs in an attempt to reproduce coherent scatter observations. Electric field and radar data from the night of EVEX could be used as inputs to the model in order to produce similar data-driven results. Unfortunately, these data are not yet fully available, but we plan to conduct such a study as soon as they are.

Bibliography

Abdu, M. A., Sastri, J. H., MacDougall, J., Batista, I. S., and Sobral, J. H. A. (1997). Equatorial disturbance dynamo electric field longitudinal structure and spread F: A case study from GUARA/ETIS campaigns. *Geophys. Res. Lett.*, 24(13):1707–1710.

Aveiro, H. C. and Hysell, D. L. (2010). Three-dimensional numerical simulation of equatorial F region plasma irregularities with bottomside shear flow. *J. Geophys. Res.*, 115:A11321.

Aveiro, H. C., Hysell, D. L., Caton, R. G., Groves, K. M., Klenzing, J., Pfaff, R. F., Stoneback, R., and Heelis, R. A. (2012). Three-dimensional numerical simulations of equatorial spread F: Results and observations in the Pacific sector. *J. Geophys. Res.*, 117:A03325.

Basu, S., Basu, S., Groves, K. M., Yeh, H.-C., Su, S.-Y., Rich, F. J., Sultan, P. J., and Keskinen, M. J. (2001). Response of the equatorial inonosphere in the South Atlantic region to the great magnetic storm of July 15, 2000. *Geophys. Res. Lett.*, 28(18):3577–3580.

Bates, D. R. (1950). A suggestion regarding the use of rockets to vary the amount of atmospheric sodium. *J. Geophys. Res.*, 55:347–349.

Batista, I. S., Abdu, M. A., Carrasco, A. J., Reinisch, B. W., de Paula, E. R., Schuch, N. J., and Bertoni, F. (2008). Equatorial spread F and sporadic E-layer connections during the Brazilian Conjugate Point Equatorial Experiment (COPEX). *J. Atmos. Sol. Ter. Phys.*, 70:1133–1143.

Batista, I. S., de Medeiros, R. T., Abdu, M. A., de Souza, J. R., Bailey, G. J., and de Paula, E. R. (1996). Equatorial ionospheric vertical plasma drift model over the Brazilian region. *J. Geophys. Res.*, 101(A5):10887–10892.

Bedinger, J. F. (1973). Photography of a lithium vapor trail during the daytime. *J. Atmos. Terr. Phys.*, 35:377–380.

Bhasvar, P. D., Ramanujarao, K., and Verenekar, K. G. (1965). Study of the neutral upper atmosphere winds near the equator. *Space Res.*, V:986.

Bilitza, D. and Reinisch, B. W. (2008). International Reference Ionosphere 2007: Improvements and new parameters. *Adv. Space Res.*, 42:599–609.

Booker, H. G. and Wells, H. W. (1938). Scattering of radio waves by the F region. *J. Geophys. Res.*, 43:249–256.

Carrasco, A. J., Batista, I. S., and Abdu, M. A. (2005). The pre-reversal enhancement in the vertical drift for Fortaleza and the sporadic E layer. *J. Atmos. Sol. Ter. Phys.*, 67:1610–1617.

Caton, R. G., Pedersen, T. R., Groves, K. M., Hines, J., Cannon, P. S., N.Jackson-Booth, Parris, R. T., Holmes, J. M., Su, Y.-J., Mishin, E. V., Roddy, P. A., Viggiano, A. A., Shuman, N. S., Ard, S. G., Bernhardt, P. A., Siefring, C. L., and Retterer, J. (2016). Artificial ionospheric modification - the Metal Oxide Space Cloud (MOSC) experiment. *Submitted to Radio Science.*

Costa, E. and Kelley, M. C. (1978). On the role of steepened structures and drift waves in equatorial bubbles. *J. Geophys. Res.*, 83:4359.

Daniell, R. E., Brown, L. D., Anderson, D. N., Fox, M. W., Doherty, P. H., Decker, D. T., Sojka, J. J., and Schunk, R. W. (1995). PIM: A global parameterization based on first principles models. *Radio Sci.*, 30:1499–1510.

de La Beaujardiere, O. (2004). C/NOFS: a mission to forecast scintillations. *J. Atmos. Terr. Phys.*, 66:1573–1591.

Doornbos, E. (2012). *Thermospheric density and wind determination from satellite dynamics*. Springer.

Drob, D. P., Emmert, J. T., Meriwether, J. W., Makela, J. J., Doornbos, E., Conde, M., Hernandez, G., Noto, J., Zawdie, K. A., McDonald, S. E., Huba, J. D., and Klenzing, J. H. (2015). An update to the Horizontal Wind Model (HWM): The quiet time thermosphere. *Earth and Space Science*, 2(7):301–319.

Drob, D. P. et al. (2008). An empirical model of the Earth's horizontal wind fields: HWM07. *J. Geophys. Res.*, 113(A12):A12304.

Dungey, J. W. (1956). Convective diffusion in the equatorial F-region. *J. Atmos. Terr. Phys.*, 9:304.

Eccles, J. V. (1998a). Modeling investigation of the evening prereversal enhancement of the zonal electric field in the equatorial ionosphere. *J. Geophys. Res.*, 103(A11):26709–26719.

Eccles, J. V. (1998b). A simple model of low-latitude electric fields. *J. Geophys. Res.*, 103(A11):26699–26708.

Emmert, J. T., Faivre, M. L., Hernandez, G., Jarvis, M. J., Meriwether, J. W., Niciejewski, R. J., Sipler, D. P., and Tepley, C. A. (2006). Climatologies of nighttime upper thermospheric winds measured by ground-based Fabry-Perot interferometers during geomagnetically quiet conditions: 1. Local time, latitudinal, seasonal, and solar cycle dependence. *Geophy. Res. Lett.*, 111(A12):1A12302.

Englert, C. R., Harlander, J. M., Brown, C., Makela, J., Marr, K., and Immel, T. (2015). Mighti: The spatial heterodyne instrument for thermospheric wind measurements onboard the icon mission. In *Fourier Transform Spectroscopy and Hyperspectral Imaging and Sounding of the Environment*, page FM4A.1. Optical Society of America.

Farley, D. T. (1969). Incoherent scatter power measurements: A comparison of various techniques. *Radio Sci.*, 4:139–142.

Farley, D. T., Bonelli, E., Fejer, B. G., and Larsen, M. F. (1986). The prereversal enhancement of the zonal electric field in the equatorial ionosphere. *J. Geophys. Res.*, 91(A12):13723–13728.

Fejer, B. G., de Paula, E. R., Heelis, R. A., and Hanson, W. B. (1995). Global equatorial ionospheric vertical plasma drifts. *J. Geophys. Res.*, 100:5769–5776.

Fejer, B. G., dePaula, E. R., Gonzalez, S. A., and Woodman, R. F. (1991). Average vertical and zonal F region plasma drifts over Jicamarca. *J. Geophys. Res.*, 96:13901.

Fejer, B. G., Kudeki, E., and Farley, D. T. (1985). Equatorial F region zonal plasma drifts. *J. Geophys. Res.*, 90(A12):12,249–12,255.

Fejer, B. G. and Scherliess, L. (1997). Empirical models of storm-time equatorial zonal electric fields. *J. Geophys. Res.*, 105:18391.

Fritts, D. C., Abdu, M. A., Batista, B. R., Batista, I. S., Batista, P. P., Buriti, R., Clemesha, B. R., Dautermann, T., de Paula, E., Fechine, B. J., Fejer, B., Gobbi, D., Haase, J., Kamalabadi, F., Laughman, B., Lima, L. M., Liu, H.-L., Medeiros, A., Pautet, P.-D., Riggin, D. M., Sabbas, F. S., Sobral, J. H. A., Stamus, P., Takahashi, H., Taylor, M. J., Vadas, S. L., and Wrasse, C. M. (2009). The Spread F Experiment (SpreadFEx): Program overview and first results. *Earth Planets Space*, 61:411–430.

Groves, G. V. (1960). Upper-atmosphere wind studies by skylark rocket sodium experiment. *Nature, Lond.*, 187:1001.

Haerendel, G. V., Eccles, J. V., and Cakir, S. (1992). Theory for modeling the equatorial evening ionosphere and the origin of shear in the horizontal plasma flow. *J. Geophys. Res.*, 97(A2):1209–1223.

Hedin, A. E., Biondi, M. A., Burnside, R. G., Hernandez, G., Johnson, R. M., Kileen, T. L., Mazaudier, C., Meriwether, J. W., Salah, J. E., Smith, R. W., Spencer, N. W., Wickwar, V. B., and Virdi, T. S. (1991). Revised global model of thermosphere winds using satellite and ground-based observations. *J. Geophys. Res.*, 96(A5):7657.

Heelis, R. A. (2004). Electrodynamics in the low and middle latitude ionosphere: a tutorial. *J. Atmos. Sol. Terr. Phys.*, 66:825–838.

Heelis, R. A., Kendall, P. C., Moffett, R. J., Windle, D. W., and Rishbeth, H. (1974). Electrical coupling of the E and F-regions and its effect on F-region drifts and winds. *Planet. Space Sci.*, 22:743–756.

Heinselman, C. J. and Nicolls, M. J. (2008). A Bayesian approach to electric field and E-region neutral wind estimation with the Poker Flat Advanced Modular Incoherent Scatter Radar. *Radio Sci.*, (5):RS5013.

Holmes, J. M., Dressler, R., Pedersen, T. R., Caton, R. G., and Miller, D. (2016). High-resolution visible spectra from ionospheric samarium releases. *Radio Science*.

Huang, C.-S., de la Beaujardiere, O., Roddy, P. A., Hunton, D. E., Ballenthin, J. O., and Hairston, M. R. (2013). Long-lasting daytime equatorial plasma bubbles observed by the C/NOFS satellite. *J. Geophys. Res.*, 118(5):2398–2408.

Huang, C.-S. and Kelley, M. C. (1996a). Nonlinear evolution of equatorial spread F 1. on the role of plasma instabilities and spatial resonance associated with gravity wave seeding. *J. Geophys. Res.*, 101(A1):283–292.

Huang, C.-S. and Kelley, M. C. (1996b). Nonlinear evolution of equatorial spread F 2. gravity wave seeding of Rayleigh-Taylor instability. *J. Geophys. Res.*, 101(A1):293–302.

Huba, J. D., Joyce, G., and Krall, J. (2008). Three-dimensional equatorial spread F modeling. *Geophys. Res. Lett.*, 35:L10102.

Huba, J. D., Joyce, G., Krall, J., and England, S. L. (2009). Three-dimensional equatorial spread F modeling: Zonal neutral wind effects. *Geophys. Res. Lett.*, 36(19):L19106.

Hysell, D. L. (2016). Private communication.

Hysell, D. L., Jafari, R., Milla, M. A., and Meriwether, J. W. (2014). Data-driven numerical simulations of equatorial spread F in the Preuvian sector. *J. Geophys. Res. Space Physics*, 119:3815–3827.

Hysell, D. L., Kelley, M. C., and Swartz, W. E. (1990). Seeding and layering of equatorial spread F by gravity waves. *J. Geophys. Res.*, 95(A10):17253–17260.

Hysell, D. L. and Kudeki, E. (2004). Collisional shear instability in the equatorial F region ionosphere. *J. Geophys Res.*, 109:A11301.

Hysell, D. L., Kudeki, E., and Chau, J. L. (2005). Possible ionospheric preconditioning by shear flow leading to equatorial spread F. *Ann. Geophys.*, 23(7):2647–2655.

Hysell, D. L., Larsen, M. F., Swenson, C. M., Barjatya, A., and Wheeler, T. F. (2006). Shear flow effects at the onset of equatorial spread F. *J. Geophys. Res.*, 111:A11317.

Hysell, D. L., Milla, M. A., Condori, L., and Vierinen, J. (2015). Data-driven numerical simulations of equatorial spread F in the Peruvian sector 3: Solstice. *J. Geophys. Res.*, 120:10809–10822.

Ingersoll, J. (2008). A regularization technique for the analysis of photographic data used in chemical release wind measurements. *All Theses*, (Paper 421).

Ingwersen, P. A. and Lemnios, W. Z. (2000). Radars for ballistic missile defense research. *Linc. Lab. Journal*, 12(2):245–266.

Jahn, J.-M., LaBelle, J., and Pfaff, R. F. (1997). DC electric field measurements with the Guara spread-F rocket. *Geophys. Res. Lett.*, 24(13):1695–1698.

Kelley, M. C. (2009). *The Earth's Ionosphere: Plasma Physics and Electrodynamics.* Elseiver.

Kelley, M. C. and Ilma, R. R. (2016). Generation of a severe convective ionospheric storm under stable Rayleigh–Taylor conditions triggering by meteors? *Ann. Geophys.*, 34:165–170.

Kelley, M. C., LaBelle, J., Kudeki, E., Fejer, B. G., Basu, S., Basu, S., Baker, K. D., Hanuise, C., Argo, P., Woodman, R. F., Swartz, W. E., Farley, D. T., and J. W. Meriwether, J. (1986). The Condor equatorial spread F campaign: Overview and results of the large-scale measurements. *J. Geophys. Res.*, 91(A5):5487–5503.

Kelley, M. C., Larsen, M. F., LaHoz, C. A., and McClure, J. P. (1981). Gravity wave initiation of equatorial spread F: A case study. *J. Geophys. Res.*, 86:9087.

Kelley, M. C., Livingston, R. C., Rino, C. L., and Tsunoda, R. T. (1982). The vertical wave number spectrum of topside equatorial spread F: Estimates of backscatter levels and implications for a unified theory. *J. Geophys. Res.*, 87(A7):5217–5221.

Kelley, M. C., Makela, J. J., de La Beaujardiere, O., and Retterer, J. (2011). Convective ionospheric storms: A review. *Rev. Geophys.*, 49(2):RG2003.

Kelley, M. C., Makela, J. J., Ledvina, B. M., and Kintner, P. M. (2002). Observations of equatorial spread-F from Haleakala, Hawaii. *Geophys. Res. Lett.*, 30(4):2003.

Keskinen, M. J. (2010). Equatiroal ionospheric bubble precursor. *Geophys. Res. Lett.*, 37:L09106.

Keskinen, M. J., Mitchell, H. G., Fedder, J. A., Satyanarayana, P., Zalesak, S. T., and Huba, J. D. (1988). Nonlinear evolution of the Kelvin-Helmholtz instability in the high-latitude ionosphere. *J. Geophys. Res.*, 93:137.

Kiene, A., Larsen, M. F., and Kudeki, E. (2015). Equatorial F region neutral winds and shears near sunset measured with chemical release techniques. *J. Geophys. Res. Space Physics*, 120:9004–9013.

Kil, H., Paxton, L. J., and Oh, S.-J. (2009). Global bubble distribution seen from ROCSAT-1 and its association with the evening prereversal enhancement. *J. Geophys. Res.*, 114:A06307.

Killeen, T. L., Skinner, W. R., Johnson, R. M., Edmonson, C. J., Wu, Q., Niciejewski, R. J., Grassl, H. J., Gell, D. A., Hansen, P. E., Harvey, J. D., and Kafkalidis, J. F. (1999). TIMED Doppler interferometer (TIDI). *Proc. SPIE 3756, Optiucal Spectroscopic Techniques and Instrumentation for Atmospheric and Space Research III*, page 289.

Krall, J., Huba, J. D., and Martinis, C. R. (2009). Three-dimensional modeling of equatorial spread F airglow enhancements. *Geophys. Res. Lett.*, 36:L10103.

Krall, J., Huba, J. D., Ossakow, S. L., Joyce, G., Makela, J. J., Miller, E. S., and Kelley, M. C. (2011). Modeling of equatorial plasma bubbles triggered by non-equatorial traveling ionospheric disturbances. *Geophys. Res. Lett.*, 38(8):L08103.

Kudeki, E., Akgiray, A., Milla, M., Chau, J. L., and Hysell, D. L. (2007). Equatorial spread-F initiation: Post-sunset vortex, thermospheric winds, gravity waves. *J. Atmos. Sol-Terr. Phys.*, 69:2416–2427.

Kudeki, E. and Bhattacharyya, S. (1999). Postsunset vortex in equatorial F-region plasma drifts and implications for bottomside spread-F. *J. Geophys. Res.*, 104:28163–28170.

Kudeki, E., Fejer, B. G., Farley, D. T., and Ierkic, H. M. (1981). Interferometer studies of equatorial F-region irregularities and drifts. *Geophys. Res. Lett.*, 8:377.

LaBelle, J., Kelley, M. C., and Seyler, C. E. (1986). An analysis of the role of drift waves in equatorial spread F. *J. Geophys. Res.*, 91:5513.

Larsen, M. F. (2002). Winds and shears in the mesosphere and lower thermosphere: Results from four decades of chemical release wind measurements. *J. Geophys. Res.*, 107(A8):1215–1228.

Larsen, M. F., Meriwether, J. W., Niciejewski, R., and Vickery, K. (1989). Simultaneous observations of neutral winds and electric fields at spaced locations in the dawn auroral oval. *J. Geophys. Res.*, 94(A12):17235–17243.

Larsen, M. F. and Odom, C. D. (1997). Observations of altitudinal and latitudinal E-region neutral wind gradients near sunset at the magnetic equator. *Geophys. Res. Lett.*, 24(13):1711–1714.

Liu, H., Watanabe, S., and Kondo, T. (2009). Fast thermospheric wind jet at the Earth's dip equator. *Geophys. Res. Lett.*, 36:L08103.

Manju, G., Sridharan, R., Ravindran, S., Haridas, M. K. M., Pant, T. K., Sreelatha, P., and Kumar, S. V. M. (2012). Rocket borne in-situ Electron density and Neutral Wind measurements in the equatorial ionosphere–Results from the January 2010 annular solar eclipse campaign from India. *J. Atmos. Sol. Terr. Phys.*, 86:56–64.

Mendillo, M., Baumgardner, J., and Sultan, P. J. (1989). Optical and radar techniques applied to chemical release in active experiments in the ionosphere/thermosphere system. *Adv. Space Res.*, 10:8–15.

Meriwether, J. W., Moody, J. W., Biondi, M. A., and Roble, R. G. (1986). Optical interferometric measurements of nighttime equatorial thermospheric winds at Arequipa, Peru. *J. Geophys. Res.*, 91(A5):5557–5566.

Miller, E. S., Makela, J. J., and Kelley, M. C. (2009). Seeding of equatorial plasma depletions by polarization electric fields from middle latitudes: Experimental evidence. *Geophys. Res. Lett.*, 36:L18105.

Ossakow, S. L. and Chaturvedi, P. K. (1978). Morphological studies of rising equatorial spread F bubbles. *J. Geophys. Res.*, 83:2085.

Ossakow, S. L., Zalesak, S. T., McDonald, B. E., and Chaturvedi, P. K. (1979). Nonlinear equatorial spread F: Dependence on altitude of the F peak and bottomside background electron density gradient scale length. *J. Geophys. Res.*, 84:17.

Ossakow, S. L., Zalesak, S. T., and Zabusky, N. J. (August 1977). Recent results on cleavage, bifurcation, and cascade mechanisms in ionospheric plasma clouds. *Memo. Rep. 3579*, (Nav. Res. Lab., Washington, D. C.).

Pedersen, T. R., Miller, D., Holmes, J. M., and Groves, K. M. (2016). Empirical modeling of plasma clouds produced by the Metal Oxide Space Clouds (MOSC) experiment. *Radio Science*.

Pfaff, R., Yamamoto, M., Marionni, P., Mori, H., and Fukao, S. (1998). Electric field measurements above and within a sporadic-E layer. *Geophys. Res. Lett.*, 25(11):1769–1772.

Pfaff, R. F., Sobral, J. H. A., Abdu, M. A., Swartz, W. E., LaBelle, J. W., Larsen, M. F., Goldberg, R. A., and Schmidlin, F. J. (1997). The Guara campaign: A series of rocket-radar investigations of the Earth's upper atmosphere at the magnetic equator. *Geophys. Res. Lett.*, 24(13):1663–1666.

Picone, J. M., Hedin, A. E., Drob, D. P., and Aikin, A. C. (2002). NRLMSISE-00 empirical model of the atmosphere: Statistical comparisons and scientific issues. *J. Geophys. Res.*, 107(A12):2416–2427.

Raghavarao, R., Gupta, S. P., Sekar, R., Narayanan, R., Desai, J. N., Sridharan, R., Babu, V. V., and Sudhakar, V. (1987). In situ measurements of winds electric fields and electron densities at the onset of equatorial spread F. *J. Atmos. Terr. Phys.*, 49(5):485–492.

Rayleigh, J. W. S. (1883). Investigation of the character of the equilibrium of an incompressible heavy fluid of variable density. *Proc. London Math. Soc.*, 14:170–177.

Reigber, C., Luhr, H., and Schwintzer, P. (2002). CHAMP mission status. *Adv. SPace Res.*, 30(2):129–134.

Retterer, J. M. (2010a). Forecasting low-latitude radio scintillation with 3-D ionospheric plume models: 1. Plume model. *J. Geophys. Res.*, 115:A03306.

Retterer, J. M. (2010b). Forecasting low-latitude radio scintillation with 3-D ionospheric plume models: 2. Scintillation calculation. *J. Geophys. Res.*, 115:A03307.

Richmond, A. D. (1972). Numerical model of the equatorial electrojet. *Tech. Rep. AFCRL-72-0668, ERP 421*, (Air Force Cambridge Res. Lab., Bedford, Mass).

Rider, K., Immel, T., Taylor, E., and Craig, W. (2015). ICON: Where Earth's weather meets space weather. *2015 IEEE Aerospace Conference*, pages 1–10.

Rishbeth, H. (1971). Polarization fields produced by winds in the equatorial F region. *Planet. Space Sci.*, 19:357–369.

Rosenberg, N. W., Golumb, D., and Jr., E. F. A. (1963). Chemiluminescence of trimethyl aluminum released into the upper atmosphere. *J. Geophys. Res.*, 68:5895–5898.

Saad, Y. (1990). SPARSKIT: A basic tool kit for sparse matrix computations. *Tech. Rep. RIACS-90-20.*

Sastri, J. H. (1996). Longitudinal dependence of equatorial F region vertical plasma drifts in the dusk sector. *J. Geophys. Res.*, 101(A2):2445–2452.

Satyanarayana, P., Guzdar, P. N., Huba, J. D., and Ossakow, S. L. (1984). Rayleigh-Taylor instability in the presence of a stratified shear layer. *J. Geophys. Res.*, 92:8813.

Scannepieco, A. J. and Ossakow, S. L. (1976). Nonlinear equatorial spread F. *Geophys. Res. Lett.*, 3:451.

Scherliess, L. and Fejer, B. G. (1999). Radar and satellite global equatorial F region vertical drift model. *J. Geophys. Res.*, 104:6829–6842.

Schunk, R. W. and Nagy, A. F. (2004). *Ionospheres: Physics, Plasma Physics, and Chemistry.* Cambridge Univ. Press, Cambridge.

Sekar, R., Suhasini, R., and Raghavarao, R. (1994). Effects of vertical winds and electric fields in the nonlinear evolution of equatorial spread F. *J. Geophys. Res.*, 99(A2):2205–2213.

Shah, G. M. (1970). Study of aerosols in the atmosphere by twilight scattering. *Tellus*, 22(1):82–93.

Shepherd, G. G., Thuillier, G., Gault, W. A., Solheim, B. H., Hersom, C., Alunni, J. M., Brun, J.-F., Brune, S., Charlot, P., Cogger, L. L., Desaulniers, D.-L., Evans, W. F. J., Gattinger, R. L., Girod, F., Harvie, D., Hum, R. H., Kendall, D. J. W., Llewellyn, E. J., Lowe, R. P., Ohrt, J., Pasternak, F., Peillet, O., Powell, I., Rochon, Y., Ward, W. E., Wiens, R. H., and Wimperis, J. (1993). WINDII, the wind imaging interferometer on the Upper Atmosphere Research Satellite. *J. Geophys. Res.*, 98(D6):10725–10750.

Shume, E. B., Hysell, D. L., and Chau, J. L. (2005). Zonal wind velocity profiles in the equatorial electrojet derived from phase velocities of type II radar echoes. *J. Geophys. Res.*, 110:A12308.

Spencer, N. W., Wharton, L. E., Carignan, G. R., and Maurer, J. C. (1982). Thermosphere zonal winds, vertical motions and temperature as measured from Dynamics Explorer. *Geophys. Res. Lett.*, 9(9):953–956.

Sultan, P. J. (1996). Linear theory and modeling of the Rayleigh-Taylor instability leading to the occurrence of equatorial spread F. *J. Geophys. Res.*, 101(A12):26875–26891.

Swisdak, M. (2006). Notes on the dipole coordinate system. *Plasma Physics Division, Naval Research Laboratory, Washington, D. C.*, page arXiv:physics/0606044.

Szuszczewicz, E. P., Tsunoda, R. T., Narcisi, R., and Holmes, J. C. (1980). Coincident radar and rocket observations of equatorial spread F. *Geophys. Res. Lett.*, 7:537.

Tapley, B. D., Bettadpur, S., Watkins, M., and Reigber, C. (2004). The gravity recovery and climate experiment: Mission overview and early results. *Geophys. Res. Lett.*, 31(9):L09607.

Taylor, G. L. (1950). The instability of liquid surfaces when accelerated in a direction perpendicular to their planes. *Proc. R. Soc. London*, 201:192–196.

Tsunoda, R. T. (2005). On the enigma of day-to-day variability in equatorial spread F. *Geophys. Res. Lett.*, 32:L08103.

Tsunoda, R. T. (2006). Day-to-day variability in equatorial spread F: Is there some physics missing? *Geophys. Res. Lett.*, 33:L16106.

Valenzuela, A. G., Haerendel, G., Foppl, A., Kappler, H., Woodman, R. F., Fejer, B. G., and Kelley, M. C. (1980). Barium cloud observations of shear flow in the post sunset equatorial F layer. *Amer. Geophys. Union, Spring Meeting.*

van der Vorst, H. (1992). Bi-CGSTAB: A fast and smoothly converging variant of Bi-CG for the solution of nonsymmetric linear systems. *SIAM J. Sci. Stat. Comput.*, 13:631–644.

van Helleputte, T., Doornbos, E., and Visser, P. (2009). CHAMP and GRACE accelerometer calibration by GPS-based orbit determination. *Adv. Space Res.*, 43(12):1890–1896.

Watanabe, S., Abe, T., Habu, H., Kakinami, Y., Yamamoto, M.-Y., and Yamamoto, M. (2013). WINDs Campaign – Ion-neutral coupling in the thermosphere. *International Symposium on Space Technology and Science, 2013*, page Accessed from archive.ists.or.jp.

Woodman, R. F. (2009). Spread F–An old equatorial aeronomy problem finally resolved? *Ann. Geophys.*, 27:1915–1934.

Woodman, R. F. and LaHoz, C. (1976). Radar observations of F region equatorial irregularities. *J. Geophys. Res.*, 81:5447–5466.

Zalesak, S. T. and Ossakow, S. L. (1980). Nonlinear equatorial spread F: Spatially large bubbles resulting from large horizontal scale initial perturbations. *J. Geophys. Res.*, 85(A5):2131–2142.

Zalesak, S. T., Ossakow, S. L., and Chaturvedi, P. K. (1982). Nonlinear equatorial spread F: The effect of neutral winds and background Pedersen conductivity. *J. Geophys. Res.*, 87(A1):151–166.